



GEORG-AUGUST-UNIVERSITÄT  
GÖTTINGEN

Fakultät für  
Physik  $\Phi^{[q,p]=i\hbar}$

### Master's Thesis

## Lagrangian Properties of Particle Transport in Weakly Turbulent Rayleigh-Bénard Convection

prepared by

**Simon Schütz**

from Göttingen

at the Max Planck Institute for Dynamics and Self-Organization

**Thesis period:** 11th March 2013 until 30th August 2013

**First referee:** Prof. Dr. Eberhard Bodenschatz

**Second referee:** Prof. Dr. Gert Lube



# Contents

<b>1. Introduction</b>	<b>1</b>
<b>2. Fluid and Particle Motion in Rayleigh-Bénard Convection</b>	<b>3</b>
2.1. Geometry of the Bénard System . . . . .	3
2.2. Fluid Motion in Rayleigh-Bénard Convection . . . . .	5
2.3. Dynamics of Rayleigh-Bénard Convection . . . . .	6
2.4. Boussinesq Approximation . . . . .	10
2.5. Lagrangian Particle Trajectories . . . . .	12
2.6. Diffusion by Brownian Motion . . . . .	13
2.7. Diffusion Under Advection . . . . .	14
<b>3. Numerical Scheme for Flow and Particles</b>	<b>17</b>
3.1. Numerical Solution of the Boussinesq Equations . . . . .	17
3.1.1. Toroidal-Poloidal Decomposition of the Velocity Field . . . . .	17
3.1.2. Galerkin Method . . . . .	19
3.1.3. Pseudo-Spectral Discretization . . . . .	22
3.1.4. Penalization . . . . .	23
3.1.5. Dealiasing . . . . .	24
3.1.6. Time Stepping Scheme . . . . .	25
3.2. Particle Tracing . . . . .	26
3.2.1. Implementation of Particle Advection . . . . .	26
3.2.2. Implementation of Brownian Diffusion . . . . .	27
3.3. Parallelized Implementation of the Simulation Scheme . . . . .	27
3.3.1. GPU Architecture and Computing Model . . . . .	27
3.3.2. Initialization and Simulation Loop . . . . .	30
3.3.3. Data Containers . . . . .	30
3.3.4. Time Stepping Operators . . . . .	31
3.3.5. Particle Tracer . . . . .	32
3.3.6. Output Methods . . . . .	33
3.3.7. Performance Optimizations . . . . .	34
<b>4. Particle Transport in Spiral Defect Chaos</b>	<b>37</b>
4.1. Onset of SDC in Large Systems . . . . .	37
4.2. Particle Transport in Stationary Patterns . . . . .	42
4.2.1. Ideal Straight Rolls . . . . .	42
4.2.2. Straight Rolls with Imposed Mean Flow . . . . .	44

## Contents

4.2.3.	Giant Spiral . . . . .	46
4.2.4.	Dislocation . . . . .	48
4.2.5.	Dislocation Lines . . . . .	50
4.3.	Diffusive Transport of Passive Scalar . . . . .	52
4.3.1.	Mean Square Displacement . . . . .	52
4.3.2.	Effective Diffusivity . . . . .	54
4.3.3.	Diffusion Enhancement . . . . .	55
4.3.4.	Rayleigh Number Effects on Diffusion Enhancement . . . . .	58
4.4.	Two-Particle Dispersion in Spiral Defect Chaos . . . . .	60
4.4.1.	Radial Distribution . . . . .	64
4.4.2.	Horizontal and Vertical Dispersion . . . . .	65
4.4.3.	Influence of Diffusivity on Effective Dispersion . . . . .	67
4.4.4.	Influence of Rayleigh Number on Effective Dispersion . . . . .	68
4.4.5.	Dislocation Effects on Dispersion Enhancement . . . . .	70
4.5.	Irreversibility of Convective Flow . . . . .	72
<b>5.</b>	<b>Conclusions and Outlook</b>	<b>75</b>
5.1.	Parallelized Galerkin Solver and Particle Tracer . . . . .	75
5.2.	Transport Properties of Spiral Defect Chaos . . . . .	77
<b>A.</b>	<b>Appendix</b>	<b>81</b>
A.1.	Discrete Equations for the Boussinesq Problem . . . . .	81
A.2.	Table of Simulation Parameters . . . . .	88
A.3.	Error in the Simulation Code . . . . .	89

# List of Figures

2.1. Geometries of the Periodic and Cylindrical Fluid Cell . . . . .	3
2.2. Busse Balloon . . . . .	7
2.3. Skewed Varicose Instability . . . . .	8
2.4. Cross Roll Instability . . . . .	8
2.5. Bistability of Ideal Straight Rolls and Spiral Defect Chaos . . . . .	9
2.6. Aspect Ratio Dependence of Spiral Defect Chaos Onset . . . . .	9
3.1. Sine and Chandrasekhar Functions . . . . .	21
3.2. GPU Multiprocessor Layout . . . . .	28
3.3. Control Flow between CPU and GPU . . . . .	29
3.4. Memory Access for Data Transfers between CPU and GPU . . . . .	29
3.5. Graphical Frontend for Real-Time Output . . . . .	34
4.1. Convection Pattern in a Large Aspect Ratio System at $\varepsilon = 0.2$ . . . . .	38
4.2. Convection Pattern in a Large Aspect Ratio System at $\varepsilon = 0.4$ . . . . .	39
4.3. Convection Pattern in a Large Aspect Ratio System at $\varepsilon = 0.5$ . . . . .	40
4.4. Convection Pattern in a Large Aspect Ratio System at $\varepsilon = 0.6$ . . . . .	41
4.5. Flow Field in Ideal Straight Rolls . . . . .	42
4.6. Particle Transport in Ideal Straight Rolls . . . . .	43
4.7. Vertical Velocity Profile of Imposed Mean Flow . . . . .	44
4.8. Particle Transport in Ideal Straight Rolls with Imposed Mean Flow . . . . .	45
4.9. Convection Pattern of a Giant Spiral . . . . .	46
4.10. Particle Transport in a Giant Spiral . . . . .	47
4.11. Mean Flow of Giant Spiral and Dislocation . . . . .	48
4.12. Particle Transport around a Dislocation . . . . .	49
4.13. Instability of Straight Roll Domain Boundary . . . . .	50
4.14. Particle Transport along Dislocation Line . . . . .	51
4.15. Convection Pattern and Particle Density in a Cylindrical System . . . . .	52
4.16. Development of the Mean-Square Displacement $M_2(t)$ . . . . .	53
4.17. Relation between Effective Diffusivity $\mathcal{L}^*$ and Particle Diffusivity $\mathcal{L}$ . . . . .	54
4.18. Diffusion Enhancement relative to the Péclet Number . . . . .	56
4.19. Characteristic Velocity $U$ relative to $\varepsilon$ . . . . .	57
4.20. Diffusion Enhancement $\mathcal{L}^* - \mathcal{L}$ relative to $\varepsilon$ at $\Gamma = 30$ . . . . .	58
4.21. Diffusion Enhancement $\mathcal{L}^* - \mathcal{L}$ relative to $\varepsilon$ at $\Gamma = 100$ . . . . .	59
4.22. Pair Dispersion $R^2(t)$ of Tracer Particles . . . . .	61

*List of Figures*

4.23. Lagrangian Diffusivity at $\varepsilon = 0.2$ . . . . .	62
4.24. Lagrangian Diffusivity at $\varepsilon = 0.4$ . . . . .	63
4.25. Lagrangian Diffusivity at $\varepsilon = 0.6$ . . . . .	63
4.26. Horizontal Radial Distribution Function of Particle Pairs . . . . .	65
4.27. Lagrangian Diffusivity for the Horizontal and Vertical Dispersion Components . . . . .	66
4.28. Lagrangian Diffusion Enhancement relative to the Péclet Number . . . . .	68
4.29. Lagrangian Diffusivity at Different Rayleigh Numbers . . . . .	69
4.30. Lagrangian Diffusion Enhancement $\mathcal{L}_L^* - \mathcal{L}$ relative to $\varepsilon$ . . . . .	69
4.31. Development of the Two-Particle Dispersion $R^2(t)$ for ISR and SDC . . . . .	70
4.32. Lagrangian Diffusion Enhancement Relative to the Péclet Number, for ISR and SDC	71
4.33. Convection Pattern at $\Gamma = 50$ and $\varepsilon = 0.8$ . . . . .	71
4.34. Third Moment of the Work $W(\tau)$ on a Particle . . . . .	72
4.35. Variance and Skewness of the Work $W(\tau)$ on a Particle . . . . .	73

# 1. Introduction

Of the many goals in studying large-scale fluid motion, one lies in understanding its transport of mass. This transport is a vital process in nature on many scales, and also highly relevant for industrial applications. From the distribution of chemical species on a reactive surface[29] to atmospheric dispersion of pollutants[9], a thorough understanding of the relevant processes is required to face existing challenges. In addition, understanding the transport properties of a flow is a key method to understand the flow itself[25].

One important large-scale flow is thermal convection, where collective fluid motion is driven by a temperature gradient within the fluid. Under gravitational acceleration, variations in density due to thermal expansion cause a buoyancy force, which drives a physical motion. The motion is suppressed for small temperature gradients due to the fluid's viscosity, but convection sets in above a system-dependent threshold. As a self-sustained means of fluid motion, driven by an external temperature gradient, convection transports heat and material through the system. Because this transport couples back to the driving mechanism in a nonlinear fashion, a vast abundance of complex and interesting patterns emerge.

The Bénard system, introduced in 1900 by H. Bénard[3], produces this kind of convection and has therefore been subject to much experimental and theoretical investigation[5, 15]. A fluid is contained between two parallel plates at constant, but different temperatures. The plates are perpendicular to the direction of gravity, the bottom plate being warmer than the top plate. At a sufficiently high temperature difference, convective fluid motion sets in. After a mathematical description of the instability by J. W. Rayleigh[23], convection in the Bénard system is called Rayleigh-Bénard Convection (RBC). It is an example for pattern formation in non-equilibrium systems.

A special state of Rayleigh-Bénard convection is the so-called Spiral Defect Chaos (SDC), in which the convection rolls form a spatiotemporally chaotic pattern of rotating spirals and other defects. This state, first described by Morris *et al.*[20], is common for systems where the thermal diffusivity and kinematic viscosity of the fluid have a similar order of magnitude. Transport behavior of a fluid in this state is the main point of investigation in this thesis.

We focus on the transport of point particles that get advected with the flow pattern, but additionally experience molecular diffusion. The interplay between the spatiotemporal chaos of large-scale advection and the local diffusion process opens up new perspectives on transport phenomena that are related to the spreading of gases in the earth's atmosphere or nutrients in ocean flows, but may also provide new insights into the emergence of Spiral Defect Chaos itself. While a first intuitive approach is to investigate the transport of a particle away from its initial position in a fixed coordinate system, we assume the Lagrangian perspective and consider the relative distance between pairs of particles in the flow field.

## *1. Introduction*

The numerical method that we use in our investigation is based on earlier work by Jens Zudrop, who in his Master's thesis[32] describes a GPU-parallelized pseudo-spectral Galerkin scheme to simulate Rayleigh-Bénard convection in high aspect ratio systems at low Rayleigh numbers. We extend this simulation code to a higher vertical resolution, optimize it for speed, and include an advection-diffusion mechanism for point particles.

This thesis is structured as follows: After the introductory Chapter 1, Chapter 2 provides an analytical description of the Bénard system and the governing equations of fluid motion. It discusses models of particle motion in this system, and gives an overview of the dynamics of Rayleigh-Bénard Convection. Chapter 3 derives the numerical model used for simulating the thermal convection according to the Boussinesq model, and the method to advance the diffusive tracer particles inside the fluid's velocity field. In Chapter 4, the results of the numerical simulations are stated, and briefly discussed in the context of the available literature. Finally, Chapter 5 summarizes this thesis. It discusses the results from Chapter 4 from a more general perspective, and relates them to results from other numerical and experimental studies.

## 2. Fluid and Particle Motion in Rayleigh-Bénard Convection

In this chapter, we discuss the dynamics of fluid motion in Rayleigh-Bénard convection and of passive diffusive particles in the flow field. For this, we first have to define the geometry of the system under consideration, for which we can then derive a dimensionless form of the equations of fluid motion and temperature evolution. We describe the Boussinesq approximation that eliminates the pressure field from the equations, and motivate the Rayleigh and Prandtl numbers. In the second part of this chapter, we introduce the Lagrangian view on a flow field and different types of tracer particles. We describe the mechanisms of diffusion and advection that affect the trajectories of tracer particles in the fluid.

### 2.1. Geometry of the Bénard System

The Bénard system consists of a fluid between two horizontal flat plates, of which the bottom one is held at constant temperature  $T_b$  while the top one is at temperature  $T_t$ . In a Cartesian coordinate system, where the  $x$ - and  $y$ -axes denote the horizontal directions while the  $z$ -axis points vertically upward, we consider a square cell with edge length  $L$  in the horizontal directions and cell height  $d$ . The domain of this cell is

$$\bar{\Omega} = [0; L] \times [0; L] \times [-\frac{d}{2}; \frac{d}{2}]. \quad (2.1)$$

We consider two geometries of fluid volume in the domain: A cylinder with no-slip side walls and a square system with periodic boundaries (Fig. 2.1). The cylindrical system provides a basis for comparison to experiments[21] and other simulations[11], whereas the periodic system is the

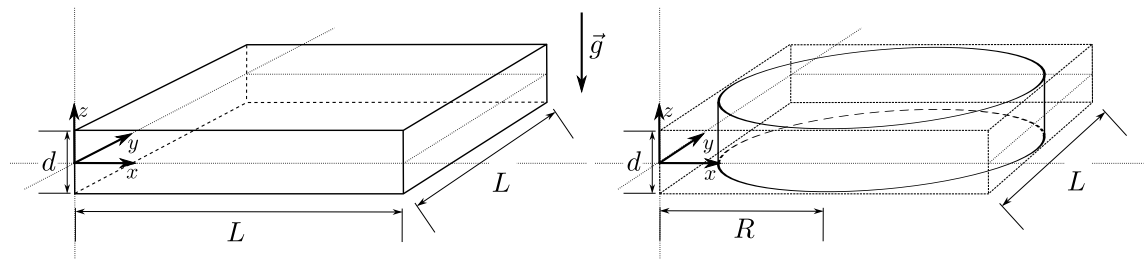


Figure 2.1.: Geometries of the periodic and cylindrical fluid cell. Note that the origin lies in the middle between the top and bottom plates. Solid lines mark the fluid volume  $\bar{\Omega}_f$ .

## 2. Fluid and Particle Motion in Rayleigh-Bénard Convection

most general type of Bénard system, which uses the full domain  $\bar{\Omega}$  and avoids any side boundary effects. For the cylindrical system of radius  $R$ , the fluid volume is

$$\bar{\Omega}_{f,\text{cyl}} := \left\{ \vec{x} \in \bar{\Omega} : (x - \frac{L}{2})^2 + (y - \frac{L}{2})^2 \leq R^2 \right\} \quad (2.2)$$

and we define the aspect ratio  $\Gamma$  as the quotient of radius  $R$  and height  $d$ ,

$$\Gamma_{\text{cyl}} := \frac{R}{d}. \quad (2.3)$$

The fluid volume  $\bar{\Omega}_{f,\text{periodic}}$  of the periodic system is the cell domain  $\bar{\Omega}$ , and we define the aspect ratio as the half width to depth ratio,

$$\Gamma_{\text{periodic}} := \frac{L}{2 \cdot d}. \quad (2.4)$$

Heating of the bottom plate creates a positive difference between bottom and top temperatures and causes an unstable layering in a fluid with positive heat expansion, which is the interesting case that leads to thermal convection. We call the temperature difference between the plates

$$\Delta T := T_b - T_t, \quad (2.5)$$

and the mean between top and bottom temperatures

$$T_0 := \frac{T_t + T_b}{2}. \quad (2.6)$$

We focus on the boundaries of the fluid volume that are not periodic and call them  $\partial\Omega_f$ . For the periodic system, they are the top plate  $\partial\Omega_t$  and bottom plate  $\partial\Omega_b$ :

$$\partial\Omega_{t,\text{periodic}} := \left\{ \vec{x} \in \bar{\Omega}_f : z = \frac{d}{2} \right\} \quad (2.7a)$$

$$\partial\Omega_{b,\text{periodic}} := \left\{ \vec{x} \in \bar{\Omega}_f : z = -\frac{d}{2} \right\} \quad (2.7b)$$

For the cylinder, the side wall  $\partial\Omega_{\text{cyl}}$  is also taken into account:

$$\partial\Omega_{t,\text{cyl}} := \left\{ \vec{x} \in \bar{\Omega}_f : z = \frac{d}{2} \wedge (x - \frac{L}{2})^2 + (y - \frac{L}{2})^2 \leq R^2 \right\} \quad (2.8a)$$

$$\partial\Omega_{b,\text{cyl}} := \left\{ \vec{x} \in \bar{\Omega}_f : z = -\frac{d}{2} \wedge (x - \frac{L}{2})^2 + (y - \frac{L}{2})^2 \leq R^2 \right\} \quad (2.8b)$$

$$\partial\Omega_{\text{cyl}} := \left\{ \vec{x} \in \bar{\Omega}_f : (x - \frac{L}{2})^2 + (y - \frac{L}{2})^2 = R^2 \right\} \quad (2.8c)$$

For the velocity field  $\vec{u}$ , we impose no-slip boundary conditions that require the velocity to vanish at all boundaries  $\partial\Omega_f$  of the fluid volume. This affects the top and bottom plates and side walls for the cylindrical system, but only the top and bottom plates for the periodic system. With  $\partial\Omega_f$  chosen appropriately, we get

$$\vec{u}(\vec{x}) = 0 \quad \forall \vec{x} \in \partial\Omega_f. \quad (2.9)$$

The temperature field  $T$  is fixed at the top and bottom plates. In the cylindrical geometry,

the side walls have a linear gradient between the top and bottom temperature, such that the temperature boundary conditions read

$$T(\vec{x}) = T_t \quad \forall \vec{x} \in \partial\Omega_t, \quad (2.10a)$$

$$T(\vec{x}) = T_b \quad \forall \vec{x} \in \partial\Omega_b, \quad (2.10b)$$

$$T(\vec{x}) = T_0 - \frac{z}{d} \cdot \Delta T \quad \forall \vec{x} \in \partial\Omega_{cyl}. \quad (2.10c)$$

## 2.2. Fluid Motion in Rayleigh-Bénard Convection

Fluid motion in the Bénard experiment is governed by the Navier-Stokes equation, which is the most general description for the movement of a viscous fluid. This description follows from Reynold's transport theorem[24] and the conservation of mass, energy and momentum, for details see [10, 32]. Conservation of momentum can be written for the velocity field  $\vec{u}$  of the fluid as

$$\partial_t(\rho\vec{u}) + \vec{u} \cdot \nabla(\rho\vec{u}) = -\nabla p + \nabla \cdot \mathbb{T} + \vec{f}_{\text{ext}}, \quad (2.11)$$

where  $\rho$  is the fluid mass density,  $p$  the pressure,  $\mathbb{T}$  the deviatoric stress tensor[10] and  $\vec{f}_{\text{ext}}$  an external force density. Entering the mass density  $\rho$  into the transport theorem, we get the continuity equation

$$\partial_t\rho + \nabla \cdot (\rho\vec{u}) = 0. \quad (2.12)$$

The energy density  $e$  of the fluid is the sum of the kinetic energy density  $e_{kin} = \frac{1}{2}\rho\vec{u}^2$  and the thermal energy density  $e_{therm} = \rho c T$  with heat capacity  $c$  and temperature  $T$ . From the heat equation, we get

$$\partial_t(\rho c T) + \vec{u} \cdot \nabla(\rho c T) = k\nabla^2 T, \quad (2.13)$$

where  $k$  is the thermal conductivity of the fluid. Together with a local relation  $p(\rho, e)$  and expressions for the stress tensor  $\mathbb{T}$  and the force  $\vec{f}$ , the three equations (2.11), (2.12) and (2.13) are sufficient to describe the temporal evolution of the convective flow in the Bénard system.

We consider a Newtonian fluid with  $\nabla \cdot \mathbb{T} = \mu \nabla^2 \vec{u}$ , where  $\mu$  is the dynamic viscosity of the fluid. From the dynamic viscosity, the local density and thermal properties of the fluid, we can define the kinematic viscosity  $\nu$  and thermal diffusivity  $\kappa$  by the relations[10]

$$\nu := \frac{\mu}{\rho} \quad \text{and} \quad \kappa := \frac{k}{\rho c}. \quad (2.14)$$

Convection is driven by buoyancy, which in our system is caused by the accelerative effect of gravity upon density variations of the fluid. We therefore assume a gravitational external force with acceleration  $g$  in the negative  $z$ -direction,

$$\vec{f}_{\text{ext}} = -\rho g \vec{e}_z. \quad (2.15)$$

### 2.3. Dynamics of Rayleigh-Bénard Convection

Describing the rich dynamics of Rayleigh-Bénard Convection is beyond the scope of this thesis, for an overview see [4, 5, 15]. We shall here limit ourselves to a description of the behavior close to the onset of thermal convection, as this regime is the focus of our investigations.

The two most fundamental control parameters for the system dynamics are the *Rayleigh number*  $Ra$ , and the *Prandtl number*  $Pr$ <sup>1</sup>, which have the form:

$$Ra := \frac{\alpha g \Delta T d^3}{\nu \kappa} \quad (2.16)$$

$$Pr := \frac{\nu}{\kappa} \quad (2.17)$$

While the Rayleigh number describes the relative strength of thermal forcing of the system, the Prandtl number, which “can be viewed as the ratio of the thermal diffusion time  $t_\nu = d^2/\nu$  to the vertical viscous relaxation time  $t_\eta = d^2/\nu$ ” ([5], p. 710), describes the importance of thermal transport by convection relative to thermal diffusion. Our focus in the convective dynamics is on systems at Prandtl numbers  $Pr = 1$ .

For small (and negative)  $Ra$ , there exists a stable, stationary state in which the velocity of the fluid vanishes and the temperature assumes a linear,  $z$ -dependent profile of the form  $T(z) = T_0 - \frac{z}{d} \Delta T$ . At a critical Rayleigh number of

$$Ra_c \approx 1708, \quad (2.18)$$

convection sets in[26]. Fluctuations in the velocity and temperature fields become unstable for certain wave numbers and grow in time, starting at the critical wave number of

$$q_c \approx \frac{3.117}{d}, \quad (2.19)$$

as predicted by analysis of the Boussinesq equations (see Section 2.4) for a Bénard system of infinite extent[26]. The growing modes form counter-rotating convection rolls, which near onset have a tendency to assume a parallel configuration with low curvature. In a pattern of wave number  $q$  (where the periodicity is  $\lambda = 2\pi/q$ ), each of the alternating convection rolls has a width of

$$\frac{\lambda}{2} = \frac{\pi}{q}. \quad (2.20)$$

Hence, at onset ( $q = q_c$ ), the width-to-height ratio of a roll is

$$\Gamma_{\text{roll}} = \frac{\pi}{q_c d} \approx 1.008 : \quad (2.21)$$

The convection rolls are slightly wider than they are high. With increasing Rayleigh number the aspect ratio increases even further. The reduced Rayleigh number  $\varepsilon$  denotes the distance of a

---

<sup>1</sup> Often called  $\sigma$  in the literature, we here denote the Prandtl number by  $Pr$  in order not to confuse it with the standard deviation  $\sigma$  of a Gaussian distribution, which appears later in the context of diffusion.

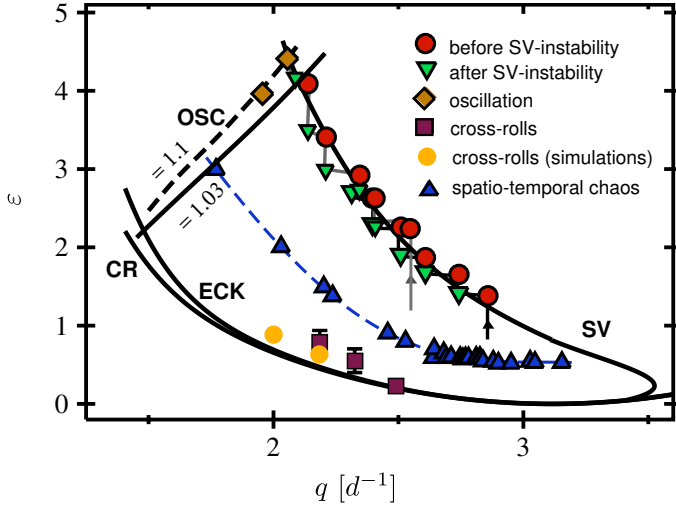


Figure 2.2.: Stability region of straight convection rolls for wave number  $q$  and Rayleigh parameter  $\varepsilon$ , at  $Pr \approx 1$ . Spatio-temporal chaos and straight rolls can exist for the same set of parameters. From Plapp [21].

system's  $Ra$  from the onset, and is defined as

$$\varepsilon := \frac{Ra - Ra_c}{Ra_c}. \quad (2.22)$$

The onset marks a second-order phase transition[4], with the maximum vertical velocity increasing with the square root of the reduced Rayleigh number.

In this thesis, we limit our investigations mostly to the range  $0 \leq \varepsilon \leq 1$ , with few exceptions of higher  $\varepsilon$  for small aspect ratio systems. For  $\varepsilon > 0$ , there exists a whole interval of stable wave numbers, limited at high and low wave numbers by secondary instabilities which decrease respectively increase the wave number. This stability region in the parameter space of  $q$ ,  $\varepsilon$  and  $Pr$  is called the Busse balloon[21], in Figure 2.2 we see its shape in the  $q$ - $\varepsilon$ -plane near  $Pr = 1$ .

Near onset, three secondary instabilities can occur, which are the Eckhaus instability, the Skewed Varicose instability, and the Cross Roll instability. The description of these instabilities will follow Plapp [21]. Assume a flow pattern of ideal straight rolls<sup>2</sup> with some wave number  $q_0$  in direction  $\vec{e}_x$ . The vertical midplane fluid motion will then have a profile of

$$u_z(x, y) \propto \exp(iq_0x). \quad (2.23)$$

Depending on  $q_0$ , modulations of this roll pattern will be unstable and grow from small perturbations. The slowly growing *Eckhaus instability* is a long wave length modulation of the wave vector in direction  $\vec{e}_x$ , with a modulation wave number  $s_x \ll q_0$ ,

$$u_z(x, y) \propto \exp(iq_0x) \cdot \exp(is_x x). \quad (2.24)$$

---

<sup>2</sup>We assume the system to be of infinite extent, so that the choice of direction  $\vec{e}_x$  is arbitrary. We neglect the  $z$ -dependent, three-dimensional structure of the flow field and higher-order deviations from the sine/cosine profile.

## 2. Fluid and Particle Motion in Rayleigh-Bénard Convection

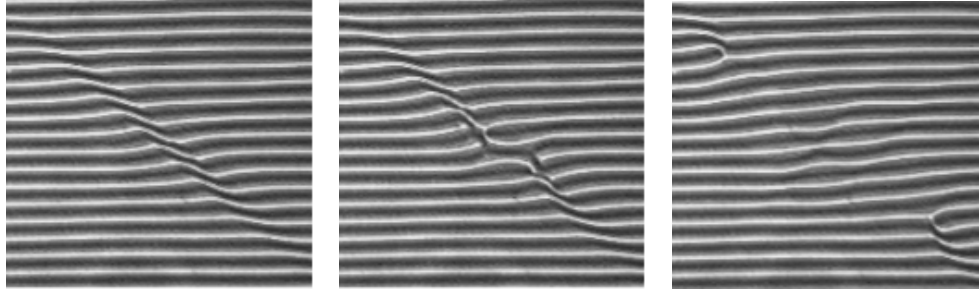


Figure 2.3.: Skewed Varicose instability at  $\varepsilon = 2.26$ ,  $Pr = 1.07$ , time increases from left to right. A pair of defects is generated, and the wave number decreases. Shadowgraph images, from Plapp[21].

It will modulate the spacing of rolls. The Eckhaus instability can both decrease and increase the wave number of the pattern, since for  $q_0 > q_c$ , closely spaced adjacent rolls will merge into one roll, while at  $q_0 < q_c$  new rolls will emerge from the gap between widely spaced convection rolls. In practice, we usually only observe the instability to increase the wave number, as the Skewed Varicose instability sets in for lower  $q_0 > q_c$ .

The *Skewed Varicose* instability is a long wave length modulation with a wave vector  $(s_x, s_y)^T$  (with  $s_x, s_y \ll q_0$ ) that is tilted against  $\vec{e}_x$ , usually by an angle close to  $\frac{\pi}{2}$ . The modulation then has the general form

$$u_z(x, y) \propto \exp(iq_0x) \cdot \exp[i(s_x x + s_y y)]. \quad (2.25)$$

The pattern is sheared, and reconnections form dislocation pairs that migrate away from each other to reduce the wave number of the pattern.

The *Cross roll instability* is a short wave length instability perpendicular to the original stripe pattern, with a wave number  $s_y \approx q_0$  and a modulation of the form

$$u_z(x, y) \propto \exp(iq_0x) \cdot \exp(is_y y). \quad (2.26)$$

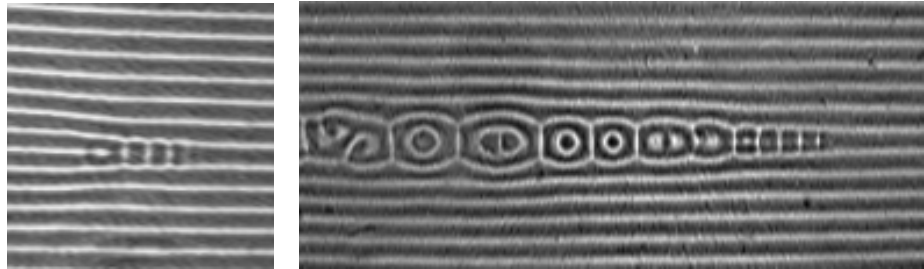


Figure 2.4.: Cross Roll instability at  $\varepsilon = 0.7$ ,  $Pr = 1.09$ , after rapidly decreasing  $\varepsilon$  from a higher value. Left: The Cross Roll instability migrates from left to right, increasing the wave number in the process. Right: *Totem Pole pattern*: The Cross Roll instability migrates from left to right, leaving behind a disordered region of targets and dislocations from which Spiral Defect Chaos can emerge. Shadowgraph images, from Plapp[21].

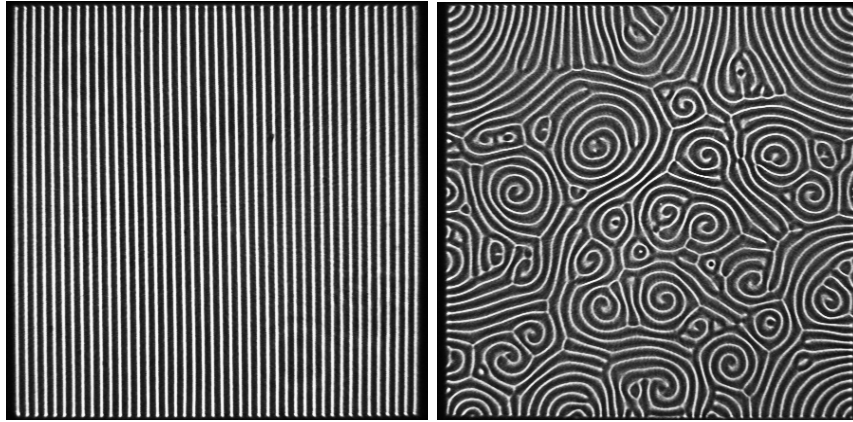


Figure 2.5.: Bistability of Ideal Straight Rolls and Spiral Defect Chaos, in a square cell at  $\varepsilon = 0.92$ . Depending on the initial conditions, the system assumes either the regular ISR state (left), or the dynamic SDC (right). Shadowgraph images, from Plapp[21].

For a given  $q_0$ , the instability occurs at lower  $\varepsilon$  than the Eckhaus instability, and would not be observed if  $\varepsilon$  was changed very slowly. However, it grows much faster, and is therefore common in systems with fast dynamics. Figures 2.3 and 2.4 show the Skewed Varicose and Cross Roll instabilities, as observed in the experiment by Plapp[21].

These instabilities characterize the reaction to infinitely small perturbations in infinitely large systems, but will be part of local processes in finite systems as well. However, finite-size perturbations and boundary effects can move the boundaries of the stability region, and allow more complex patterns to emerge[16]. One such pattern type is the *Spiral Defect Chaos* (SDC) state of Rayleigh-Bénard convection, which is known to be bistable with the *Ideal Straight Roll* (ISR) state at the same system parameters, both in bounded and periodic systems. SDC is characterized by convection rolls that form a spatiotemporally chaotic pattern rich of rotating spirals and other defects[20]. It is common for  $Pr \approx 1$ . Figure 2.5 shows ISR and SDC at identical experimental

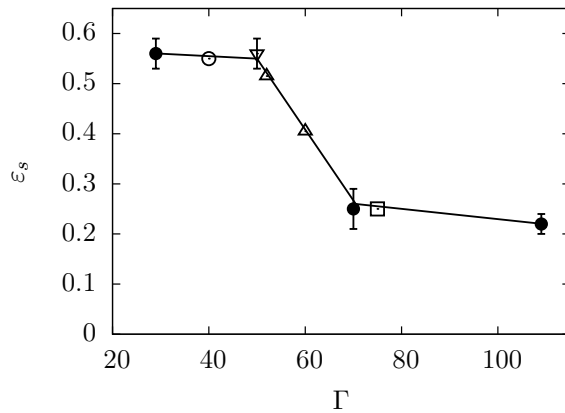


Figure 2.6.: Aspect ratio dependence of the onset of Spiral Defect Chaos for cylindrical cells at  $Pr \approx 1$ . Experimental data, assembled by Bodenschatz *et al.*[5].

## 2. Fluid and Particle Motion in Rayleigh-Bénard Convection

parameters. From random initial conditions, the SDC state will usually be assumed above the onset  $\varepsilon_s$  of SDC. ISR at unstable  $q_0$  can change to SDC via one of the above instabilities, whereas an SDC state can relax into ISR for small  $\varepsilon$ . SDC onset is higher for small systems[5], with a strong dependence of the onset  $\varepsilon_s$  on the aspect ratio  $\Gamma$  near  $\Gamma = 60$ , see Figure 2.6. The limit of SDC onset for infinite systems and precise data for the curve  $\varepsilon_s(\Gamma)$  are however still unknown, as large aspect ratio systems are hard to access experimentally, and equilibration into the dynamic equilibrium takes long for computer simulations.

### 2.4. Boussinesq Approximation

If the magnitude of fluid velocity  $V$  in this buoyancy-driven convection system is much smaller than the sound speed  $v_s$  in the fluid, such that fluctuations in the fluid density equilibrate fast, the Boussinesq approximation can be used to simplify the equations.

The Boussinesq approximation[7] assumes that the density  $\rho$  of the convecting fluid is constant, except in the term for  $\vec{f}_{\text{ext}}$  where a fluctuation in density leads to a strong buoyancy force. This approximation is justified if density fluctuations due to pressure differences equilibrate very fast ( $v_s \gg V$ ) and fluctuations due to temperature are much smaller than the mean density ( $\delta\rho \ll \rho_0$ ). For  $\vec{f}_{\text{ext}}$ , the density fluctuation due to temperature differences  $\delta T = T - T_0$  can be expanded in a Taylor series via the volume expansion coefficient of the fluid,

$$\alpha = \frac{1}{V} \left. \frac{\partial V}{\partial T} \right|_{T_0} : \quad (2.27)$$

$$\begin{aligned} \rho(T) &= \rho_0(1 - \alpha \delta T) + \mathcal{O}(\delta T^2) \\ \Rightarrow \vec{f}_{\text{ext}} &= \rho_0 (\alpha \delta T - 1) g \vec{e}_z + \mathcal{O}(\delta T^2). \end{aligned} \quad (2.28)$$

With the constant mean density  $\rho_0$ , the equations of fluid motion then read

$$\partial_t \vec{u} + \vec{u} \cdot \nabla \vec{u} - \frac{\mu}{\rho_0} \nabla^2 \vec{u} + \frac{1}{\rho_0} \nabla p = (\alpha \delta T - 1) g \vec{e}_z, \quad (2.29a)$$

$$\nabla \cdot \vec{u} = 0, \quad (2.29b)$$

$$\partial_t T + \vec{u} \cdot \nabla T = \frac{k}{\rho_0 c} \nabla^2 T. \quad (2.29c)$$

Above equations (2.29) have a stationary solution that fulfills the boundary conditions at the top and bottom plates, which are no-slip for the velocity and constant values for the temperature as discussed in Section 2.1. The stationary solution is

$$\tilde{u} = \vec{0}, \quad (2.30a)$$

$$\tilde{T} = T_0 - \frac{z \cdot \Delta T}{d}, \quad (2.30b)$$

$$\tilde{p} = \rho_0 g \left( z + \frac{\alpha \Delta T z^2}{2d} \right). \quad (2.30c)$$

We will generally choose our initial conditions close to this stationary solution, and observe how

small disturbances to the stationary solution grow into dynamic convection rolls. We will write these deviations from the stationary solution as

$$\vec{u}' := \vec{u} - \tilde{u}, \quad (2.31a)$$

$$T' := T - \tilde{T}, \quad (2.31b)$$

$$p' := p - \tilde{p}. \quad (2.31c)$$

We solve the evolution equations for these deviations only, and reconstruct the complete solution by adding it to the stationary fields. Note that the stationary fields still influence the deviations via the nonlinear terms. Given these stationary solutions, the equations for the fluid dynamics in the Bénard system for the deviations read

$$\partial_t \vec{u}' + \vec{u}' \cdot \nabla \vec{u}' - \nu \nabla^2 \vec{u}' + \frac{1}{\rho_0} \nabla p' = \alpha g T' \vec{e}_z, \quad (2.32a)$$

$$\nabla \cdot \vec{u}' = 0, \quad (2.32b)$$

$$\partial_t T' - \vec{u}' \cdot \frac{\Delta T}{d} \vec{e}_z + \vec{u}' \cdot \nabla T' = \kappa \nabla^2 T'. \quad (2.32c)$$

We identify the system height  $d$  as a characteristic length scale of the system, the total temperature difference  $\Delta T$  between the top and bottom plate as the characteristic temperature scale, and the vertical diffusion time

$$\tau_v := \frac{d^2}{\kappa} \quad (2.33)$$

as a characteristic time scale. We can then define dimensionless measures of the fluid velocity, temperature and pressure:

$$\hat{u} := \frac{d}{\kappa} \vec{u}' \quad (2.34a)$$

$$\hat{T} := \frac{T'}{\Delta T} \quad (2.34b)$$

$$\hat{p} := \frac{d^2}{\rho_0 \nu \kappa} p' \quad (2.34c)$$

With the derivative operators  $\partial_{\hat{t}} := \tau_v \partial_t$  and  $\hat{\nabla} := d \nabla$ , the incompressible Boussinesq equations then have the dimensionless form:

$$\partial_{\hat{t}} \hat{u} + \hat{u} \cdot \hat{\nabla} \hat{u} - \frac{\nu}{\kappa} \hat{\nabla}^2 \hat{u} + \frac{\nu}{\kappa} \hat{\nabla} \hat{p} = \frac{\nu}{\kappa} \frac{\alpha g \Delta T d^3}{\nu \kappa} \hat{T} \vec{e}_z \quad (2.35a)$$

$$\hat{\nabla} \cdot \hat{u} = 0 \quad (2.35b)$$

$$\partial_{\hat{t}} \hat{T} - \hat{u} \cdot \vec{e}_z + \hat{u} \cdot \hat{\nabla} \hat{T} = \hat{\nabla}^2 \hat{T} \quad (2.35c)$$

The dynamics is governed by two dimensionless numbers, which we identify as the Rayleigh number  $Ra = \frac{\alpha g \Delta T d^3}{\nu \kappa}$  and the Prandtl number  $Pr = \frac{\nu}{\kappa}$  (see Section 2.3). Expressed in terms of

## 2. Fluid and Particle Motion in Rayleigh-Bénard Convection

these quantities, the dimensionless incompressible Boussinesq equations read:

$$\frac{1}{Pr} \left( \partial_t \hat{u} + \hat{u} \cdot \hat{\nabla} \hat{u} \right) - \hat{\nabla}^2 \hat{u} + \hat{\nabla} \hat{p} = Ra \hat{T} \vec{e}_z \quad (2.36a)$$

$$\hat{\nabla} \cdot \hat{u} = 0 \quad (2.36b)$$

$$\partial_t \hat{T} - \hat{u} \cdot \vec{e}_z + \hat{u} \cdot \hat{\nabla} \hat{T} = \hat{\nabla}^2 \hat{T} \quad (2.36c)$$

The formulation in terms of dimensionless parameters makes it easy to find universal behavior and significant parameter values independent of the actual choice of system size or temperatures.

## 2.5. Lagrangian Particle Trajectories

To describe the behavior of a fluid, one can use the abstract concept of a fluid particle, an infinitesimally small quantity of the fluid for which the fluid velocity  $\vec{u}$  can be defined[10]. Many properties of a flow can be expressed by considering an observable and its behavior over time along a fluid particle's track rather than at a fixed location inside the flow field: A fixed position would have to be defined in some fixed, *Eulerian* coordinate system, but the advection velocity relative to an arbitrarily chosen fixed frame has no physical significance. In contrast, the local *Lagrangian* coordinate system of a fluid particle is specific to the local fluid flow, and by looking at many such fluid particles and how their position relative to each other changes with time, much can be learned about a flow field.

In numerics and experiments, the abstract concept of a fluid particle is replaced by the introduction of small tracer particles, whose physical properties and behavior in a flow field mostly depend on their size. Toschi *et al.*[30] discuss the equations of motion and observable quantities for Lagrangian particle trajectories in turbulence. The abstract fluid particle will always have the velocity of the fluid, such that the equation of motion for its position  $\vec{x}$  in the surrounding flow field  $\vec{u}$  is

$$\frac{d\vec{x}}{dt} = \vec{u}(\vec{x}(t), t). \quad (2.37)$$

Fluid particles must be neutrally buoyant and will for long times be distributed evenly throughout the fluid. Inertial particles may have a density  $\rho_p$  different from the fluid density  $\rho$  and are usually modelled as spheres of radius  $a$  whose velocity adjusts to the surrounding flow via Stokes drag. With the density mismatch being characterized by the factor  $\beta := \frac{3\rho}{2\rho_p + \rho}$  and the Stokes time  $\tau_S := \frac{a^2}{3\beta\nu}$ , where  $\nu$  is the fluid viscosity, position  $\vec{x}(t)$  and velocity  $\vec{v}(t)$  of inertial particles evolve as

$$\frac{d\vec{x}}{dt} = \vec{v}(t), \quad (2.38a)$$

$$\frac{d\vec{v}}{dt} = \beta \frac{D}{Dt} \vec{u}(\vec{x}(t), t) - \frac{\vec{v}(t) - \vec{u}(\vec{x}, t)}{\tau_S}. \quad (2.38b)$$

This formulation requires the flow field around the particles to be laminar and have small gradients, which in turbulence is valid if  $a$  is much smaller than the Kolmogorov length scale  $\eta$  that

depends on the fluid viscosity and energy-dissipation rate. On the other hand, both inertial particles and the abstract fluid particles need to have a radius  $a$  far above the mean-free-path level of the fluid molecules, at which thermal fluctuations make it impossible to even define a velocity of the flow. Luckily, in Rayleigh-Bénard convection close to onset, these scales are usually far apart and a wide range of tracer particle radii exists. Decreasing the radius towards the mean-free-path scale will cause fluctuations that will have a diffusive effect relative to the mean fluid motion. This effect will be discussed in Section 2.7.

Single particle trajectories, acceleration statistics and temporal correlations, like the structure function of velocity for a tracer's velocity component in some cartesian direction  $i$ ,

$$S_p(\tau) := \langle [v_i(t + \tau) - v_i(t)]^p \rangle, \quad (2.39)$$

can be used to gain insights into details of the flow both in turbulent and laminar flow fields[30]. One special approach in investigating the transport of fluid in a flow is to look at the relative motion of two particles, usually for tracks of particle pairs with a fixed initial separation. The *two-particle dispersion*[25],

$$R^2(t) := \langle [\vec{r}_{ij}(t) - \vec{r}_{ij}(t_0)]^2 \rangle, \quad (2.40)$$

is the average of the squared distance between two particles  $i$  and  $j$ , with their relative displacement vector being

$$\vec{r}_{ij} := \vec{x}_j - \vec{x}_i. \quad (2.41)$$

This relative dispersion has been used to investigate statistical properties of turbulence[6, 25], but is being used here to quantify effective fluid transport and mixing processes in laminar Rayleigh-Bénard convection for diffusing particles. With a high number of Lagrangian tracer particles, we can achieve a good spatial sampling of the system and arrive at a good statistics.

## 2.6. Diffusion by Brownian Motion

The motion of a particle inside a fluid at rest can be considered a random walk, where the steps are initiated by collisions with fluid particles that move by thermal fluctuations[18]. For a large number of noninteracting particles, one can define their density  $n$  and a flux  $\vec{j}$ , which according to Fick's law is proportional to the density gradient

$$\vec{j}_\phi = -\mathcal{D}\nabla\phi. \quad (2.42)$$

This relation defines the diffusion constant  $\mathcal{D}$ . Since the number of particles is conserved, gradients in the flux (like in Section 2.2) lead to a temporal change in density,

$$\partial_t n = \mathcal{D}\nabla^2 n. \quad (2.43)$$

For the initial condition  $n(\vec{x}, t=0) = N\delta(\vec{x})$  and boundary conditions  $n(\vec{x}, t) \rightarrow 0$  for  $|\vec{x}| \rightarrow \infty$ ,

## 2. Fluid and Particle Motion in Rayleigh-Bénard Convection

the diffusion Equation (2.43) is solved by a Gaussian distribution

$$n(\vec{x}, t) = \frac{N}{\sqrt{2\pi\sigma^2}} e^{-\frac{x^2}{2\sigma^2}} \quad (2.44)$$

with variance

$$\sigma^2 = 2n_d \mathcal{D}t, \quad (2.45)$$

where  $n_d$  is the number of dimensions and  $N$  the total number of particles.

The particle density  $n(\vec{x})$  for the noninteracting particles can be rewritten as the probability density  $\rho(\vec{x})$  of finding a single particle at location  $\vec{x}$ , by dividing by the total number of particles:

$$\rho(\vec{x}, t) = \frac{n(\vec{x}, t)}{N} = \frac{1}{\sqrt{2\pi\sigma^2}} e^{-\frac{x^2}{2\sigma^2}} \quad (2.46)$$

Applying the diffusion equation to the probability density for the location of one particle is a common technique. We use it in the discrete time-stepping of the simulation, where we assume that the mean free path of the particle motion is much smaller than the distance travelled in one time step.

## 2.7. Diffusion Under Advection

A particle that diffuses in a fluid that is not at rest, but moves with a constant velocity  $\vec{u}$ , experiences advection, such that the probability density for its location is

$$\rho(\vec{x}, t) = \rho_0(\vec{x} - \vec{u} \cdot t), \quad (2.47)$$

where  $\rho_0$  is the Gaussian probability density for a stationary fluid (Eq. (2.46)). While this relation does not hold in an inhomogeneous or non-stationary velocity field, it can be used as an approximation for time differences  $dt \ll 1$  if the field is sufficiently smooth around a particle's initial position  $\vec{x}_0$ . In this case, we write the particle's change in location  $d\vec{x}$  as the sum of the advective transport in the time  $dt$ , and a random noise  $\vec{\eta}$  drawn from the probability distribution (2.46):

$$d\vec{x} = \vec{u}(\vec{x}, t) \cdot dt + \vec{\eta}(t). \quad (2.48)$$

The Gaussian noise  $\vec{\eta}$  has zero mean and must be delta-correlated in time[2], i.e.

$$\langle \eta_i(t) \rangle = 0, \quad (2.49a)$$

$$\langle \eta_i(t) \eta_j(t') \rangle = 2\mathcal{D} dt \cdot \delta_{ij} \delta(t - t') \quad (2.49b)$$

for cartesian directions  $i, j$ . Note that this approximation is only possible if the time step  $dt$  is small compared to the temporal (and, via  $\vec{u}$ , the spatial) dynamics of the flow field, but large compared to the collision time of the Brownian motion. It yields a discrete equation of motion for

each diffusing particle:

$$\frac{d\vec{x}}{dt} = \vec{u}(\vec{x}, t) + \frac{\vec{\eta}(t)}{dt}. \quad (2.50)$$

In the three-dimensional flow field,  $\vec{\eta}$  is drawn from a Gaussian distribution around the origin with a standard deviation  $\sigma$  of

$$\sigma = \sqrt{6\mathcal{D} dt}. \quad (2.51)$$

In the unit systems adopted for the Bénard system, diffusivity is measured in units of  $\kappa$ . To simplify notation, particle diffusivity is therefore described by the dimensionless *Lewis number*<sup>3</sup>  $\mathcal{L}$ , which describes it in units of the thermal diffusivity  $\kappa$ :

$$\mathcal{L} := \frac{\mathcal{D}}{\kappa}. \quad (2.52)$$

---

<sup>3</sup>In many fields of science, the Lewis number is defined as  $\frac{\kappa}{\mathcal{D}}$ ; in RBC we take the inverse.



# 3. Numerical Scheme for Flow and Particles

While the formulation of the physical problem in terms of partial differential equations already makes simplifying assumptions regarding the phenomena involved, even those mathematical descriptions are still continuous in space and time, and can therefore not be solved with a computer. The challenge of numerics is to find an elegant method which, within the limits of memory and computation time, approximates the solution of the mathematical model as good as possible.

In this chapter, we describe the numerical methods for simulating the velocity and temperature fields of Rayleigh-Bénard convection in the incompressible Boussinesq model (Section 3.1), and for solving the advection-diffusion problem of point particles in the velocity field (Section 3.2). The method has been implemented using the programming language C++ and its extension CUDA, which allows for massive parallelization of the simulation algorithm on Graphics Processing Units (GPUs). Implementing the solver for the Boussinesq equations in CUDA has been the focus of the work of Zudrop[32], but we will briefly discuss this implementation and the additional details of the particle tracer in Section 3.3. For further detail, see [32].

## 3.1. Numerical Solution of the Boussinesq Equations

This section develops an efficient scheme to simulate the incompressible Boussinesq equations (2.36), which read

$$\frac{1}{Pr} \left( \partial_t \hat{u} + \hat{u} \cdot \hat{\nabla} \hat{u} \right) - \hat{\nabla}^2 \hat{u} + \hat{\nabla} \hat{p} = Ra \hat{T} \vec{e}_z, \quad (3.1a)$$

$$\hat{\nabla} \cdot \hat{u} = 0, \quad (3.1b)$$

$$\partial_t \hat{T} - \hat{u} \cdot \vec{e}_z + \hat{u} \cdot \hat{\nabla} \hat{T} = \hat{\nabla}^2 \hat{T}. \quad (3.1c)$$

The method makes use of a decomposition of the solenoidal (i.e. incompressible) velocity field into scalar potentials, and finds a spectral representation for the fields that solve the weak formulation for the equation system. The scheme and its derivation are mostly based on Zudrop[32].

### 3.1.1. Toroidal-Poloidal Decomposition of the Velocity Field

Hydrodynamic simulations can be performed both for compressible and incompressible flows. In compressible flows, the density is generally pressure dependent. Since pressure fluctuates on fast time scales and there is no simple equation for the time development of the pressure, standard methods for compressible flows have to include a Poisson solver for every time step, which is computationally expensive. We have therefore eliminated the pressure dependence from our equations and simulate an incompressible fluid. However, even then much effort is needed to explicitly in-

### 3. Numerical Scheme for Flow and Particles

clude the incompressibility condition  $\nabla \cdot \vec{u} = 0$  into the simulation with high accuracy. To avoid this effort, we decompose the velocity field in a way that fulfills the incompressibility condition implicitly, and simultaneously simplifies the scheme by removing a large number of degrees of freedom.

An incompressible (solenoidal) vector field  $\vec{u} : \mathbb{R}^3 \rightarrow \mathbb{R}^3$  can be generated by two scalar potential fields  $\phi, \psi$  via

$$\vec{u}(\vec{x}) = \underbrace{\nabla \times \nabla \times (\vec{e}\phi(\vec{x}))}_{\delta} + \underbrace{\nabla \times (\vec{e}\psi(\vec{x}))}_{\epsilon}, \quad (3.2)$$

where  $\vec{e}$  is a constant unit vector. This concept has been applied to the incompressible Boussinesq equations by Schmitt *et al.*[27].  $\phi$  is the poloidal component of the field,  $\psi$  is the toroidal component. Choosing  $\vec{e} = \vec{e}_z$  and defining  $\Delta_{xy} := \partial_x^2 + \partial_y^2$ , the curls (including the unit vector) reduce to the differential operators

$$\delta := \begin{pmatrix} \partial_x \partial_z \\ \partial_y \partial_z \\ -\Delta_{xy} \end{pmatrix} \quad \text{and} \quad \epsilon := \begin{pmatrix} \partial_y \\ -\partial_x \\ 0 \end{pmatrix}. \quad (3.3)$$

We consider the horizontally periodic domain of the Bénard system,  $\bar{\Omega} = \bar{\Omega}_{xy} \times \bar{\Omega}_z$ , with

$$\bar{\Omega}_{xy} := [0 : \frac{L}{d}] \times [0 : \frac{L}{d}], \quad (3.4a)$$

$$\bar{\Omega}_z := [-\frac{1}{2} : \frac{1}{2}]. \quad (3.4b)$$

In this domain, we define the horizontal mean  $\langle \dots \rangle_{xy}$  and the volume mean  $\langle \dots \rangle$  as

$$\langle \dots \rangle_{xy} := \frac{1}{\|\bar{\Omega}_{xy}\|} \int_{\bar{\Omega}_{xy}} \dots dx dy, \quad (3.5a)$$

$$\langle \dots \rangle := \frac{1}{\|\bar{\Omega}\|} \int_{\bar{\Omega}} \dots dx dy dz. \quad (3.5b)$$

Note that  $\langle \dots \rangle_{xy}$  is a quantity that still depends on  $z$ . Let  $f : \Omega \rightarrow \mathbb{R}$ ,  $g : \Omega \rightarrow \mathbb{R}$  be mean free ( $\langle f \rangle = \langle g \rangle = 0$ ), smooth, and periodic in  $x$  and  $y$ . Under the latter limitation, the horizontal mean of  $\delta f$  and  $\epsilon g$  vanishes ( $\langle \delta f \rangle_{xy} = \langle \epsilon g \rangle_{xy} = 0$ ). Any smooth solenoidal velocity field  $\vec{u}_0$  with vanishing horizontal mean ( $\langle \vec{u}_0 \rangle_{xy} = 0$ ) can be decomposed into  $\vec{u}_0 = \delta f + \epsilon g$ . For our periodic system, a horizontal mean flow  $\vec{H}(z) = (F(z), G(z), 0)^T$  needs to be added to avoid discontinuous conditions at the boundaries, such that we write the velocity field as

$$\vec{u} = \delta f + \epsilon g + \vec{H}. \quad (3.6)$$

The functions  $F : \Omega_z \rightarrow \mathbb{R}$  and  $G : \Omega_z \rightarrow \mathbb{R}$  are the  $x$ - and  $y$ -components of the mean flow of  $\vec{u}$  at a height  $z$  within the Bénard system. Note that to ensure  $\nabla \cdot \vec{H} = 0$  and respect the fixed boundaries at  $z = \pm \frac{1}{2}$ , the  $z$ -component of  $\vec{H}$  vanishes.

As shown in [27] and explained by [32], applying the operators  $\delta$  and  $\epsilon$  and the horizontal averaging  $\langle \dots \rangle_{xy}$  to (2.36a) and entering (3.6) into Equation (2.36c) gives a set of equations that

### 3.1. Numerical Solution of the Boussinesq Equations

is equivalent to the incompressible Boussinesq equations, but without an explicit incompressibility equation:

$$\frac{1}{Pr} (\partial_t \Delta \Delta_{xy} f + \delta (\vec{u} \cdot \nabla \vec{u})) = \Delta^2 \Delta_{xy} f - Ra \Delta_{xy} T \quad (3.7a)$$

$$\frac{1}{Pr} (\partial_t \Delta_{xy} g + \epsilon (\vec{u} \cdot \nabla \vec{u})) = \Delta \Delta_{xy} g \quad (3.7b)$$

$$\frac{1}{Pr} (\partial_t F + \partial_z \langle u_x u_z \rangle_{xy}) = \partial_z^2 F \quad (3.7c)$$

$$\frac{1}{Pr} (\partial_t G + \partial_z \langle u_y u_z \rangle_{xy}) = \partial_z^2 G \quad (3.7d)$$

$$\partial_t T + \Delta_{xy} f + (\vec{u} \cdot \nabla) T = \Delta T \quad (3.7e)$$

While for simplicity the hats (see Section 2.4) have been dropped, the variables  $\vec{u}$  and  $T$  (and the newly introduced  $f$ ,  $g$ ,  $F$  and  $G$ ) still refer to the dimensionless deviations from the stationary solution of (2.29). The Dirichlet boundary conditions for  $\vec{u}$  at the top and bottom plates lead to boundary conditions for  $f$ ,  $g$ ,  $F$  and  $G$  for  $z = \pm \frac{1}{2}$ , such that the boundary conditions for the Boussinesq system read:

$$f(\vec{x}) = \partial_z f(\vec{x}) = g(\vec{x}) = 0 \quad \text{for } \vec{x} \in \Omega_{xy} \times \{-\frac{1}{2}; \frac{1}{2}\} \quad (3.8a)$$

$$F(z) = G(z) = 0 \quad \text{for } z \in \{-\frac{1}{2}; \frac{1}{2}\} \quad (3.8b)$$

$$T(\vec{x}) = 0 \quad \text{for } \vec{x} \in \Omega_{xy} \times \{-\frac{1}{2}; \frac{1}{2}\} \quad (3.8c)$$

In the horizontal directions, the functions  $f$ ,  $g$  and  $T$  must be periodic with period  $\frac{L}{d}$  (in the dimensionless coordinate system):

$$f(x + m \cdot \frac{L}{d}, y + n \cdot \frac{L}{d}, z) = f(x, y, z) \quad \forall m, n \in \mathbb{Z}, \vec{x} \in \Omega \quad (3.9)$$

#### 3.1.2. Galerkin Method

We use a spectral method to find a discrete formulation of the equations (3.7) that can then be solved numerically. The method is here described in abbreviated form, for full detail see [32] and references therein. We consider a differential equation

$$D(u(\vec{x}, t)) = f(\vec{x}, t) \quad (3.10)$$

on the domain  $\bar{\Omega} \times [0; \infty)$  with boundary conditions on  $\partial\Omega$ . A *weak solution*  $\tilde{u}(\vec{x}, t)$  of this differential equation solves the equation only with respect to a discrete set of weighting functions  $\Psi_j : \Omega \rightarrow \mathbb{C}$  ( $j \in \mathbb{N}$ ) by fulfilling the integral equation

$$\int_{\Omega} [D(\tilde{u}(x, t)) - f(x, t)] \overline{\Psi_j(x)} dV = 0 \quad \forall j \forall t. \quad (3.11)$$

We approximate the solution  $u(\vec{x}, t)$  by a limited series of trial functions  $\psi_k : \Omega \rightarrow \mathbb{C}$  ( $k \in \mathbb{N}$ )

### 3. Numerical Scheme for Flow and Particles

that fulfill the boundary conditions on  $\partial\Omega$ :

$$\tilde{u}(\vec{x}, t) \equiv u^N(\vec{x}, t) := \sum_{k=0}^N \hat{u}_k(t) \psi_k(\vec{x}). \quad (3.12)$$

Choosing the weighting functions to be equal to the trial functions ( $\Psi_j = \psi_j$ ) is called a *Galerkin* method. We define an inner product

$$\langle \psi, \phi \rangle := \int_{\Omega} \psi(\vec{x}) \bar{\phi}(\vec{x}) dx. \quad (3.13)$$

To simplify notation and computation, it is common to choose trial functions that are orthogonal and normalized with respect to this inner product, fulfilling

$$\langle \psi_i, \psi_j \rangle = \delta_{ij}. \quad (3.14)$$

The coefficients  $\hat{u}_k(t)$  are the projections of  $\tilde{u}(\vec{x}, t)$  onto the orthonormal basis functions  $\psi_k$ , such that the series (3.12) constitutes a truncated generalized Fourier series:

$$\hat{u}_k(t) = \langle \tilde{u}(t), \psi_k \rangle. \quad (3.15)$$

In the periodic Bénard system, the boundary conditions in the  $x$ - and  $y$ -directions differ from those in the  $z$  direction. While velocity and temperature are fixed on the top and bottom plate, they are periodic in the horizontal directions. These boundary conditions are reflected in the choice of the ansatz functions, which are split up into their  $x$ -,  $y$ - and  $z$ -dependent parts:

$$\psi_k(\vec{x}) = \psi_{k_x}(x) \cdot \psi_{k_y}(y) \cdot \psi_{k_z}(z) \quad (3.16)$$

The total number of modes,  $N$ , is then the product of the number of modes in each direction:  $N = N_x \cdot N_y \cdot N_z$ . The modes for each spatial dimension are again orthogonal and normalized, such that  $\tilde{u}$  can be written as

$$\tilde{u}(\vec{x}, t) = \sum_{k,l,m} \hat{u}_{klm}(t) \cdot \psi_k(x) \cdot \psi_l(y) \cdot \psi_m(z). \quad (3.17)$$

#### Fourier Series for the Horizontal Modes

In the horizontal directions, we fulfill the periodic boundary conditions (see Eq. (3.9) in Section 3.1.1) by choosing Fourier modes of the form

$$E_k(x) := e^{\frac{2\pi i k x}{L}} \quad \text{for } -\frac{N_x-1}{2} \leq k \leq \frac{N_x-1}{2}. \quad (3.18)$$

for the  $x$ -modes, the same definition is used for the  $y$ -modes. These modes are orthogonal and periodic with period  $L$ . A fast transformation between the Fourier coefficients and real space exists, with the Cooley-Tukey FFT algorithm being most commonly used. In every spatial direction, the

### 3.1. Numerical Solution of the Boussinesq Equations

FFT is of order  $\mathcal{O}(N \log N)$ . Additionally, the Fourier series can be easily differentiated:

$$\partial_x^n E_k(x) = \left(\frac{2\pi i k}{L}\right)^n \cdot E_k(x). \quad (3.19)$$

The possibility to express differentiation in terms of a multiplication rapidly increases the accuracy of the scheme, since the spatial derivatives of the partial differential equations can be evaluated up to numerical precision.

#### Sine Functions for Vertical Modes

The vertical components of the functions  $g$ ,  $T$ ,  $F$  and  $G$  have to fulfill the boundary condition  $\psi_k(\pm\frac{1}{2}) = 0$  (see Eq. (3.8) in Section 3.1.1). Therefore, they are developed in sine functions

$$S_k(z) := \sin(k\pi(z + \frac{1}{2})) \quad (3.20)$$

with  $k \in \mathbb{N}^+$ , see Figure 3.1. They are orthogonal on  $[-\frac{1}{2} : \frac{1}{2}]$  and fulfill

$$\partial_z^2 S_k(z) = -k^2 \pi^2 S_k(z). \quad (3.21)$$

Note, however, that these functions are normalized to

$$\int_{\Omega_z} S_k^2(z) dz = \frac{1}{2}. \quad (3.22)$$

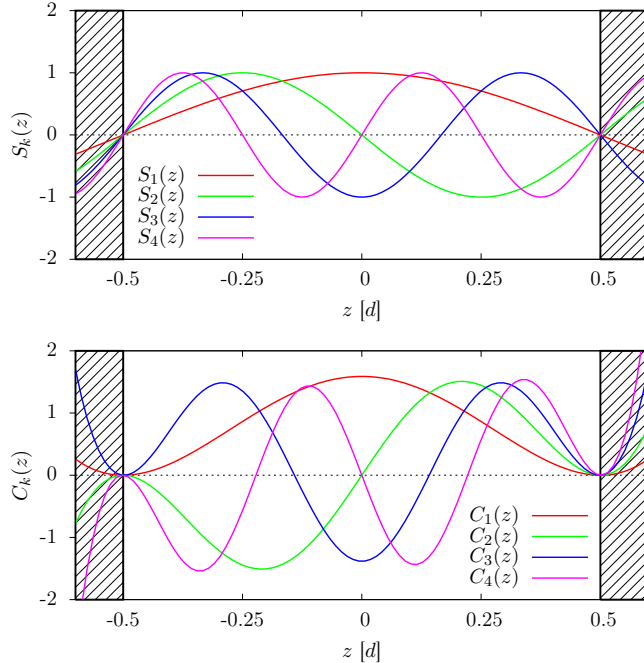


Figure 3.1.: Sine and Chandrasekhar functions for  $1 \leq k \leq 4$ .

### 3. Numerical Scheme for Flow and Particles

#### Chandrasekhar Functions for Vertical Modes

The boundary condition for  $f$  in the vertical direction,  $\psi_k(\pm\frac{1}{2}) = \partial_z \psi_k(z) \Big|_{z=\pm\frac{1}{2}} = 0$  (see Eq. (3.8) in Section 3.1.1) is fulfilled by the Chandrasekhar functions for  $1 \leq k \leq N_z$ :

$$C_k(z) := \begin{cases} \frac{\cosh(\lambda_k z)}{\cosh(\lambda_k \frac{1}{2})} - \frac{\cos(\lambda_k z)}{\cos(\lambda_k \frac{1}{2})} & \text{if } k \text{ is odd} \\ \frac{\sinh(\lambda_k z)}{\sinh(\lambda_k \frac{1}{2})} - \frac{\sin(\lambda_k z)}{\sin(\lambda_k \frac{1}{2})} & \text{if } k \text{ is even} \end{cases} \quad (3.23)$$

The parameter  $\lambda_k \in \mathbb{R}^+$  is the  $\lceil \frac{k}{2} \rceil$ th root for  $\lambda > 0$  of the function

$$(C'(\frac{1}{2}))(\lambda) := \begin{cases} \lambda \cdot (\tanh(\frac{\lambda}{2}) + \tan(\frac{\lambda}{2})) & \text{if } k \text{ is odd} \\ \lambda \cdot (\coth(\frac{\lambda}{2}) - \cot(\frac{\lambda}{2})) & \text{if } k \text{ is even} \end{cases} \quad (3.24)$$

where  $C'_k := \partial_z C_k$ . With these  $\lambda_k$ , the Chandrasekhar function  $C_k(z)$  has exactly  $(k+1)$  roots in  $[-\frac{1}{2} : \frac{1}{2}]$  and fulfills the boundary condition  $C_k(\pm\frac{1}{2}) = C'_k(\pm\frac{1}{2}) = 0$ . The function set  $\{C_k\}$  is orthogonal and normalized. Figure 3.1 shows the first few Chandrasekhar functions. For all Chandrasekhar functions, the following relation holds:

$$\partial_z^4 C_k(z) = \lambda_k^4 C_k(z). \quad (3.25)$$

#### 3.1.3. Pseudo-Spectral Discretization

With the trial functions chosen as described, the fields that describe the system state now read

$$f(\vec{x}, t) = \sum_{k,l,m} \hat{f}_{k,l,m}(t) \cdot E_k(x) E_l(y) C_m(z) \quad (3.26a)$$

$$g(\vec{x}, t) = \sum_{k,l,m} \hat{g}_{k,l,m}(t) \cdot E_k(x) E_l(y) S_m(z) \quad (3.26b)$$

$$F(z, t) = \sum_m \hat{F}_m(t) \cdot S_m(z) \quad (3.26c)$$

$$G(z, t) = \sum_m \hat{G}_m(t) \cdot S_m(z) \quad (3.26d)$$

$$T(\vec{x}, t) = \sum_{k,l,m} \hat{T}_{k,l,m}(t) \cdot E_k(x) E_l(y) S_m(z) \quad (3.26e)$$

We adopt the convention that  $k \in [-\frac{N_x-1}{2} : \frac{N_x-1}{2}]$ ,  $l \in [-\frac{N_y-1}{2} : \frac{N_y-1}{2}]$  and  $m \in [1 : N_z]$ . The Boussinesq equations (3.7) can be reordered in the form of a nonlinear differential equation:

$$B \partial_t V = L V + N(V). \quad (3.27)$$

The solution vector  $V(t)$  is made up of all  $f$ ,  $g$ ,  $F$ ,  $G$  and  $T$  entries,  $B$  and  $L$  are linear differential

operators,  $N(V)$  is a nonlinear operator. The equations are then written as:

$$\partial_t T = \Delta T - \Delta_{xy} f - (\vec{u} \cdot \nabla) T \quad (3.28a)$$

$$\frac{1}{Pr} \Delta \Delta_{xy} \partial_t f = \Delta^2 \Delta_{xy} f - Ra \Delta_{xy} T - \frac{1}{Pr} \delta (\vec{u} \cdot \nabla \vec{u}) \quad (3.28b)$$

$$\frac{1}{Pr} \Delta_{xy} \partial_t g = \Delta \Delta_{xy} g - \frac{1}{Pr} \epsilon (\vec{u} \cdot \nabla \vec{u}) \quad (3.28c)$$

$$\frac{1}{Pr} \partial_t F = \partial_z^2 F - \frac{1}{Pr} \partial_z \langle u_x u_z \rangle_{xy} \quad (3.28d)$$

$$\frac{1}{Pr} \partial_t G = \partial_z^2 G - \frac{1}{Pr} \partial_z \langle u_y u_z \rangle_{xy} \quad (3.28e)$$

In each equation, the left hand side is the time derivative  $B\partial_t V$ , while the last statements of the right hand side constitute the nonlinear term  $N(V)$ . Appendix A.1 shows the discrete equations that solve the weak formulation of the equation system, after integrating the terms from each part over  $\Omega$  with the appropriate weighting function ( $\int_{\Omega} \dots \overline{\psi_{klm}}(\vec{x}) d\vec{x}$ ).

Projecting the nonlinear term  $(\vec{u} \cdot \nabla \vec{u})$  onto all the respective Galerkin functions results in a convolution sum, which is an operation of complexity  $\mathcal{O}(N_x^3 N_y^3 N_z^3)$  in a naive implementation. Orthogonality of the horizontal ansatz functions can be used to reduce the complexity to  $\mathcal{O}(N_x^2 N_y^2 N_z^3)$ ; this however is still prohibitively expensive for large system sizes. Hence, we use the fast Fourier transform in the  $x$ - $y$ -plane (which is of complexity  $\mathcal{O}(N_x N_y N_z \log N_x N_y)$ ) to transform our system to real space, where the evaluation of the nonlinear term for the equations is of order  $\mathcal{O}(N_x N_y N_z^3)$ . The Chandrasekhar functions of the vertical direction do not provide a simple transform of that kind, and are also not orthogonal to their derivatives, such that the  $\mathcal{O}(N_z^3)$ -term in the complexity cannot be easily avoided. The solution here is to keep  $N_z$  as low as possible; this approach however limits the applicability of the simulations to low Rayleigh numbers.  $N_z = 2$  is the lowest number for which physically reasonable results can be expected close to convection onset.

### 3.1.4. Penalization

The Galerkin method is a very efficient simulation method due to the implicit incorporation of the boundary conditions into the simulation scheme. The drawback of this approach is that the scheme lacks flexibility in adapting to different boundary conditions, as good ansatz functions cannot simply be found for all boundary geometries and conditions. In our case, the spectral decomposition into Fourier modes is tailored to a periodic, rectangular system in the horizontal direction with a constant system height. While the constant vertical height is a characteristic property of the Bénard cell and correspondingly used in theoretical considerations and experiments, periodicity in the horizontal directions will not be provided in all Bénard systems, especially not in experimental setups. Common experimental geometries are fixed-boundary rectangles and circular regions (examples can be found in [19, 21]).

We will generally use a periodic system nonetheless, which avoids runtime overheads and possibly simulation artefacts that could result from boundary effects. Still, in evaluations that are designed to be compared to results from other publications, we introduce no-slip boundary conditions for the vertical side walls via an  $L^2$ -penalization scheme[1]. The scheme tries to maintain zero velocity and temperature fluctuations from the stationary state (see Eq. (2.30) in Section 2.4) by imposing a linear drag term onto these fluctuations at all locations outside the intended fluid volume  $\Omega^f$ . For

### 3. Numerical Scheme for Flow and Particles

fluid velocity, this corresponds to a viscous resisting force inside a porous medium; the temperature experiences conductive heat exchange with a large reservoir.

We restrict ourselves to fluid volumes  $\Omega^f \subset \Omega$  with vertical side walls. With the penalization parameter  $\eta \in \mathcal{R}^+$ , we define the penalization function  $P(\vec{x})$  as

$$P(\vec{x}) := \begin{cases} 0 & \text{if } \vec{x} \in \Omega^f \\ \frac{1}{\eta} & \text{else.} \end{cases} \quad (3.29)$$

If the side walls are vertical,  $P(\vec{x}) = P(x, y)$ . With this function and a uniform penalization for velocity and temperature, we can write the equations of fluid motion (3.28) as:

$$\frac{1}{Pr} \Delta \Delta_{xy} \partial_t f = \Delta^2 \Delta_{xy} f - Ra \Delta_{xy} T - \frac{1}{Pr} \delta (\vec{u} \cdot \nabla \vec{u}) - P(\vec{x}) \delta \cdot \vec{u} \quad (3.30a)$$

$$\frac{1}{Pr} \Delta_{xy} \partial_t g = \Delta \Delta_{xy} g - \frac{1}{Pr} \epsilon (\vec{u} \cdot \nabla \vec{u}) - P(\vec{x}) \epsilon \cdot \vec{u} \quad (3.30b)$$

$$\frac{1}{Pr} \partial_t F = \partial_z^2 F - \frac{1}{Pr} \partial_z \langle u_x u_z \rangle_{xy} - \langle P(\vec{x}) \vec{e}_x \cdot \vec{u} \rangle_{xy} \quad (3.30c)$$

$$\frac{1}{Pr} \partial_t G = \partial_z^2 G - \frac{1}{Pr} \partial_z \langle u_y u_z \rangle_{xy} - \langle P(\vec{x}) \vec{e}_y \cdot \vec{u} \rangle_{xy} \quad (3.30d)$$

$$\partial_t T = \Delta T - \Delta_{xy} f - (\vec{u} \cdot \nabla) T - P(\vec{x}) T \quad (3.30e)$$

Note that  $P(\vec{x})$  is discontinuous, which can cause issues in the mathematical description of existence and uniqueness of solutions to (3.30). For details, see [32] and references therein. Expressing a discontinuous function in a Fourier series will lead to an overshoot at the discontinuity (Gibbs phenomenon), which we avoid by not evaluating the penalization terms with the linear operator, but applying the penalization in real space during evaluation of the nonlinear operator. Thus, we avoid adverse effects from the jump in  $P(\vec{x})$  in the discrete formulation of the equations that implement the Galerkin scheme.

The error of the scheme can be shown to scale with  $\mathcal{O}(\eta^{3/4})$  for the  $L^2$ -penalization[1]. There is a  $H^1$  penalization scheme that can be shown to converge with  $\mathcal{O}(\eta)$ , however the  $L^2$  penalization has proven more efficient and practical in our setting. Throughout the simulations, we use a penalization parameter on the order of  $\eta \sim 0.01$ .

#### 3.1.5. Dealiasing

In the nonlinear operator, working with the truncated Fourier series will cause aliasing effects. Nonlinear effects in the lower frequencies will have a nonzero contribution to high frequencies, which are not sampled by the finite number of coefficients, and thus look like low frequency contributions in the finite spectrum. Consider a multiplication of two fields  $\tilde{u}, \tilde{v}$  (with  $k', k'' \in [-\frac{N_x-1}{2} : \frac{N_x-1}{2}]$ ), that are written as

$$\tilde{u}(x) = \sum_{k'} \hat{u}_{k'} E_{k'}(x) \quad ; \quad \tilde{v}(x) = \sum_{k''} \hat{v}_{k''} E_{k''}(x). \quad (3.31)$$

### 3.1. Numerical Solution of the Boussinesq Equations

The Galerkin method for mode  $k$  has the integral (with  $x_j = \frac{jL}{N_x}$ )

$$\langle E_k, \tilde{u}\tilde{v} \rangle = \frac{1}{|\Omega|} \int_{\Omega} \sum_{k', k''} \hat{u}_{k'} \hat{v}_{k''} e^{\frac{2\pi i x_j}{L} (k' + k'' - k)} dx = \sum_{k' + k'' = k} \hat{u}_{k'} \hat{v}_{k''}. \quad (3.32)$$

Performing a discrete Fourier transform  $\widehat{uv}_k$  will result in terms like:

$$\widehat{uv}_k = \frac{1}{N_x} \sum_{j=0}^{N_x-1} \tilde{u}(x_j) \tilde{v}(x_j) = \sum_{k' + k'' = k} \hat{u}_{k'} \hat{v}_{k''} + \sum_{k' + k'' = k \pm N_x} \hat{u}_{k'} \hat{v}_{k''}. \quad (3.33)$$

Due to the finite  $N_x$ , terms corresponding to high frequencies are projected back into the finite frequency spectrum, creating the aliasing error that cannot be neglected. It can be avoided by applying the *Orszag Two-Thirds Rule*[8]: By setting the coefficients to zero for the outer third of the frequency spectrum, the inner two thirds of the spectrum will not suffer from aliasing, while the aliasing terms that occur in the outer third will be reset with every time step.

#### 3.1.6. Time Stepping Scheme

As discussed in Section 3.1.3 and Appendix A.1, the terms for the velocity and temperature fields can be expressed as sums over their spectral modes, and discrete linear and nonlinear operators can be derived, which form the evolution equation

$$B\partial_t V = LV + N(V). \quad (3.34)$$

By only considering a finite number of modes in the spatial directions, the discrete linear operators  $B$  and  $L$  can be expressed as sparse matrices, and the nonlinear operator  $N(V)$  can be solved with an efficient algorithm. This formulation, however, is still continuous in time, and a discrete approximation must be found for the time stepping. We employ an implicit-explicit time-stepping scheme, which for a time step  $dt$  has the form

$$\tilde{V}_{t+1} = \frac{3dt}{2} \cdot B^{-1} \cdot N(V_t) - \frac{dt}{2} \cdot B^{-1} \cdot N(V_{t-1}), \quad (3.35a)$$

$$V_{t+1} = (1 - dt \cdot B^{-1} L)^{-1} [V_t + \tilde{V}_{t+1}]. \quad (3.35b)$$

The scheme combines an implicit Euler-step for the linear operator with an explicit two-step Adams-Bashforth method, which both have accumulated errors of order  $\mathcal{O}(dt)$ . For the stability of the numerical scheme, it is generally advantageous to use an implicit method, which can be done for the linear operator due to its simple block-diagonal structure. However, the nonlinear operator cannot be inverted as easily, hence the Adams-Bashforth method is employed in order to first arrive at an intermediate solution of the nonlinear equation

$$B\partial_t V = N(V) \quad (3.36)$$

### 3. Numerical Scheme for Flow and Particles

(in vector  $\tilde{V}_{t+1}$ ), which is then fed into the implicit solver of the linear problem

$$B\partial_t V = LV \quad (3.37)$$

that in this case is implemented via an implicit Euler step. The implicit Euler method is a stable, first-order scheme, which will generally damp down the solution. Schemes with higher consistency order might improve precision, but limit the maximum permissible time step at a high spatial resolution.

## 3.2. Particle Tracing

Particle motion depends only on the velocity field of the fluid and can be evaluated in parallel for different particles. Massless tracer particles follow the trajectory described by the equation of motion for a diffusing particle (Eq. (2.50)),

$$\frac{d\vec{x}}{dt} = \vec{u}(\vec{x}, t) + \frac{\vec{\eta}(t)}{dt}. \quad (3.38)$$

The effect of diffusive motion is generally much smaller than that of advection in any time step, such that its influence on the position over  $dt$  will be neglected; and independent of the particle's location, such that it can be determined without considering the effect of advection. We therefore assume the diffusion process to be independent of the advection. With the position increments due to advection  $d\vec{x}$  and diffusion  $\vec{\eta}$ , the new position  $\vec{x}(t + dt)$  of a particle can be written as

$$\vec{x}(t + dt) = \vec{x}(t) + d\vec{x}(\vec{x}, t) + \vec{\eta}(t). \quad (3.39)$$

### 3.2.1. Implementation of Particle Advection

The spectral formulation of the velocity field enables us to reconstruct the fluid velocity  $\vec{u}(\vec{x}, t)$  at any location with high precision. To make use of the complex-to-real fast Fourier transform, we restrict ourselves to a grid of size  $2(N_x - 1) \times N_y$  in the horizontal direction, and use 128 discrete levels in direction of  $z$ . Trilinear interpolation is then used to estimate the fluid velocity for a location between the grid points.

Each time step consists of one advection step with a modified 4th order Runge-Kutta time stepping method, and the diffusion step. Let  $\vec{x}_0 \in \mathbb{R}^3$  be the initial position of a particle at time  $t_0$ . Then, via trilinear interpolation over the velocity  $\vec{u}(\vec{x}, t_0)$ , the following quantities are calculated for a time step of  $dt$ :

$$\begin{aligned} d\vec{x}_a &:= dt \cdot \vec{u}(\vec{x}_0, t_0) & d\vec{x}_b &:= dt \cdot \vec{u}(\vec{x}_0 + \frac{1}{2}d\vec{x}_a, t_0) \\ d\vec{x}_c &:= dt \cdot \vec{u}(\vec{x}_0 + \frac{1}{2}d\vec{x}_b, t_0) & d\vec{x}_d &:= dt \cdot \vec{u}(\vec{x}_0 + d\vec{x}_c, t_0) \\ d\vec{x} &= \frac{1}{6}(d\vec{x}_a + 2 \cdot (d\vec{x}_b + d\vec{x}_c) + d\vec{x}_d) \end{aligned}$$

The particle position after the time step is  $\vec{x}_1 = \vec{x}_0 + d\vec{x}$ . The traditional Runge-Kutta scheme would require the velocity fields to be evaluated at intermediate times as well ( $\vec{u}(..., t_0 + \frac{dt}{2})$  etc.),

which is computationally expensive here due to the effortful construction of the velocity field. However, the velocity field changes on a time scale much larger than the flow velocity itself, such that the influence of this change on the particle trajectories is small compared to the effects of advection at the time steps we use. The accumulated error of the time stepping scheme is  $\mathcal{O}(dt^4)$ , much smaller than that of the time stepping scheme that calculates the velocity fields in the first place.

### 3.2.2. Implementation of Brownian Diffusion

According to Section 2.6, we model the diffusion process with a delta-correlated Gaussian noise  $\vec{\eta}(t)$  that is being added to the position each time step, as a means of sampling the probability density for its location. Let  $X_{\text{normal}}$  be a Gaussian distributed random variable with mean  $\mu_0 = 0$  and standard deviation  $\sigma_0 = 1$ . Then, each direction component of  $\vec{\eta}$  at a time-step  $dt$  is

$$\eta_i = \sigma \cdot X_{\text{normal}} = \sqrt{2\mathcal{L} \cdot dt} \cdot X_{\text{normal}} \quad \text{for } i \in \{x, y, z\}, \quad (3.40)$$

with position and time in dimensionless coordinates. This scheme makes use of the fact that the noise is uncorrelated for the orthogonal Cartesian directions  $\vec{e}_x$ ,  $\vec{e}_y$ ,  $\vec{e}_z$ , so that a random variable can be drawn from the normal distribution separately for each dimension.

## 3.3. Parallelized Implementation of the Simulation Scheme

We will here briefly sketch the implementation of the Galerkin scheme that solves the Boussinesq equations, putting emphasis on those features of the implementation that were added after the work of Zudrop[32] and are thus not discussed there.

The implementation is designed to make use of *Graphics Processing Unit* (GPU) devices, which were originally designed to render images for the large discrete pixel grid of a computer display. For that purpose, they are equipped with a large number of SIMD<sup>1</sup>-parallel processing cores and large, high bandwidth memory. Memory latency is hidden by a fine-grained switching between threads on one processing core. We use GPU devices of the Nvidia GeForce and Tesla series with a device memory of up to 6 GB and address them with the CUDA programming model that is based upon the C++ programming language.

### 3.3.1. GPU Architecture and Computing Model

A GPU of the Kepler architecture, which we use, consists of a fixed number of functionally identical *CUDA multiprocessors* (Figure 3.2), which each have their own instruction scheduler and a small block of fast memory. All multiprocessors have high-bandwidth access to the *Device Random-Access Memory* (DRAM). Tasks are assigned to the individual multiprocessors by the GPU control logic, such that task parallelism is possible among them. Each multiprocessor consists of a large

---

<sup>1</sup>SIMD stands for *Single Instruction, Multiple Data*; the same algorithm is being applied in parallel to different sets of data, e.g. a shading algorithm being executed on data for different pixels. The CUDA computing model allows for thread-dependent execution paths, the developer calls this SIMT (*Single Instruction, Multiple Threads*)[14]. GPUs also allow for a limited degree of task parallelism, which we do not use though.

### 3. Numerical Scheme for Flow and Particles

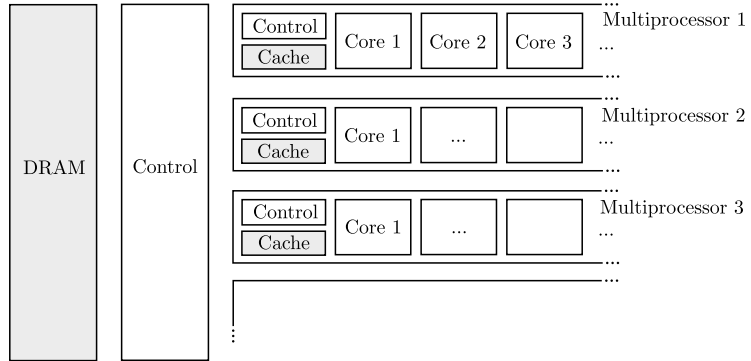


Figure 3.2.: Layout of a GPU: Tasks are distributed among multiprocessors, which each have multiple cores, but limited control hardware and local memory. Data transfers from one multiprocessor to another are only possible via the large device RAM (DRAM)[14].

number of *CUDA cores*, which process one thread at a time, but can switch quickly between different threads: Since multiple sets of registers are available per core, switches between threads require virtually no memory transactions. The fast switching between threads is used to hide latencies in accessing global memory; for maximum performance, we assign multiple threads to each core.

The distribution of parallel tasks on the hardware level is reflected in the CUDA extension to C++: The high number of threads is laid out in a *grid* of *thread blocks*, where all blocks have the same size and each block is running on one multiprocessor<sup>2</sup>. The thread inside a block, and the block inside the grid, are each indexed by three integer numbers that are available to a thread via static predefined variables. This reflects the two- or three-dimensional pixel grids in image rendering that GPUs were originally designed for, and is helpful in many general purpose applications like linear algebra. One-dimensional indexing can be achieved by setting the block and grid size to one in the second and third dimension. The maximum block and grid sizes per dimension are however limited, and to achieve more flexibility of distributing the degrees of freedom among the dimensions, we use a linear indexing that matches the memory layout of our data containers (see Section 3.3.3).

While the total instruction throughput is higher for the parallel processors than for the CPU of the host machine, a single thread will be executed much more slowly on the GPU than on the CPU due to the fast caches and sophisticated control logic of the latter. We therefore use a heterogeneous programming model where sequential parts of the algorithm will be executed on the CPU, and control will be handed over to the GPU only for those steps that benefit from parallel execution (Figure 3.3). These include the application of the different linear and nonlinear operators on the Galerkin modes for the temperature and velocity field, and the diffusion and time-stepping scheme for the tracer particles. As GPU kernel calls have a very high latency, we try to minimize the total number of calls to the GPU. The CUDA compiler accepts code for the CPU (*host code*) and for the GPU (*device code*) in one file, but separates host and device code at compile time

---

<sup>2</sup>Threads in a block are divided into *warps* of 32 threads each, and all threads of a warp run in parallel on the instruction level. This is important for local inter-thread communication, which however is not necessary in our application.

### 3.3. Parallelized Implementation of the Simulation Scheme

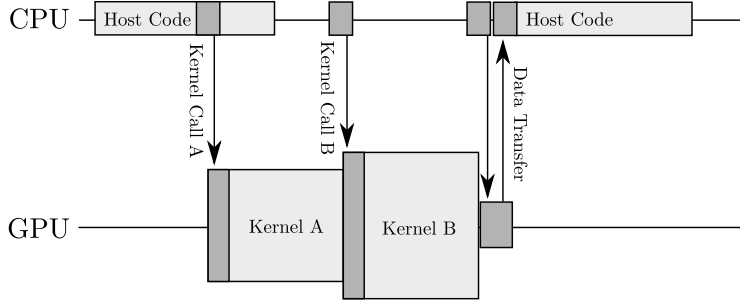


Figure 3.3.: Control flow between CPU and GPU. In this example, the host calls two kernels and transfers data from device to host. Dark shaded regions represent management and communication between device and host. Kernels can be started with different numbers of parallel threads, represented by the width of the life line on the GPU side. Asynchronous data transfer is possible for some CUDA devices, but in general, data transfers will block the host and device.

based on keywords in the function header. Functions marked with `__host__` (or unmarked) will be compiled as C/C++ functions for the CPU, while `__global__` and `__device__` functions will be compiled for the GPU. A *global* function is called a *kernel*, and can only be called from the host. Special configuration arguments are required in this call, which specify the grid size and block size, i.e. the total number of threads that will be started on the GPU and their distribution among the multiprocessors. *Device* functions are subroutines that can be called from kernels (and other device functions), and cannot be configured.

To avoid a bottleneck in the bandwidth of the PCIe bus that connects CPU and GPU, the data for the fluid velocity ( $f$ ,  $g$ ,  $F$  and  $G$ ) and temperature, and the positions of the tracer particles are stored in device memory for the whole simulation. They will be initialized once during startup, and will only be copied back to the host RAM for evaluation and output to the file system. To further reduce the number of memory transfers, particle tracks are buffered in DRAM and only written to the harddisk when the buffer is full.

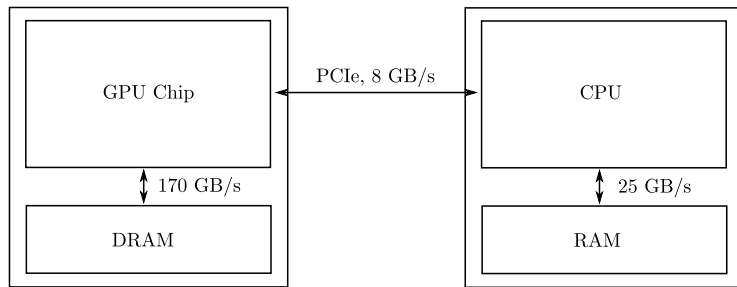


Figure 3.4.: Memory access and bandwidths for data transfers between CPU and GPU. The latency for communication between host and device is orders of magnitude larger than for accessing local memory[14]. We therefore store the simulation data on the device, and minimize the number of kernel calls.

### 3.3.2. Initialization and Simulation Loop

The simulation package relies on an object-oriented design by providing functionality in self-contained classes that implement data management, file output and operators of the numerical scheme. The main routine (Algorithm 1) is equipped with an input parser that interprets command-line arguments which specify details of the simulation geometry, physical simulation parameters, initial conditions and outputs. The initial velocity and temperature fields can either be entered into the simulation as binary files, or imprinted to the system by small temperature perturbations in the resting fluid. Any temperature perturbation includes a small random fluctuation, based on a random number generator whose seed can be set via an input parameter. Different compile flags exist for periodic and bounded systems, and for penalization masks (see Section 3.1.4) of cylindrical and other domains. Particle positions are being initialized based on a set of input parameters.

The simulation loop consists of the time stepping for the velocity and temperature fields, particle advection and diffusion in the newly computed velocity field, and file output for the flow field and particle positions. The cleanup phase after the simulation loop writes the system state for velocity and temperature to a set of binary files, writes out the remaining buffer content, and deallocates all memory.

### 3.3.3. Data Containers

All data fields are stored in contiguous memory in the form of vectors. For easy access, they are organized in tensor-like containers that allow access by multiple indices, where the mapping of the indices to the memory position is designed to optimize GPU memory access patterns. For a

---

**Algorithm 1:** Simulation loop in `main.cu`.

---

```
// Initialization
process inputs;
set working directory and GPU device;
if input files provided then read system from input files else
| allocate device memory;
| set initial conditions;
end
initialize operators for velocity/temperature calculation;
initialize operators for time stepping;
if particles should be traced then initialize particle tracer;
// Simulation Loop
for time step do
| step time for velocity/temperature field;
| if particle tracer initialized then step time for particles;
| measure and store observables;
end
// Cleanup
measure and store observables (clear buffers);
free memory;
```

---

### 3.3. Parallelized Implementation of the Simulation Scheme

three-dimensional field of size  $N_x \times N_y \times N_z$  with indices

$$(k, l, m) \in [0 : N_x - 1] \times [0 : N_y - 1] \times [0 : N_z - 1], \quad (3.41)$$

the position of an item  $(k, l, m)$  in the memory field is

$$p_{klm} = k + l \cdot N_x + m \cdot N_x \cdot N_y. \quad (3.42)$$

This choice of memory access pattern allows for a simple separation of the memory into  $N_z$  contiguous memory blocks for the different  $z$ -layers, which we use when Fourier-transforming the temperature and velocity fields in  $x$  and  $y$  for the nonlinear operator.

The containers are implemented as templated classes, which can be instantiated for real and complex entries at single and double precision. Two types of container classes exist: One for data in host RAM, one for device memory. The container for device memory consists of metadata like the container size, which is stored in RAM, and a pointer to a memory section in DRAM where the actual data can be found. This allows the algorithm to sequentially prepare all simulation steps on the CPU, and then forward all the highly parallelizable operations on the simulation data to the device without the need for large memory transfers.

A special container class stores the coefficients from the overlap integrals of the Chandrasekhar and Sine functions, that appear in the discrete formulation of the Galerkin scheme (see Appendix A.1). Analytic solutions for the integrals exist, which are precomputed once during initialization and then made available to the modules that use them. The coefficients are stored in RAM and passed to the GPU as parameters of kernel calls.

#### 3.3.4. Time Stepping Operators

The time stepping scheme (Section 3.1.6) uses three operators: The *nonlinear operator*  $N(V)$ , the *inverse time-stepping operator*  $B^{-1}$ , and the *implicit linear operator*  $(1 - dt B^{-1} L)^{-1}$  which already includes an implicit Euler time step. The discrete form of the operators can be found in Appendix A.1.

The nonlinear operator makes use of the CuFFT library[12] to Fourier transform the spectral representations of  $f$ ,  $g$  and  $T$  to real space and back. Only  $N_x/2 + 1$  modes in  $x$ -direction need to be stored in Fourier space due to symmetry in the complex Fourier coefficients. For the cylindrical system, the penalization mask is being applied in real space. For an efficient transform, we always choose  $N_x$  and  $N_y$  as powers of two. We normalize the FFTs when we transform from real to Fourier space, with a normalization constant of

$$\frac{1}{N_x N_y}. \quad (3.43)$$

The implicit linear operator for  $g$ ,  $F$  and  $G$  can be directly implemented in kernels, since the implicit matrix is diagonal. For  $f$  and  $T$ , the operator is block diagonal. The blocks are being precomputed by the CPU in the initialization phase, with matrix operations being supplied by the *GNU Scientific Library*, and stored in DRAM on the GPU. A special code branch exists for

### 3. Numerical Scheme for Flow and Particles

$N_z = 2$ , where diagonality of the operator allows for dense storage and faster computation. The same approach is used for the inverse time-stepping operator  $B^{-1}$ , which follows the evaluation of the nonlinear operator.

The three operators are managed by the *implicit-explicit time-stepping operator*, which implements the Adams-Bashforth routine for the explicit time-stepping of the nonlinear terms by always storing an intermediate solution vector from the previous time step,  $B^{-1}N(V_{t-1})$ , to get the explicit increment  $\tilde{V}_{t+1}$  for the next time step. For the first time step, when no result for the previous step is available, this method is replaced by an explicit Euler time step

$$\tilde{V}_1 = dt \cdot B^{-1} \cdot N(V_0). \quad (3.44)$$

Note that, since the system of Rayleigh-Bénard convection is chaotic, this minor change may alter the outcome of a simulation that is restarted from an early snapshot.

#### 3.3.5. Particle Tracer

The particle tracer maintains a buffer of particle trajectories, which are stored in device RAM and regularly transferred to host RAM, from where they are written to a binary file. In every time step, the velocity field is calculated in 128 equidistant vertical positions from the spectral representation of the potentials  $f$ ,  $g$ , and the mean flows  $F$  and  $G$ . The vertical resolution of the velocity field is two orders of magnitude higher than the number of vertical modes, whereas in the horizontal plane, the number of grid points corresponds to the number of Fourier modes of  $f$  and  $g$ .

Particles that enter the top and bottom boundary layer or cross the top or bottom plates during a time step are reflected back into the fluid. For this reflection, we assume the particles to have a radius of  $10^{-3} d$ , which sets the maximum allowed distance from the system midplane to

$$d_p = \frac{1}{2} - 10^{-3}. \quad (3.45)$$

In the periodic system, particles are traced in the horizontally infinite domain

$$\bar{\Omega}_p = \mathbb{R}^2 \times [-d_p; d_p] \quad (3.46)$$

and their positions are projected into the periodic fluid domain  $\bar{\Omega}_f$  only for evaluating the fluid velocity. The particle domain in the cylindrical system is

$$\bar{\Omega}_{p,cyl} = [0; L] \times [0; L] \times [-d_p; d_p] \quad (3.47)$$

and particles may leave the fluid domain  $\Omega_f$  by diffusion. We thus initialize particle positions far from the side boundaries in the bounded system, and limit the simulation times such that particles that reach the side walls do not contribute significantly to the simulation results. For long-time simulations, we only consider periodic systems, where dispersion properties can be followed over long times. Note that in this case, long-range correlations from the periodic structure of the velocity field need to be taken into account.

Algorithm 2 shows in pseudocode how we perform the trilinear interpolation. It combines the

**Algorithm 2:** Trilinear interpolation in `particle_tracer.cu`.

---

```

// Get position in coordinates of velocity grid
xgrid := Nx · (x/Lx − ⌊x/Lx⌋);
ygrid := Ny · (y/Ly − ⌊y/Ly⌋);
zgrid := 127 · (z + dp)/(2dp);
// Get lower and higher grid indices
\underline{x} := ⌊xgrid⌋;
\underline{y} := ⌊ygrid⌋;
\underline{z} := ⌊zgrid⌋;
\underline{\bar{x}} := (\underline{x} + 1 < Nx)?(underline{x} + 1) : 0;
\underline{\bar{y}} := (\underline{y} + 1 < Ny)?(underline{y} + 1) : 0;
\underline{\bar{z}} := \underline{z} + 1;
// Linear average in x-direction
w := xgrid − \underline{x};
\underline{\vec{v}}00 := (1 − w) · \vec{v}[\underline{x}, \underline{y}, \underline{z}] + w · \vec{v}[\underline{\bar{x}}, \underline{y}, \underline{z}];
\underline{\vec{v}}01 := (1 − w) · \vec{v}[\underline{x}, \underline{y}, \underline{\bar{z}}] + w · \vec{v}[\underline{\bar{x}}, \underline{y}, \underline{\bar{z}}];
\underline{\vec{v}}10 := (1 − w) · \vec{v}[\underline{x}, \underline{\bar{y}}, \underline{z}] + w · \vec{v}[\underline{\bar{x}}, \underline{\bar{y}}, \underline{z}];
\underline{\vec{v}}11 := (1 − w) · \vec{v}[\underline{x}, \underline{\bar{y}}, \underline{\bar{z}}] + w · \vec{v}[\underline{\bar{x}}, \underline{\bar{y}}, \underline{\bar{z}}];
// Linear average in y-direction
w := ygrid − \underline{y};
\underline{\vec{v}}0 := (1 − w) · \vec{v}00 + w · \vec{v}10;
\underline{\vec{v}}1 := (1 − w) · \vec{v}01 + w · \vec{v}11;
// Linear average in z-direction
w := zgrid − \underline{z};
\underline{\vec{v}}particle := (1 − w) · \vec{v}0 + w · \vec{v}1;

```

---

projection of the particle positions into the fluid simulation volume with a smooth interpolation scheme between 8 velocity vectors at the nearest grid points. As it is part of the Runge-Kutta scheme, four iterations of the interpolation are needed for every time step. We tested an alternative approach of reconstructing the velocity field directly at the particles' positions by adding up the individual contributions from the ansatz functions, but found the negative impact on performance to outweigh the increase in precision.

The routine for the diffusion of particles uses the CUDA CuRAND library[13] and specifically its function `curand_normal()`. We reach a high degree of parallelism by operating one random number generator for each particle and spatial direction ( $x$ ,  $y$ ,  $z$ ). The generators are initialized and their states stored in DRAM, one random number is generated from each generator in each time step.

### 3.3.6. Output Methods

Several modules are provided for output of simulation data. A binary writer writes RAM-based data containers to files, and can also read them back into memory. This writer is used especially to store snapshots of the fluid state. In addition, data fields can be written in formats readable by the `vtk` and `gnuplot` plotting programs. Particle tracks are written in a special binary file format, which in addition to the positions of the particles at the different time steps also maintains a record of metadata like the framerate and a descriptor string.

### 3. Numerical Scheme for Flow and Particles

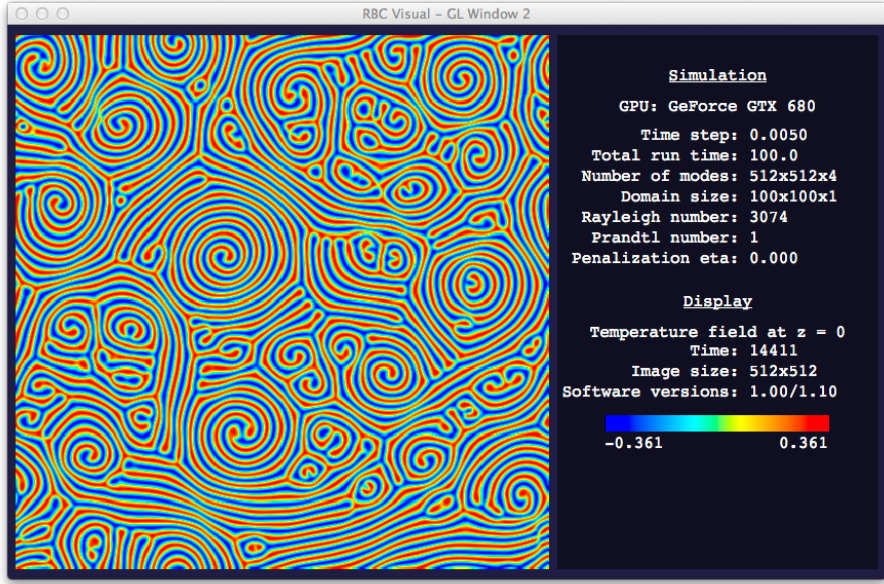


Figure 3.5.: Graphical frontend of the UDP server module that we use in the simulation package for real-time output of the midplane temperature field and particle density.

A server module can be compiled into the simulation, which transmits live images of the running simulation to a graphics display (Fig. 3.5). The server is non-blocking and uses the UDP protocol to minimize an impact of the real-time output on performance. The frontend is written in Qt and uses the `QPainter` class to draw an updated image of the simulation in regular time intervals.

#### 3.3.7. Performance Optimizations

We optimized the simulation for runtime performance by identifying ways to utilize the existing computational capabilities of the GPU efficiently. As each kernel call requires first a nontrivial communication between CPU and GPU, and then the scheduling of the task to the multiprocessors, time can be saved by merging functionalities of several kernels into one, and removing kernel calls that have no effect for the given input parameters. On many occasions, data fields are being scaled by multiplying each entry with a constant factor, right after another, more complex routine has been performed. By including the scaling by a constant factor to this first routine, the second kernel call and its overhead can be avoided, at the expense of one additional argument and operation in the first kernel which has a comparatively small effect on runtime. A similar improvement is being achieved by executing the scaled addition

$$A := A + c \cdot B \quad (3.48)$$

for data fields  $A$  and  $B$ , which appears in the evaluation of the nonlinear operator, only for  $c \neq 0$ . In the simulation,  $c$  is often the value some overlap integral, which vanishes if the integrand is odd in the symmetric vertical simulation domain.

We also optimized memory access patterns on the device, where we reduced the total number

### 3.3. Parallelized Implementation of the Simulation Scheme

of device memory accesses by storing intermediate results in registers, especially when composing complex numbers from their real and imaginary part: Instead of

```
output[index].x = input[index].x + factor.x * to_add[index].x  
                  - factor.y * to_add[index].y;  
output[index].y = input[index].y + factor.x * to_add[index].y  
                  + factor.y * to_add[index].x;
```

with 8 accesses to device-global memory, we write

```
CUDA_FLOAT entry = input[index];  
CUDA_FLOAT add_entry = to_add[index];  
entry.x += factor.x * add_entry.x - factor.y * add_entry.y;  
entry.y += factor.x * add_entry.y + factor.y * add_entry.x;  
output[index] = entry;
```

with only 3 global memory accesses. We use complex number types only when they are needed, and thus reduce memory and bandwidth usage. The kernels in our simulation scheme are relatively short, such that register pressure is low and intermediate results can be stored in registers instead of global memory. Compile-time flags are being used to determine the floating-point precision, enable the penalization scheme and set periodic boundaries for the particle tracer, since these functionalities would otherwise require much additional runtime effort.



## 4. Particle Transport in Spiral Defect Chaos

This chapter lists and discusses the results that we obtained by numerical simulations of the incompressible Boussinesq equations and the tracing of diffusive particles in the resulting flow fields. In Section 4.1, we consider the transition from Ideal Straight Rolls to fully developed Spiral Defect Chaos with increasing  $\varepsilon$  for large aspect ratio systems, discussing the onset of Spiral Defect Chaos. The Spiral Defect Chaos state creates a complex pattern, which however consists of simple primitives like rolls, defects and spirals. We report qualitative observations and quantitative measurements of passive scalar transport in flow fields representing those primitive patterns in Section 4.2. From particle transport in these static flow fields, we turn to dynamic Spiral Defect Chaos in bounded and periodic systems. We investigate in Section 4.3 the effective diffusivity of a passive scalar represented by a high number of diffusive particles, and its dependence on the diffusivity of the individual particles. The enhancement of passive scalar diffusivity by the convective motion motivates an investigation of Lagrangian particle dispersion under the influence of advection and diffusion. In Section 4.4, we discuss its dependence on particle diffusivity and Rayleigh number, and investigate how the dynamic flow field enhances the dispersion. We attempt in Section 4.5 to extract information about the irreversibility of the spatiotemporal dynamics from the acceleration statistics of Lagrangian particle trajectories in the convective flow field.

### 4.1. Onset of SDC in Large Systems

Large aspect ratio Bénard systems have been observed to show Spiral Defect Chaos even at low Rayleigh numbers[5]. We want to investigate the transition to SDC for large aspect ratios in the low Rayleigh number regime. Since the transition time into the dynamic equilibrium grows with the system size, a measure of which is the horizontal thermal diffusion time

$$\tau_h = \tau_v \cdot \frac{L^2}{d^2}, \quad (4.1)$$

this investigation is a computationally challenging task.

Unlike noted by Zudrop[32], initializing a system with straight rolls and a dislocation pair does not suffice to create SDC in a system. The additional roll pair that this method inserts will generally just grow or shrink along its orientation, depending on the preferred wave number of ISR. Zudrop likely observed spatiotemporal chaos after erroneously starting the system with an initial wave number  $q = \frac{2\pi}{d}$ , far beyond the region of stable rolls. Under these initial conditions, defects would form immediately, and relaxation to straight rolls would take a long time especially for large aspect ratio systems. Still, finding spirals in the resulting patterns will be somewhat indicative of whether SDC can be expected for long times.

#### 4. Particle Transport in Spiral Defect Chaos

The figures on the following pages show the midplane temperature field of large systems after initialization times of  $t_{\text{init}} = 60000 \tau_v$  from initial conditions with small random perturbations. At  $\varepsilon = 0.2$  (Figure 4.1), the whole system quickly reaches the ISR state, with just a few dislocations remaining. The dislocations have the tendency to form dislocation lines, that have the appearance of local low-angle grain boundaries. The shown configuration has a slow mean flow in the negative  $y$  direction, which moves the dislocations along. Climbing of dislocations along the roll direction is being observed more frequently than gliding between the convection rolls, and no new dislocations get created with time. It is possible that for very long times, even the existing dislocations annihilate and the system reaches a perfect ISR state, but simulations could only be run for just above one horizontal thermal diffusion time due to the large system size, and defects were moving and annihilating very slowly.

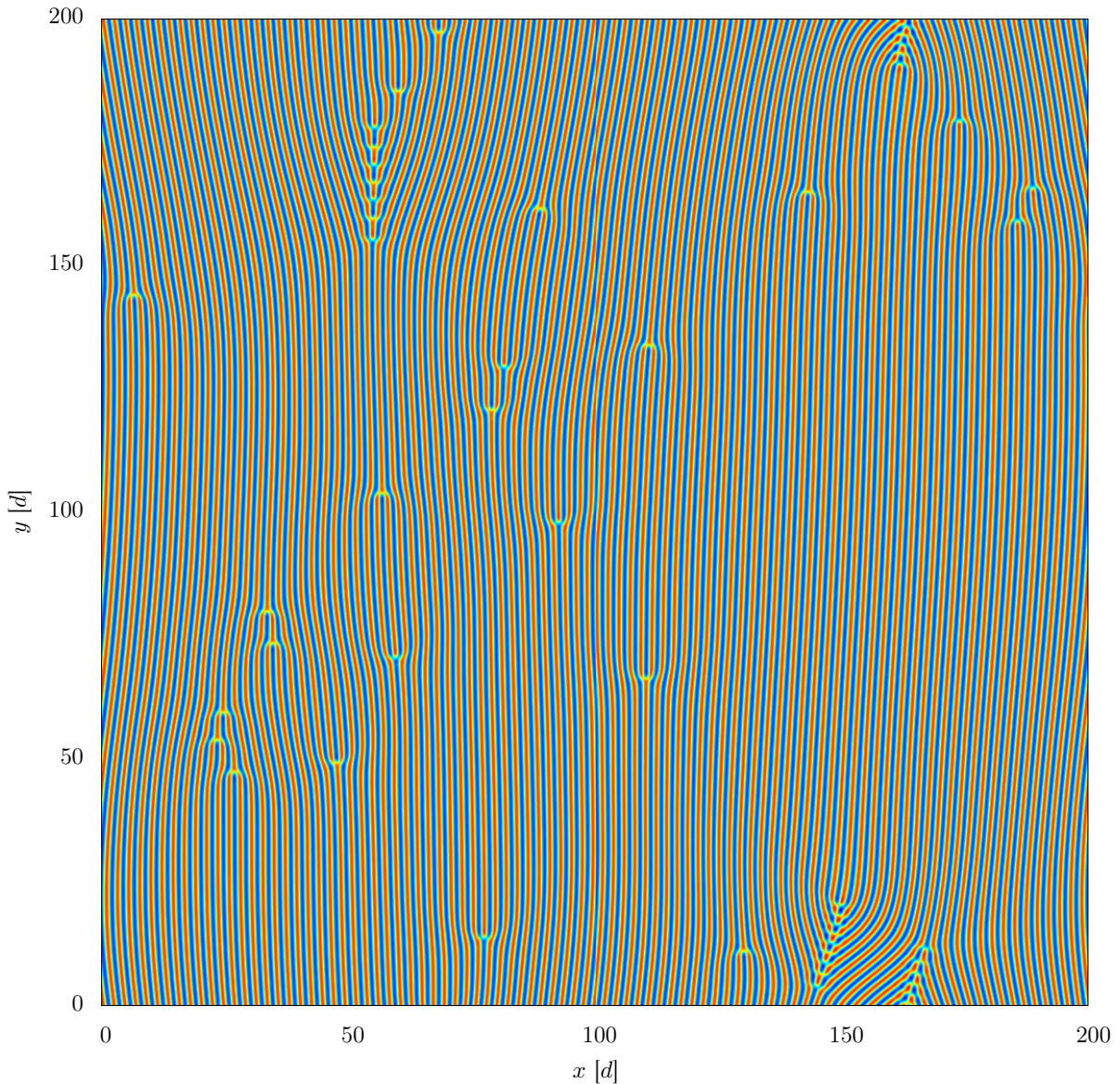


Figure 4.1.: Midplane temperature in a periodic system of aspect ratio  $\Gamma = 100$ , at  $\varepsilon = 0.2$ ,  $Pr = 1$ . We observe a mean flow in the negative  $y$  direction, and slow climbing of dislocations.

At  $\varepsilon = 0.4$ , straight rolls and spiral defects seem to coexist in the same system. While the overall pattern is generally oriented in one direction, patches of ISR are separated by regions with many defects. The defect-rich regions generally have a convex shape, often lense-shaped when embedded into an area of straight rolls. New defects get generated in the high-curvature and defect-rich regions, especially in the form of zig-zagging dislocation lines. However, the total defect density appears to remain constant, as dislocation lines meet and annihilate each other. The wave number is slightly lower than at  $\varepsilon = 0.2$ , and both its variation and the roll curvature even in the large patch of straight rolls is much larger. Regions of high curvature have a low wave number and vice versa. The correlation length of the pattern is on the same length scale as the system size, so that a system of infinite extent could still have different characteristics.

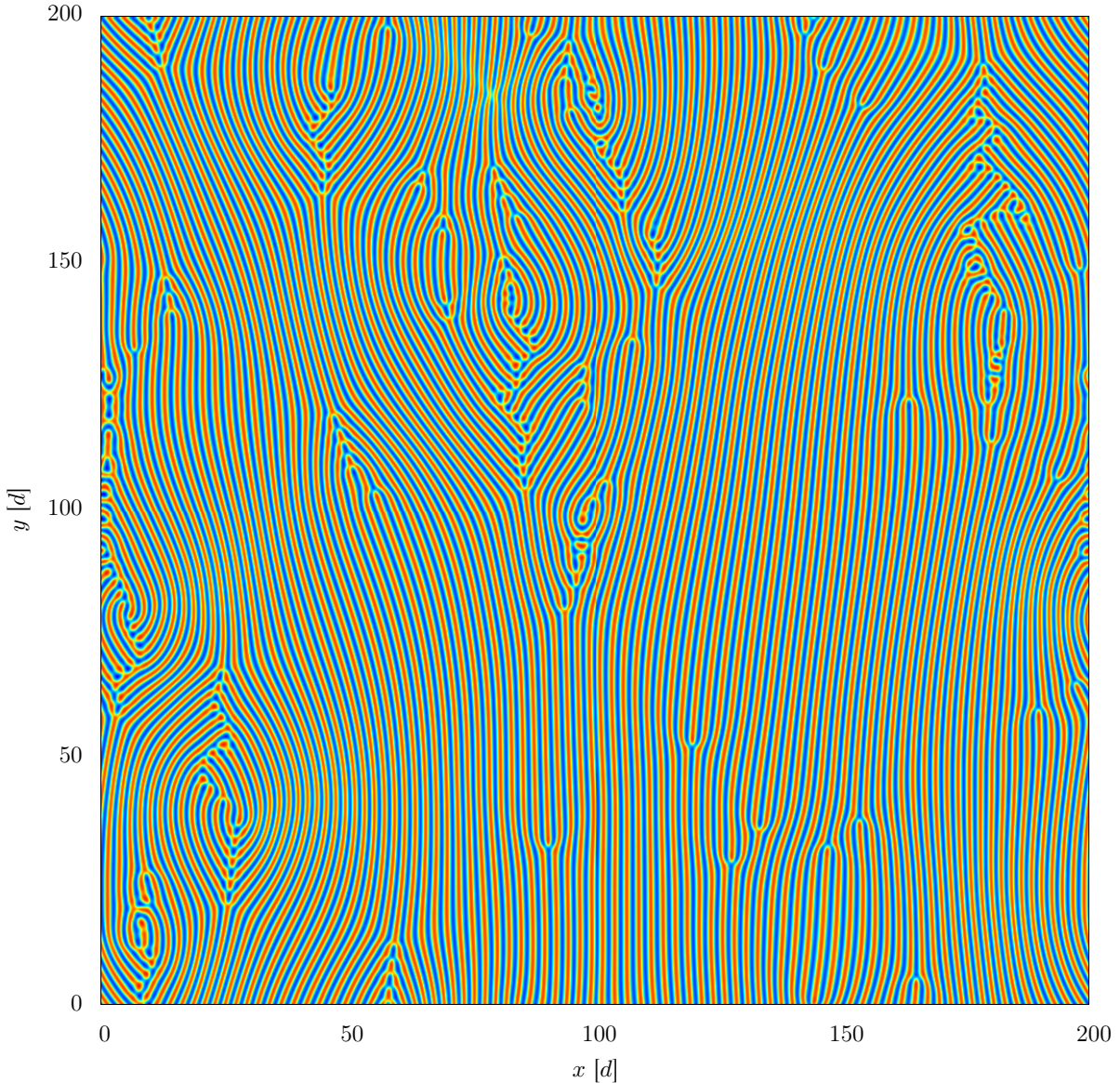


Figure 4.2.: Midplane temperature in a periodic system of aspect ratio  $\Gamma = 100$ , at  $\varepsilon = 0.4$ ,  $Pr = 1$ . Defects get generated in the high-curvature regions and annihilate when dislocation lines meet.

#### 4. Particle Transport in Spiral Defect Chaos

The pattern at  $\varepsilon = 0.5$  shows Spiral Defect Chaos, with the orientation of the straight roll patches in all the different directions and spirals being present in the system at all times. The size of the straight roll patches is on the order of 10 rolls. We commonly observe grain boundaries where the rolls are oriented perpendicular to each other, the grain boundary running parallel to the roll direction on one side. In this setting, new rolls nucleate parallel to the boundary, extending the size of the boundary-oriented region and decreasing the region with rolls perpendicular to the boundary. This allows convex regions around a dislocation-rich center to quickly grow outward. However, fronts of other orientation can just as well proceed into these curved patches. Unlike at  $\varepsilon = 0.4$ , we observe dislocation triangles, where straight roll patches of different orientations do not end in a zig-zag dislocation line, but the rolls are bent on one side to point in the same direction while they connect to each other on the other side of the triangle. The roll curvature is much larger at this Rayleigh number.

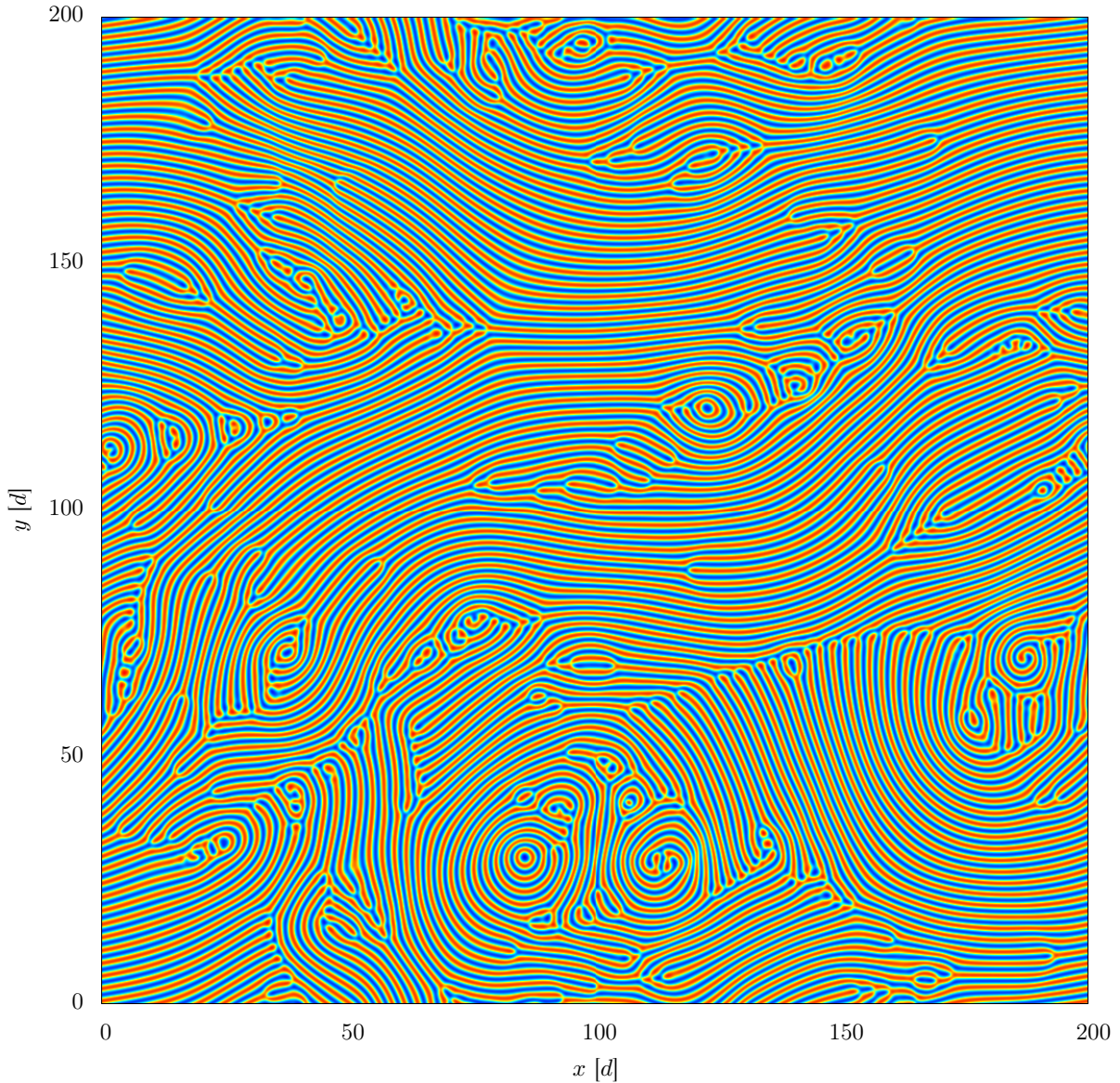


Figure 4.3.: Midplane temperature in a periodic system of aspect ratio  $\Gamma = 100$ , at  $\varepsilon = 0.5$ ,  $Pr = 1$ .

#### 4.1. Onset of SDC in Large Systems

Going to  $\varepsilon = 0.6$  shows even smaller roll patches, which measure on the order of 5 rolls across. Dislocation-rich areas fill most of the system, and many cross roll and skewed varicose instabilities can be observed in the system. The dynamics is very fast, such that large spirals are not common. Fronts that reorient patches of straight rolls still play a major part in the dynamics, but since the straight roll patches are smaller, the influence of the cross-roll instability is much stronger in changing the pattern.

We must note that for all simulations shown here, the simulation code suffered from the error discussed in Appendix A.3 for the first  $50000 \tau_v$  of the initialization time, and was continued with the correct simulation scheme for another  $10000 \tau_v$  after that. Since no significant effect of the error could be found, and the defect dynamics had a much faster time scale than  $10000 \tau_v$  for  $\varepsilon \geq 0.4$ , we believe that the images represent a typical system state. Still, we chose not to show system states between  $\varepsilon = 0.2$  and  $\varepsilon = 0.4$ , where patterns would change on this large time scale.

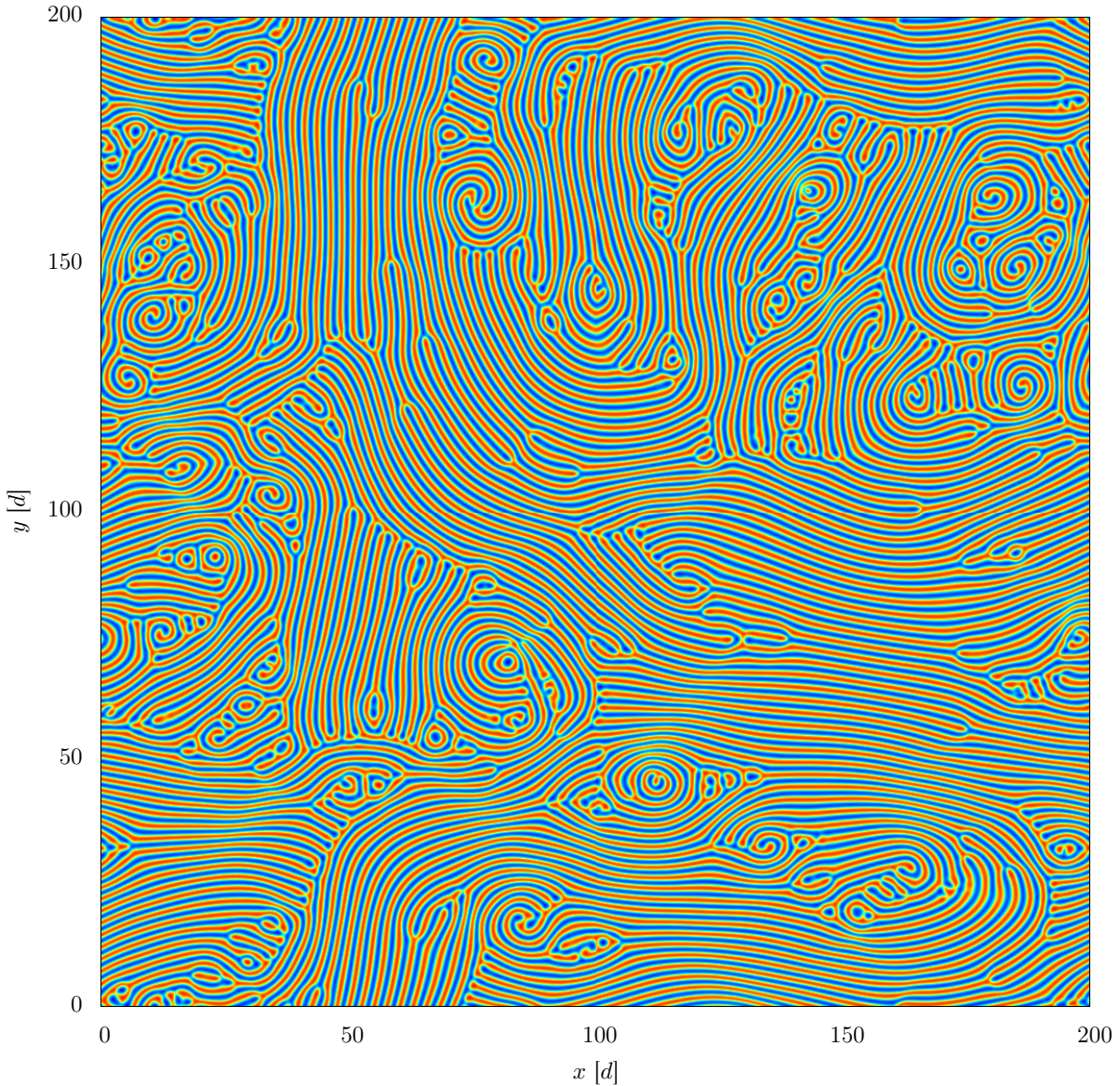


Figure 4.4.: Midplane temperature in a periodic system of aspect ratio  $\Gamma = 100$ , at  $\varepsilon = 0.6$ ,  $Pr = 1$ .

## 4.2. Particle Transport in Stationary Patterns

The roll patterns in the Bénard system can be assembled from simple primitives, namely spirals, straight rolls, and defects in between them. We investigate, from a Eulerian perspective, how diffusing particles are transported by these patterns. Figures on the following pages show the midplane temperature of the systems at chosen parameter values (note that for each image, only part of the simulation domain is shown). Unless noted otherwise, the system was simulated for an initialization time of  $5 \tau_v$  with an initial perturbation in the temperature field, then the flow was held stationary, and particles with an initial Gaussian distribution with  $\sigma^2 = 0.375$  were introduced at the specified location.

### 4.2.1. Ideal Straight Rolls

Ideal Straight Rolls (ISR) span the whole Bénard cell between the linear instability at  $Ra_c = 1708$  and the aspect ratio dependent onset of SDC at a higher Rayleigh number. Even then, the pattern is made of convection rolls, and patches of many nearly parallel rolls still exist in the system. While a top view on the midplane temperature (Fig. 4.5a) provides only few noteworthy insights, looking at the temperature and velocity fields of  $y$ -oriented rolls in a  $x$ - $z$ -view (Fig. 4.5b) reveals much of the underlying structure of the convection rolls. The convective motion stretches the interface between hot and cold fluid and increases the temperature gradient, which enhances the heat transport. Close to onset, fluid motion will lead to just a small wiggle in the mean-temperature surface (green in the plot), but with increased thermal forcing, the plumes of hot and cold fluid will be more and more pronounced, driven by faster and faster fluid motion.

The transport of diffusing tracer particles in the Ideal Straight Roll pattern has been extensively

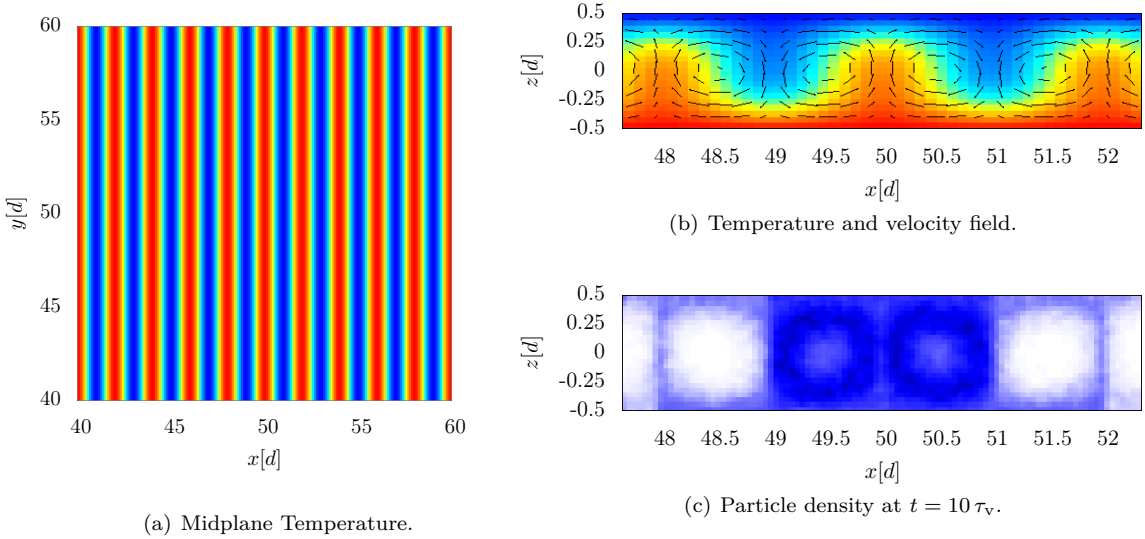


Figure 4.5.: (a): ISR pattern at  $\Gamma = 50$ ,  $\varepsilon = 0.55$ ,  $Pr = 1$ . (b): Side view on the temperature and velocity distribution of a convection roll. (c): Density distribution of diffusive particles shortly after injection.

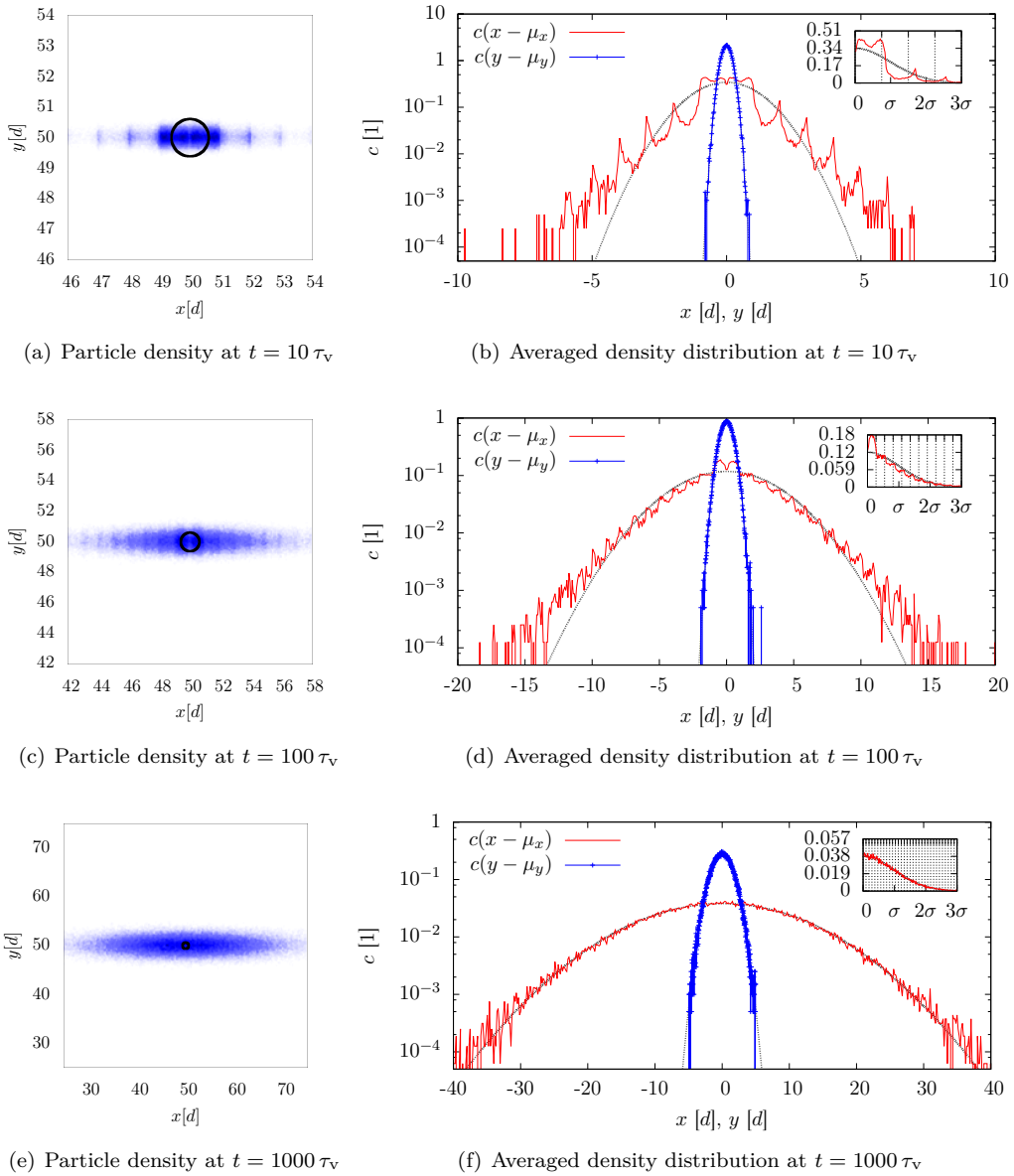


Figure 4.6.: Particle transport in a system of aspect ratio  $\Gamma = 50$  at  $\varepsilon = 0.55$ ,  $Pr = 1$ . Particle distribution of  $10^5$  particles of  $\mathcal{L} = 10^{-3}$  that were started at  $t = 0$  at location  $\langle \vec{x} \rangle = (50, 50, 0)^T$  with  $\sigma^2 = 0.375$ , for different times  $t$ . (a), (c), (e): Particle density in a top view on a region within the simulation domain. The black circle marks the initial position of the particles, its radius being their standard deviation  $\sigma$ . (b), (d), (f): Profile of the particle concentration along the  $x$ -/ $y$ -axis of the ISR system (Fig. 4.5), relative to the mean  $\mu$ . The dotted lines show a Gaussian distribution with equal mean and variance. The inset shows the data for  $c(x - \mu_x)$  without log-scale, the spacing between the dotted grid lines is one length unit  $d$  (corresponding to the height of the cell).

#### 4. Particle Transport in Spiral Defect Chaos

studied by Solomon *et al.*[28]. The roll structure enhances diffusion in a regular way, such that on a large scale and neglecting the structures within each convection roll, the particle density has a Gaussian profile. Looking at the temporal evolution of the concentration profile with time (Fig. 4.6), the transition towards the large-scale Gaussian profile can be observed. Since the fluid motion for ISR is purely in one horizontal direction, the  $x$ -direction in our case, particle motion in the  $y$ -direction happens purely by diffusion. In our axis-aligned ISR system, we define the concentration profile  $c(x)$  as

$$c(x) := \int_{\Omega_y} \int_{\Omega_z} c(x, y, z) dy dz, \quad (4.2)$$

where  $c(x, y, z)$  is the particle concentration, defined as the fraction of all particles that can be found within a small volume around  $(x, y, z)$ .  $c(y)$  is defined accordingly.

For small times far below the vortex turnover time, diffusion of the single particles dominates the transport and the concentration profile is Gaussian (not shown in the figures). On the vortex turnover time scale ( $t \sim 1 \tau_v$ ), the profile deviates from a Gaussian in that the concentration is almost constant within one convection roll, with a steep gradient between adjacent rolls (see also Fig. 4.5d) and an increased density in the distribution tails. For very long times ( $t \sim 10^3 \tau_v$ ), the tails approach the Gaussian profile again. This behavior reflects the advective motion, which enhances the diffusion at intermediate time scales, but for long times acts as a diffusion process itself due to its circulating nature.

##### 4.2.2. Straight Rolls with Imposed Mean Flow

Large scale properties of the convective dynamics are influenced by the mean flow[16], which we define as

$$\bar{u}(x, y) := \int_{\Omega_z} \vec{u}(x, y, z) dz. \quad (4.3)$$

In a roll pattern with curvature, a mean flow perpendicular to the rolls will emerge. Since a mean flow between two plates will generally assume a Poiseuille-profile that is strongest in the center between the plates, such a mean flow could strongly enhance diffusion through the separatrix between convection rolls. We investigate this setting by initializing a system with ISR as in

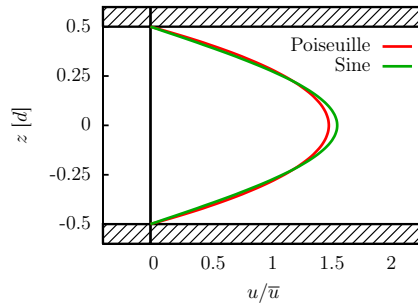


Figure 4.7.: Poiseuille-type parabolic velocity profile, and sine profile  $S_1(z)$  that we force at  $N_z = 2$ . The sine profile has a larger maximum velocity at the midplane and a less steep gradient at the boundaries.

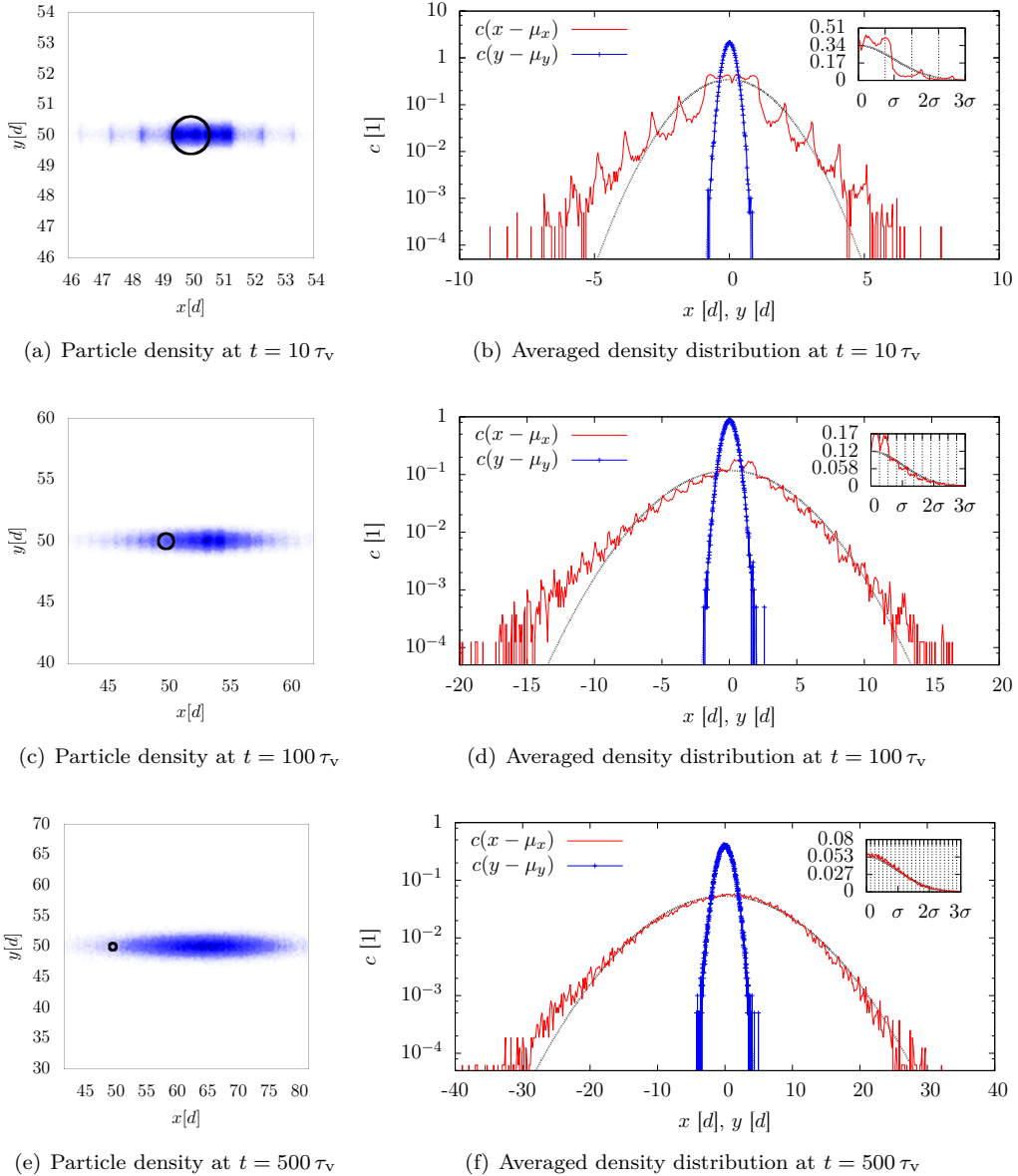


Figure 4.8.: Particle transport in a system of aspect ratio  $\Gamma = 50$  at  $\varepsilon = 0.55$ ,  $Pr = 1$  with a mean flow of  $\langle F \rangle_z = 0.042 \kappa/d$ . Particle distribution of  $10^5$  particles of  $\mathcal{L} = 10^{-3}$  that were started at  $t = 0$  at location  $\langle \vec{x} \rangle = (50, 50, 0)^T$  with  $\sigma^2 = 0.375$ , for different times  $t$ . (a), (c), (e): Particle density in a top view on a region within the simulation domain. The black circle marks the initial position of the particles, its radius being their standard deviation  $\sigma$ . (b), (d), (f): Profile of the particle concentration along the  $x$ -/ $y$ -axis of the ISR system (Fig. 4.5), relative to the mean  $\mu$ . The dotted lines show a Gaussian distribution with equal mean and variance. The inset shows the data for  $c(x - \mu_x)$  without log-scale, the spacing between the dotted grid lines is one length unit  $d$  (corresponding to the height of the cell).

#### 4. Particle Transport in Spiral Defect Chaos

Section 4.2.2, but impose a constant global mean flow  $\langle F \rangle_z$  in the positive  $x$ -direction. Figure 4.8 shows the resulting density profile.

We observe that the diffusion is actually weaker than before, and the downwind tail of the distribution is much more enhanced than the upwind tail. From Figure 4.8d, we see that the convection roll pair that initially carried the particles (with the maximum particle density) is moving faster than the mean of the distribution. We attribute this finding to effects similar to Taylor dispersion[29] in pipe flow, where diffusion towards the boundaries leads to slower transport in the parabolic mean flow profile. But even with this effect, it remains surprising that the addition of an advection mechanism, which is inhomogeneous in the  $z$ -direction, does not appear to increase the width of the final particle distribution (Fig. 4.8f) compared to convection without mean flow.

#### 4.2.3. Giant Spiral

The large spiral is a good example for the competition between two wavenumber selection mechanisms [16, 22]: In dynamic equilibrium, the spiral core in the center prefers a higher wave number and will rotate such as to increase the wave number, while the dislocation next to the side walls of a cylindrical system will move around the spiral center and decrease the wave number. A mean flow is suspected to transport mass from the spiral center to the dislocation.

Figure 4.9 shows such a spiral, with parameters inspired by values from Plapp[21]. The pattern consists of a pair of counter-rotating thermal convection rolls that start from the spiral core and form a one-armed outward spiral. The convection roll pair is annihilated at the dislocation. Beyond the dislocation, convection rolls form circles. We created an initial pattern by perturbing the initial

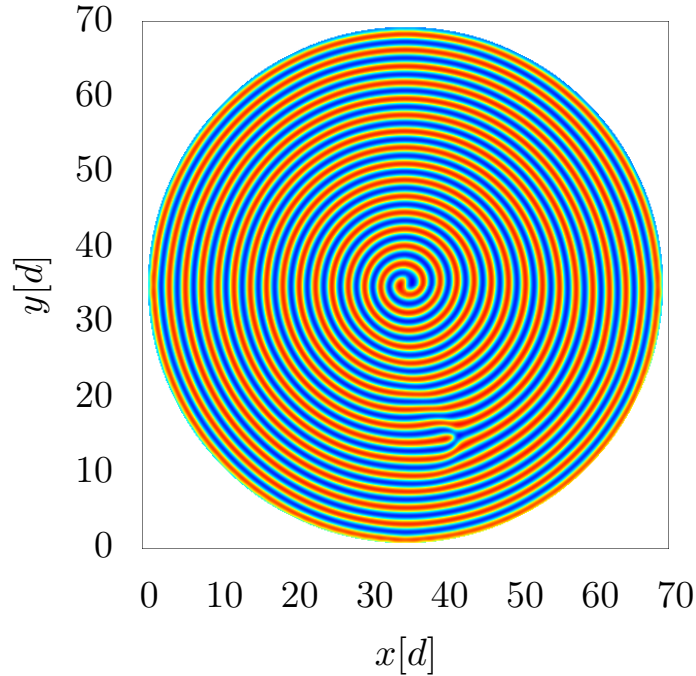


Figure 4.9.: Particle transport in a giant spiral of aspect ratio  $\Gamma = 35$  at  $\varepsilon = 0.6$ ,  $Pr = 1$ , with a circular fixed boundary. Midplane temperature of the system.

#### 4.2. Particle Transport in Stationary Patterns

temperature field according to the function

$$T_0(\vec{x}) = a_0 \cdot \cos \left( q \cdot \sqrt{(x - x_0)^2 + (y - y_0)^2} - \arctan\left(\frac{y - y_0}{x - x_0}\right) + \arctan\left(\frac{y - y_1}{x - x_1}\right) \right). \quad (4.4)$$

The initial amplitude is  $a_0 \ll 1$ , the wave number is  $q \approx 2.8 d^{-1}$ , the spiral core is at  $(x_0, y_0) = (\frac{1}{2}L, \frac{1}{2}L)$ , and an outer defect is generated at  $(x_1, y_1) = (\frac{4}{5}L, \frac{1}{2}L)$ , which lies at 60 % of the distance from the core to the boundary. To avoid nucleation of defects at the side boundary of the fluid

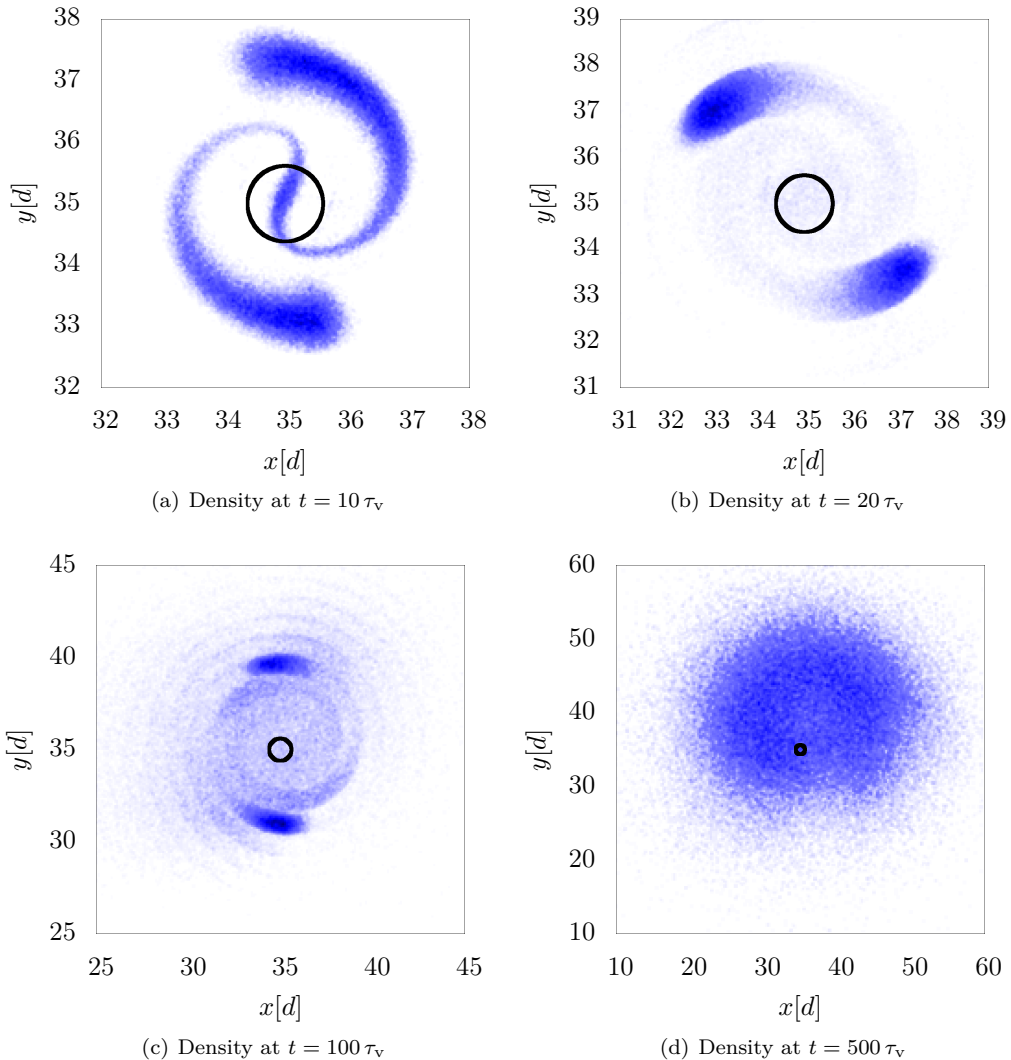


Figure 4.10.: Particle transport in a giant spiral of aspect ratio  $\Gamma = 35$  at  $\varepsilon = 0.6$ ,  $Pr = 1$ , with a circular fixed boundary. The wave number is  $q \approx 2.8 d^{-1}$ . The images show only parts of the simulation domain. Particle distribution of  $10^5$  particles of  $\mathcal{L} = 10^{-3}$  that were started at  $t = 0$  at location  $\langle \vec{x} \rangle = (35, 35, 21, 0)^T$  with  $\sigma^2 = 0.375$ , for different times  $t$ . The outer 4 convection rolls of the system were artificially kept time independent, to stop defects from the simulation domain boundary from migrating into the system.

#### 4. Particle Transport in Spiral Defect Chaos

domain, we kept the flow field of the outer 4 convection rolls constant after a short initialization phase. The defect and spiral core move around the center in the clockwise direction and with a period of  $T \approx 240 \tau_v$ .

Several interesting phenomena can be observed in this setting. For once, the initial area of high particle concentration splits up into two parts that migrate outward along the spiral arms (Fig. 4.10a). This behavior suggests a counter clockwise advective mean flow along the spiral arms. Motion across the separatrices between adjacent convection rolls is so much weaker than mixing within each roll that the rolls act as tubes that transport the tracer particles outward along the spiral arms. Within these transport tubes, the particle density dynamics is similar to Taylor dispersion[17]. As the defect moves around the center, a systematic mean flow from the core to the outer defect is not clearly visible in the tracer motion. However, we notice that the spiral core drifts off-center towards the positive  $y$ -direction for long times, such that the wave number increases on that side of the defect. For  $t > 500$ , we observed the formation of additional defects in this region. The particle transport shows a large-scale mean flow in this direction, which strongly shifts the center of mass of the particles and apparently moves the spiral core along as well.

##### 4.2.4. Dislocation

Figure 4.12 shows one dislocation of a dislocation pair at  $q = \pi/d$ . Particles introduced into the system show a mean motion in the direction of the higher wave number (the negative  $y$  direction in figures 4.12a-d). The particles proceed in a front that is spread across several convection rolls, and move back in the positive  $y$  direction further away from the symmetry axis of the dislocation. Despite this backward motion, particle density stays low in a conical area in the region of lower wave number, and the high-density region assumes an elliptical shape which resembles that of the Gaussian distribution for ISR (Fig. 4.6f).

We assume that the overall particle distribution is caused by two large, counter-rotating vortices in the horizontal plane (Fig. 4.11). Since the wave number of the system is already higher than the preferred one, the system pushes the dislocation in the negative  $y$  direction to reduce its wave number. If this process induces a mean flow along the dislocation, it will have to be compensated

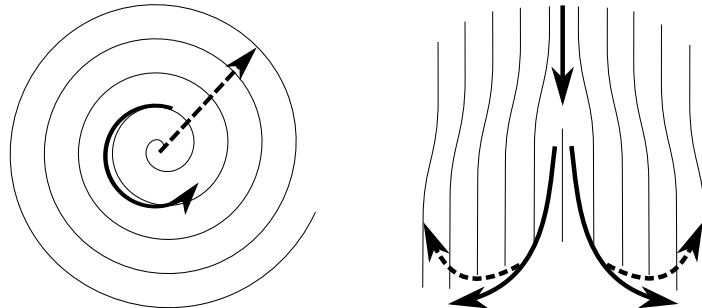


Figure 4.11.: Left: Mean flow of the giant spiral, and mean flow that moves the spiral core. Note that the spiral pattern itself was rotating in the opposite direction of the rotating mean flow. Right: Particle transport pattern near a dislocation in straight rolls.

## 4.2. Particle Transport in Stationary Patterns

by a mean fluid motion to positive  $y$  in the rest of the system. This flow pattern pulls the particle blob along, until it reaches a region where the influence of the dislocation is small and the pattern is that of normal ISR. Since the mean flow motion is inhomogeneous along the vertical axis, not all particles will be moved equally (see also Section 4.2.2), and particles remain in the region between the dislocation and the particle blob. From there, they move to positive  $y$  along the convection tubes.

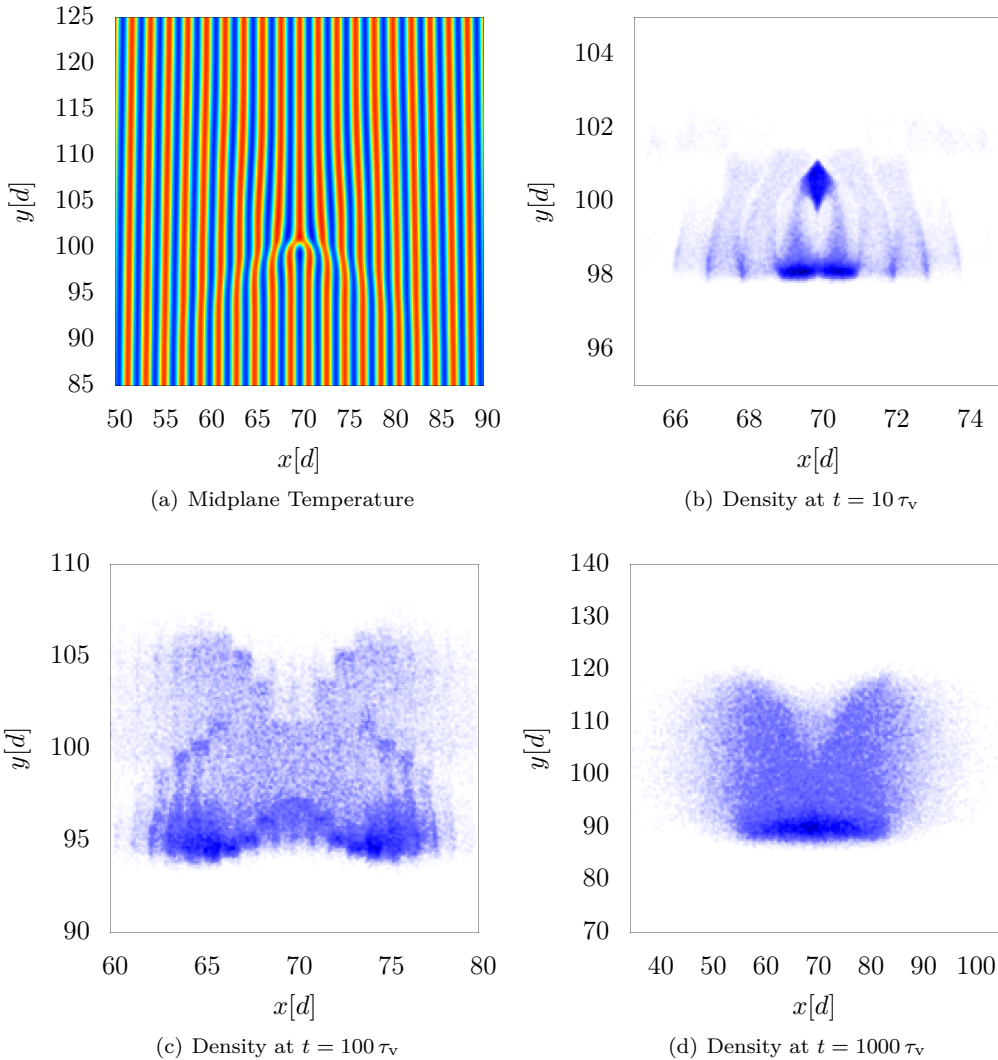


Figure 4.12.: Particle transport around a dislocation at aspect ratio  $\Gamma = 70$  at  $\varepsilon = 0.55$ ,  $Pr = 1$ . The images show only parts of the simulation domain. (a): Midplane temperature of the system. (b), (c), (d): Particle distribution of  $10^5$  particles of  $\mathcal{L} = 10^{-3}$  that were started at  $t = 0$  at location  $\langle \vec{x} \rangle = (70, 101, 0)^T$  with  $\sigma^2 = 0.375$ , for different times  $t$ .

### 4.2.5. Dislocation Lines

When simulating a large aspect ratio cell close to SDC onset ( $\varepsilon = 0.25$ ), we found a quasi-periodic pattern as depicted in Fig. 4.14. Since this simulation suffered from the error discussed in Appendix A.3, we cannot claim that this pattern is representative for Rayleigh-Bénard convection at the given parameter values. In a system of straight rolls, a dislocation line starts, similar to a grain boundary in solid state physics. While the starting point of the dislocation line drifts only slowly, the lower ends oscillate, driven by cross rolls. Introducing particles at the starting point reveals the transport behavior: Like in the ISR case, there is an amplification of the diffusivity perpendicular to the rolls. In addition, however, a strong transport occurs along the dislocation.

The observed pattern and particle transport reveal many properties of Rayleigh-Bénard convection: Due to the roll curvature at both sides of the dislocation, we expect a mean flow that enhances transport in these two directions. The dislocation line shows the competition between domains of different straight roll orientation, which we already discussed in Section 4.1 and see in Figure 4.13: The boundary between regions of different roll orientation is parallel to the rolls on one side and moves towards the other side. This happens when the angle between the roll directions is near  $90^\circ$ , at lower angles, the configuration seems more stable and the boundary is symmetric between the domains.

The square system is periodic with an edge length of  $200d$ , and the domains of different roll orientation meet again at a dislocation line with the same structure that points in the other direction. Despite the fast dynamics of the dislocation line, no new defects get generated, and towards the bottom of the dislocation line, the rolls curve back to form a parallel pattern. Since the boundaries always move perpendicular to rolls that end, the number of defects is conserved.

At  $\varepsilon = 0.25$ , the long-range order of the pattern spans the whole system. For earlier times, the same simulation featured one giant, multi-armed spiral. From the time that the simulation was run, it remains unclear whether the system will at some point merge the two dislocation lines and move towards an ordered state with only few defects.

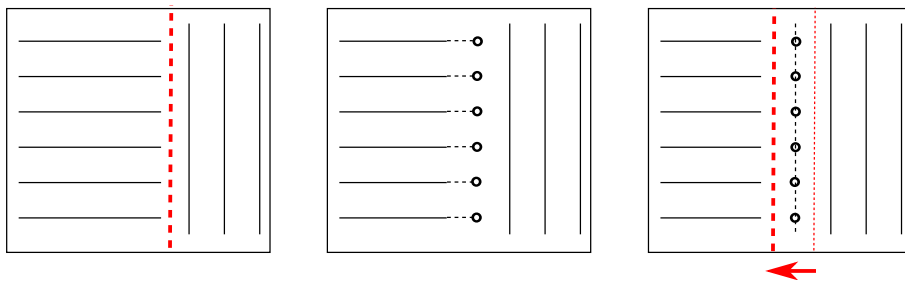


Figure 4.13.: At straight roll domain boundaries with angles close to  $90^\circ$ , the boundary (red dashed line) orients parallel to the rolls in one domain (black lines). This induces a cross roll instability in the other domain, and the boundary moves. At  $Pr = 1$ , this behavior has a major impact on the pattern dynamics in the range  $0.2 < \varepsilon < 0.8$ , where systems have large ISR domains of different orientations.

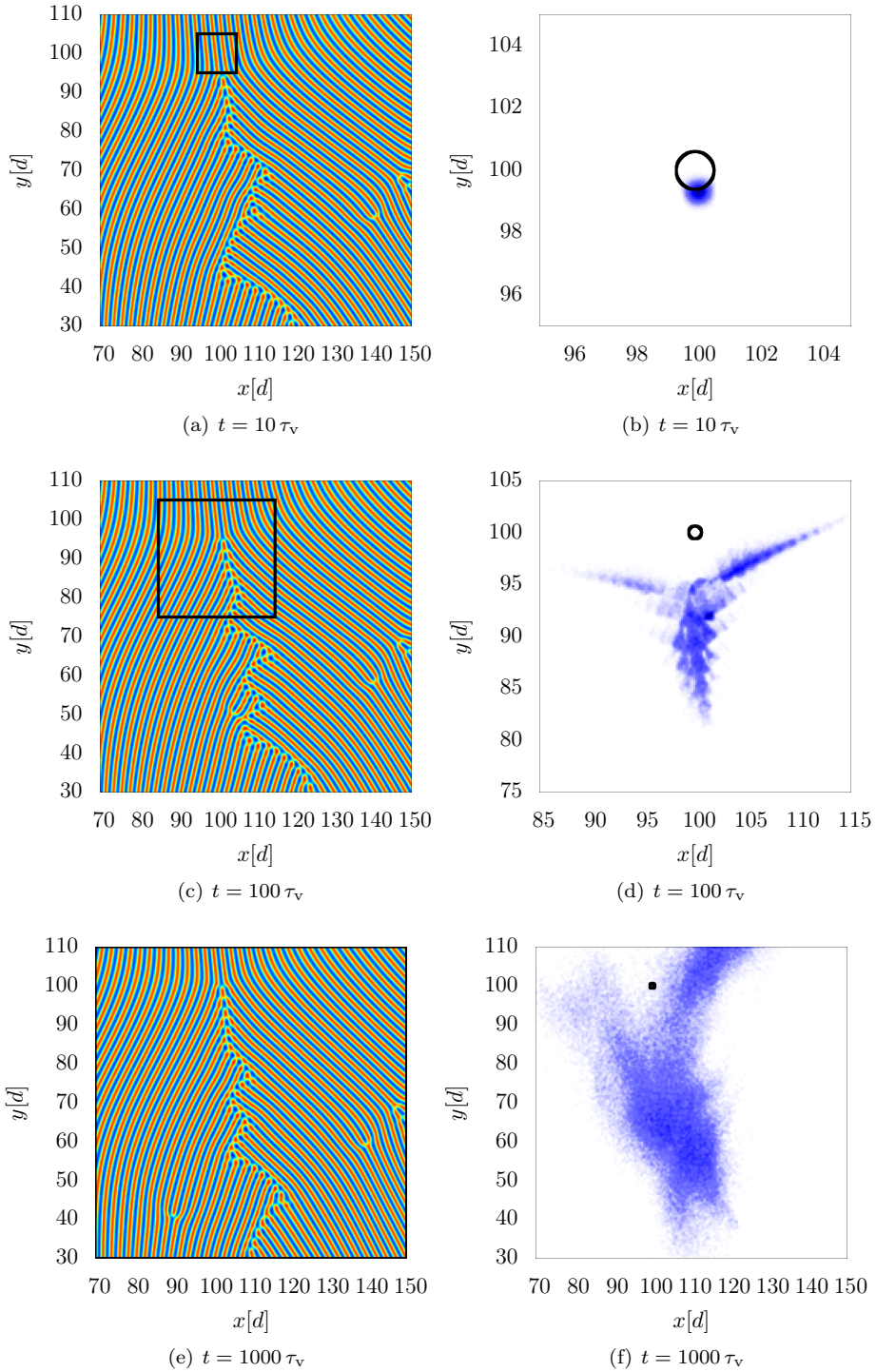


Figure 4.14.: Pattern and particle transport in a large system of aspect ratio  $\Gamma = 100$  at  $\varepsilon = 0.25$ ,  $Pr = 1$ . The images show only parts of the simulation domain. (a),(c),(e): Midplane temperature. (b),(d),(f): Particle distribution of  $10^3$  particles of  $\mathcal{L} = 10^{-3}$  that were started at  $t = 0$  at location  $\langle \vec{x} \rangle = (100, 100, 0)^T$  with  $\sigma_{xy}^2 = 0.375$ , for different times  $t$ .

### 4.3. Diffusive Transport of Passive Scalar

To investigate the transport properties of time-dependent Rayleigh-Bénard convection, we first consider transport in a small fluid cell of aspect ratio  $\Gamma = 30$ . We release a fixed number of passive tracer particles at the center, and consider the second moment (variance) of the tracer distribution,

$$M_2(t) = \sigma^2(t) = \langle [x - \langle x \rangle]^2 \rangle. \quad (4.5)$$

Results in this setting, for a passive scalar fluid, have been first reported by Chiam *et al.*[11]. In our series of experiments, we first choose parameters to match their choice and compare their results to our simulations. Later, we extend the measurements to more data points and larger systems.

#### 4.3.1. Mean Square Displacement

We measure the mean square displacement  $M_2(t)$  over a set of  $N = 10^5$  particles, which we release into the Bénard system at some time  $t_0$  after an initialization period. The particles are released at the center of the system, with an initial variance of  $M_2(t_0) = \frac{3}{8} d^2$ . As the standard deviation of such distribution is smaller than 1 ( $\sigma \approx 0.61 d$ ), the majority of the particles is then contained in one or two convection rolls. Figure 4.15 shows the midplane temperature field of one realization of the flow field. Mean flow in the pattern is observed to be very small, such that the center of the distribution remains at the center of the cell.

We consider the time development of the mean square displacement at different Rayleigh numbers and particle diffusivities (Fig. 4.16), at values for which results have been reported in [11]. Three regions can be identified: For very short times below the vortex turnover time ( $t < \tau_v$ ),  $M_2$  starts off very flat, with a steep gradient at  $t \approx 0.1 \tau_v$  followed by a plateau. This regime is characterized by vertical motion in the convection rolls, which will first advect particles in one direction, but will

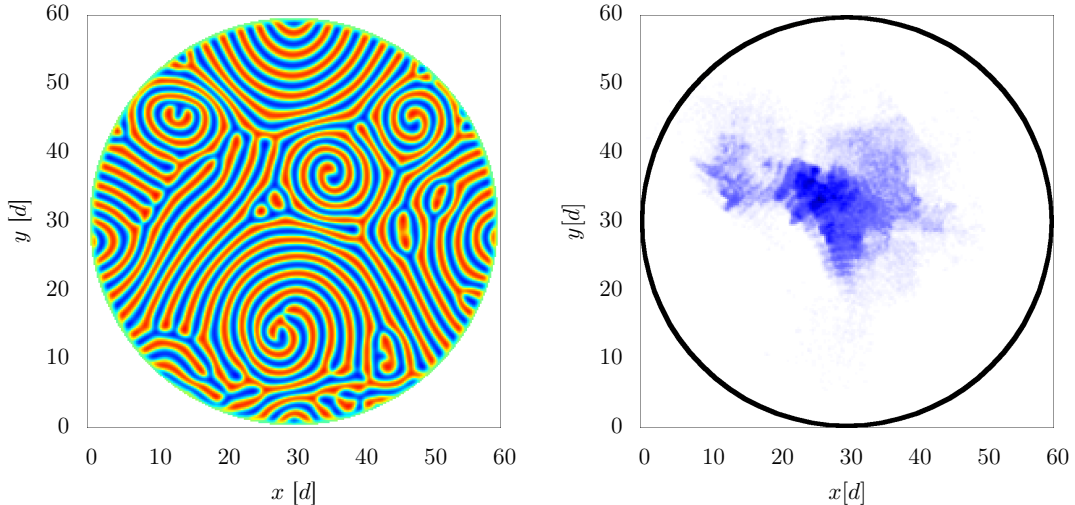


Figure 4.15.: Left: Midplane temperature for a cylindrical system of aspect ratio  $\Gamma = 30$  at  $\varepsilon = 0.8$ ,  $Pr = 1$ . Right: Particle density of  $N = 10^5$  particles with  $\mathcal{L} = 10^{-3}$  at  $t = 10^2 \tau_v$ .

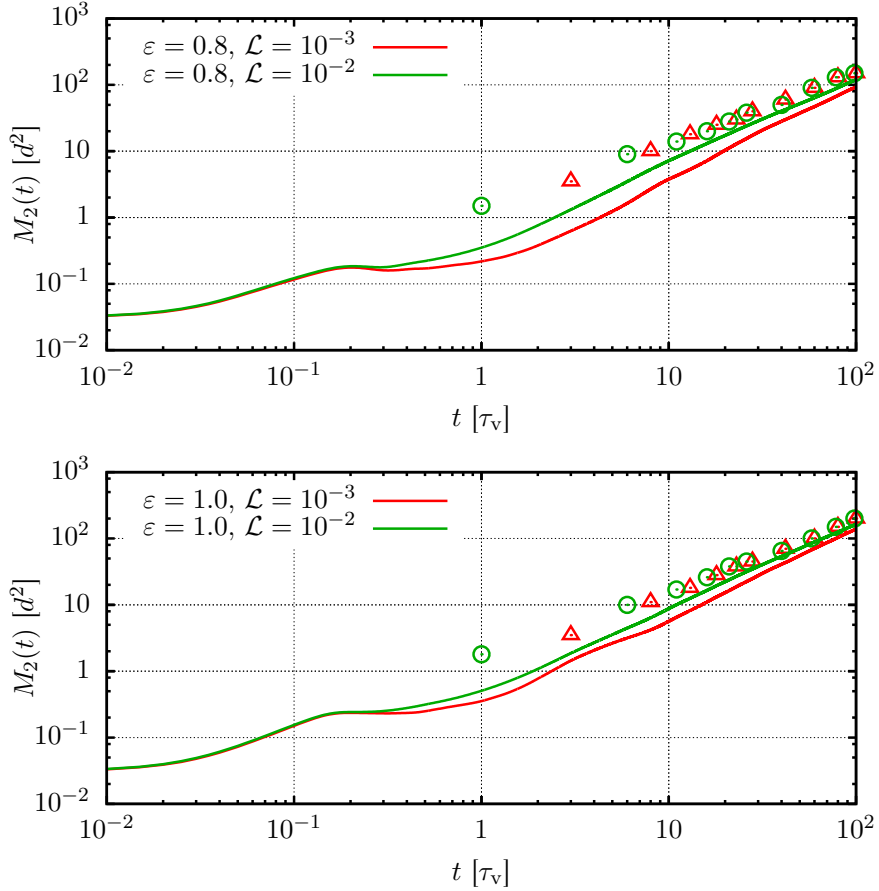


Figure 4.16.: Development of the mean-square displacement  $M_2(t)$  of the tracer particles, in a cylindrical system of aspect ratio  $\Gamma = 30$  at  $Pr = 1$  and for different  $\varepsilon$ . The lines show the average over 20 simulations with  $N = 10^5$  particles each. Circles and triangles correspond to the values in [11].

then stretch the particle cloud when it spans across more than one roll. Our focus is on the regime after this initial phase, with times in the range  $t \in [1 : 10^2] \tau_v$ , where diffusion and advection along the horizontal dimensions raise the mean square displacement above one. Over these two decades, we observe a nearly linear increase of the mean square displacement with time, which we will analyze next. For  $t > 10^2 \tau_v$ ,  $M_2$  approaches  $(L/2)^2 = 900 d^2$ , the upper bound for the second moment in the finite-size system. Here, an increasing number of particles reaches the boundaries of the simulation domain. As the side walls are implemented with the penalization technique, particles can freely diffuse through them, causing a biased statistics for these long times. We therefore ignore all results for  $M_2 > 300 d^2$ , and later give results for a large aspect ratio system of  $\Gamma = 100$  with periodic boundary conditions, which does not suffer so much from boundary effects and serves as a closer approximation to systems of infinite extent.

### 4.3.2. Effective Diffusivity

The linear regime in the variance of the particle distribution describes a normal diffusion process, with an effective diffusivity that is generally larger than that of the individual particles due to an enhancement by the advective motion. Following Chiam *et al.*[11], we thus define an effective Lewis number  $\mathcal{L}^*$  by

$$\mathcal{L}^* = \left\langle \frac{M_2(t)}{4t \cdot \kappa} \right\rangle, \quad (4.6)$$

based on the approximation of normal diffusive transport in a two-dimensional system (Eq. (2.45)). As the thermal diffusivity  $\kappa$  is only used to arrive at a dimensionless form of the diffusivity, we

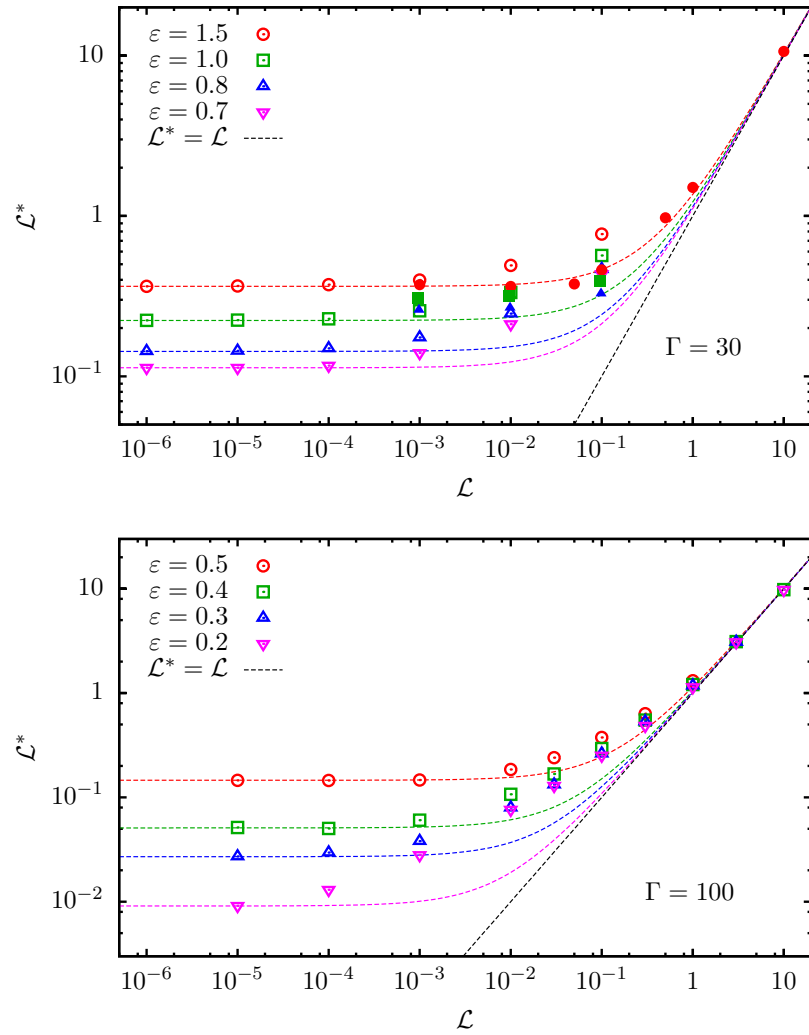


Figure 4.17.: Relation between effective diffusivity  $\mathcal{L}^*$  and particle diffusivity  $\mathcal{L}$ , at different  $\varepsilon$  and  $\Gamma$ , with  $Pr = 1$ . The system with  $\Gamma = 30$  is cylindrical, the runs at  $\Gamma = 100$  were performed in a periodic system. Filled symbols are data from [11]. The dotted lines represent relations  $\mathcal{L}^* = \mathcal{L}_0 + \mathcal{L}$ .

will refer to  $\mathcal{L}^*$  synonymously by the terms *effective Lewis number* and *effective diffusivity*. The average is performed for the range  $M_2 \in [1 : 300] d^2$ , which is the linear regime in all measurements. The effective diffusivity characterizes the joint effect of diffusion and advection that transports a particle through the system.

The relation between particle diffusivity  $\mathcal{L}$  and resulting effective diffusivity  $\mathcal{L}^*$  is shown in Figure 4.17. For small  $\mathcal{L}$ , the particle dispersion is dominated by the motion of the convecting fluid and largely independent of  $\mathcal{L}$ . There seems to be a basic diffusion mechanism inherent to the convection system that sets a base line to the effective diffusivity. At extremely high particle diffusivities ( $\mathcal{L} > 1$ , i.e. the particle diffusivity being larger than the thermal diffusivity), the effective diffusivity collapses onto the line  $\mathcal{L}^* = \mathcal{L}$ . Here, the effective diffusive motion of the particles is faster than the advection. A simple model for the observed behavior would be to express the effective  $\mathcal{L}^*$  as a sum of the ( $\varepsilon$ -dependent) base line system diffusivity  $\mathcal{L}_0$ , and the particle diffusivity  $\mathcal{L}$ :

$$\mathcal{L}^* = \mathcal{L}_0 + \mathcal{L} \quad (4.7)$$

This result would be observed if the two random processes were statistically independent (with  $\sigma^{*2} = \sigma_0^2 + \sigma^2$ ). In fact, the observed behavior is close to this basic model, but exhibits an amplification for  $\mathcal{L} \approx \mathcal{L}_0$ . With decreasing  $\varepsilon$ , the initial plateau shifts to lower and lower  $\mathcal{L}$ , indicating that the diffusivity inherent to the flow pattern is driven by the spatiotemporal dynamics of the pattern and its dislocations rather than the pure existence of convection rolls. Lewis number values of  $\mathcal{L} < 10^{-7}$  will not be considered here, such as to avoid rounding errors of our discrete floating-point accuracy.

Comparison with the values brought forward by Chiam *et al.* shows the same trend for the simulation at  $\varepsilon = 1.5$ , but a significantly larger difference between diffusion enhancements for the different  $\varepsilon$ . The reasons for this discrepancy remain unclear, but might lie in the limited vertical resolution of our simulation.

### 4.3.3. Diffusion Enhancement

The relative diffusion enhancement caused by the advective motion, which we call  $\Delta$ , can be obtained by considering the ratio between the absolute increase in Lewis number due to advection, and the original Lewis number:

$$\Delta := \frac{\mathcal{L}^* - \mathcal{L}}{\mathcal{L}}. \quad (4.8)$$

The relative influence of diffusion and advection on mass transport can be described by the dimensionless Péclet number, which is defined as

$$\mathcal{P} := \frac{d \cdot U}{\mathcal{D}} = \frac{d}{\kappa} \cdot \frac{U}{\mathcal{L}}. \quad (4.9)$$

We have chosen the characteristic length scale as the system height  $d$ , and the characteristic velocity  $U$  to be the average absolute velocity of the fluid flow inside the Bénard system, which we

#### 4. Particle Transport in Spiral Defect Chaos

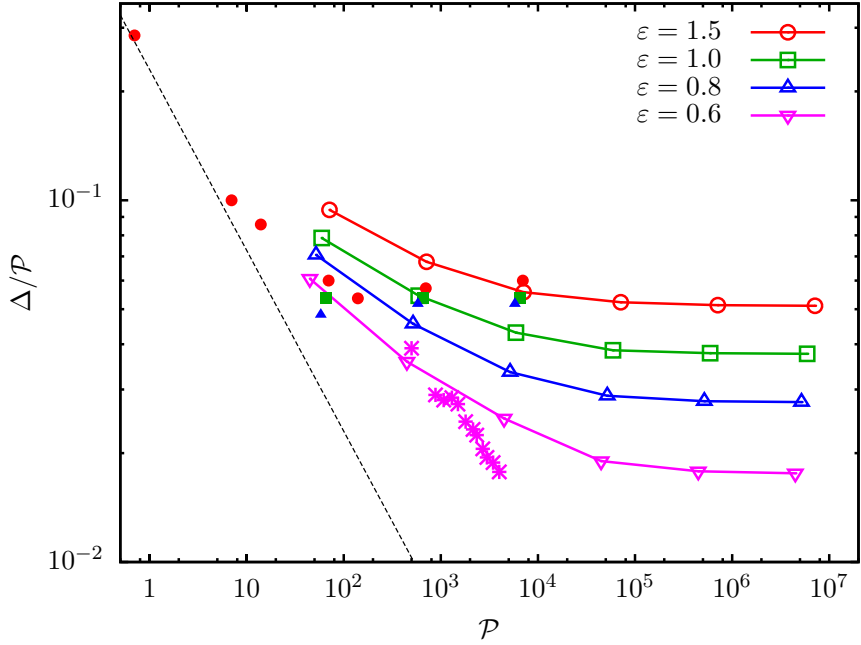


Figure 4.18.: Diffusion enhancement relative to the Péclet number, in a cylindrical system at  $\Gamma = 30$ ,  $Pr = 1$ , for different  $\varepsilon$ . Filled symbols are simulation results from [11], stars are measurements from [28] (with fast rotating straight rolls at  $\varepsilon = 4.5$ ). The dashed line is  $\Delta \propto P^{1/2}$ . Note that  $\Delta/P \propto (\mathcal{L}^* - \mathcal{L})$  and  $P \propto \mathcal{L}^{-1}$ .

calculate by averaging over the fluid volume  $\Omega^f$ :

$$U := \langle |\vec{u}| \rangle = \frac{1}{|\Omega^f|} \int_{\Omega^f} |\vec{u}(\vec{x})| d\vec{x} \quad (4.10)$$

Since the term  $\frac{d}{\kappa}$  is the inverse of our selected velocity scale, it will be omitted when we consider  $U$  in dimensionless coordinates. From their findings, Chiam *et al.* suggest that

$$\Delta \propto P. \quad (4.11)$$

We confirm this hypothesis for large  $P$  by plotting the quantity  $\Delta/P = \frac{\mathcal{L}^* - \mathcal{L}}{U}$  in Figure 4.18. Again, we observe the Rayleigh number dependence of the diffusion process to be much more pronounced than Chiam *et al.* report. For  $P < 10$  (not shown in Fig. 4.18), we observed a drop in the diffusion enhancement, which we cannot explain physically. It is likely an artifact of our simulation scheme: As discussed in Section 3.2, we assume that over the time step  $dt$  of our simulation the position increment due to diffusion is much smaller than the scale on which the velocity field changes. However, for  $\mathcal{L} \geq 1$ , the jumps get increasingly large even for small time steps like  $dt = 10^{-3}$ , where

$$\sigma = \sqrt{2 \mathcal{L} \cdot dt} \geq \sqrt{2 \cdot 10^{-3}} \approx 0.04.$$

A significant variation in the flow pattern can be expected across 5% of the system height, especially near the vertical boundaries. Over the same time interval, advection on the velocity scale  $U = 5$  will transport a particle over a distance of  $dx = 0.005$  (in units of  $d$ ): The diffusion process hides the effects of advection. As our focus is on situations where the defect dynamics of the Spiral Defect Chaos has a major influence on the particle diffusion process, we will not concern us with this extreme case of high diffusivity, but use values for the diffusivity where the dependence of the diffusivity enhancement on  $\varepsilon$  is large. We expect our simulation technique to be most accurate for  $10^{-2} \leq \mathcal{L} \leq 10^{-7}$ , where the effect of diffusion is smaller than that of advection, but large enough to cause particle dispersion throughout the system and be orders of magnitude larger than numerical rounding and discretization errors.

In measurements with Ideal Straight Rolls at  $\varepsilon = 4.5$ , Solomon *et al.*[28] observed a scaling of

$$\mathcal{L}^* \propto \mathcal{P}^{1/2}. \quad (4.12)$$

For this ISR case, the observation matches calculations that base on a diffusion process through the separatrices between adjacent rolls. Chiam *et al.* observe the same effect in their simulations for small  $\mathcal{P}$ , when diffusion is fast relative to advection, and suspect a transition from a scaling of  $\mathcal{L}^* \propto \mathcal{P}$  to  $\mathcal{L}^* \propto \mathcal{P}^{1/2}$  when the Péclet number  $\mathcal{P}$  decreases. This type of transition is visible in our data as well. The transition point lies in the region of  $\mathcal{P} = 10^4$  at  $\varepsilon = 0.6$  and moves towards  $\mathcal{P} = 10^2$  for higher  $\varepsilon$ . We suspect that the transition in the scaling is a result of the increasing density of defects that characterize the transition from ISR to SDC: When the Péclet number is low, particle diffusivity is strong and diffusion through the separatrix between adjacent rolls will be relatively easy, regardless of the change of the convective pattern with time. For higher Péclet numbers however, particles are kept within one roll and will change rolls preferentially during the creation or annihilation of defects. In this regime, defect dynamics will be the leading cause of diffusion enhancement.

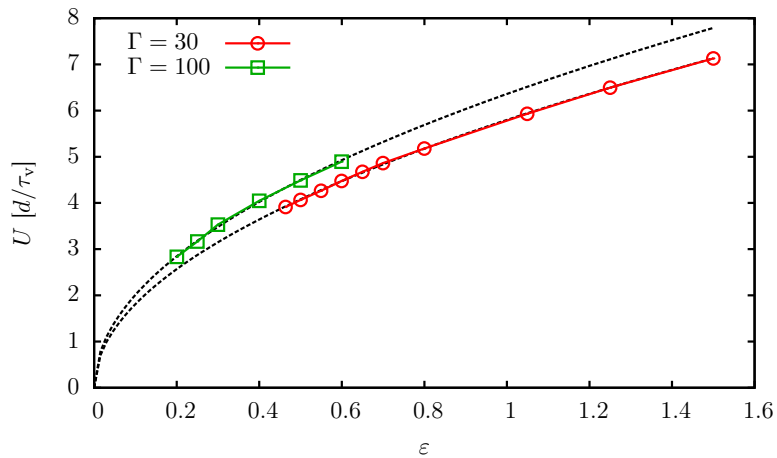


Figure 4.19.: Characteristic velocity  $U$  relative to the distance  $\varepsilon$  from RBC onset, in a cylindrical system with  $\Gamma = 30$ ,  $Pr = 1$ , and a periodic system with  $\Gamma = 100$ . The dashed black lines are  $U \propto \sqrt{\varepsilon}$ .

#### 4.3.4. Rayleigh Number Effects on Diffusion Enhancement

We now investigate how changes in the strength of thermal convection, characterized by the reduced Rayleigh number  $\varepsilon$  (see Eq. (2.22)), enhance the particle diffusion. We note that the first and foremost effect of the thermal forcing is to drive the convective motion, which leads to an advection with a characteristic mean velocity  $U$ . We observe a scaling of

$$U \propto \varepsilon^{1/2}. \quad (4.13)$$

This scaling can be observed for both the cylindrical cell with fixed boundaries at  $\Gamma = 30$ , and a periodic system of aspect ratio  $\Gamma = 100$  (Figure 4.19). The absolute value of  $U$  in the fixed-boundary system is smaller than in the periodic system, as one would expect, considering side wall friction and the larger number of defects in the pattern. Chiam *et al.* have measured the effective diffusivity for three different  $\varepsilon$ , and from that data assume a scaling of the diffusion enhancement of the form

$$\mathcal{L}^* - \mathcal{L} \propto \varepsilon^{1/2}. \quad (4.14)$$

This is consistent with their result of  $\Delta \propto \mathcal{P}$  for large  $\mathcal{P}$ :

$$\begin{aligned} \mathcal{L} \cdot \mathcal{P} &\propto \mathcal{L} \cdot \Delta \propto \varepsilon^{1/2} & [\text{with } \mathcal{P} := \frac{d}{\kappa} \cdot \frac{U}{\mathcal{L}}, \Delta := \frac{\mathcal{L}^* - \mathcal{L}}{\mathcal{L}}] \\ \Rightarrow U &\propto \varepsilon^{1/2} \end{aligned} \quad (4.15)$$

However, this behavior is only being observed for large  $\mathcal{P}$ , and Chiam *et al.* suspect a transition in the transport mechanism for smaller  $\mathcal{P}$  that leads to the  $\Delta \propto \mathcal{P}^{1/2}$  scaling of Solomon *et al.* (in ISR). By considering smaller  $\varepsilon$  at the transition from SDC to ISR, we confirm that the scaling

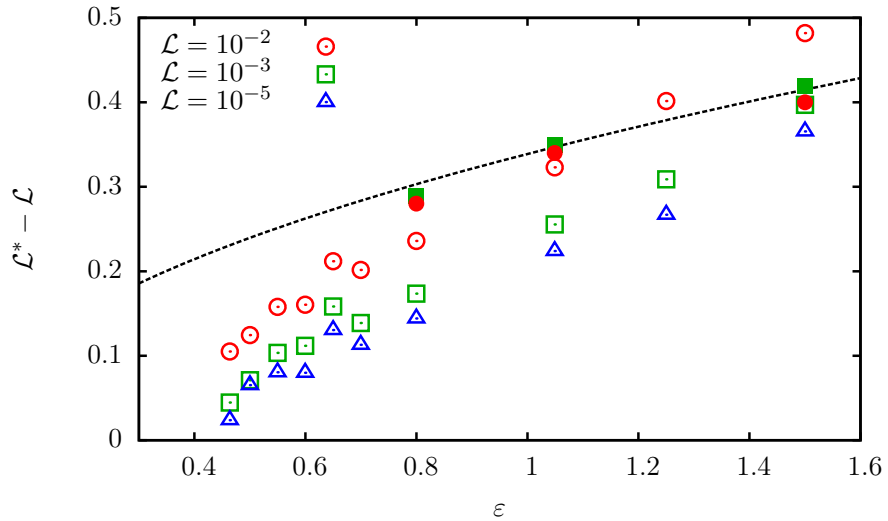


Figure 4.20.: Diffusion enhancement  $\mathcal{L}^* - \mathcal{L}$  relative to the distance  $\varepsilon$  from RBC onset, in a cylindrical system with  $\Gamma = 30$ ,  $Pr = 1$ . Filled symbols are simulation results from [11]. The black line is  $\mathcal{L}^* - \mathcal{L} \propto \sqrt{\varepsilon}$ .

does not follow the square root behavior all the way to  $\varepsilon = 0$ : Our observations at different  $\varepsilon$  qualitatively confirm the measurements for the parameter values they considered, but deviate from their fit for smaller  $\varepsilon$ . As shown in Figure 4.20, we observe only a small effective diffusivity below a transition point at  $\varepsilon \approx 0.5$ , and a steep increase afterwards. The transition point lies close to the onset of Spiral Defect Chaos, which at the aspect ratio of  $\Gamma = 30$  is expected to lie at  $\varepsilon_s \approx 0.55$  (see also [5]). We observe that the effective diffusivity varies a lot between different realizations of the flow at identical parameters (i.e. at different initial conditions or different times), as the system switches quickly between ordered and disordered states. ISR and SDC can exist at identical parameter values, but the diffusion enhancement in the SDC state is much higher than for ISR.

To arrive at more meaningful data for smaller  $\varepsilon$ , we increase the aspect ratio of our system to  $\Gamma = 100$  and use periodic boundary conditions. The results are shown in Figure 4.21. In the measurements, we observe a jump in the effective diffusivity between  $\varepsilon = 0.4$  and  $\varepsilon = 0.5$ . Since we can measure the effective diffusion without boundary effects in this larger system and the system does not switch between different states as fast, the results are more consistent between individual runs and capture more of the overall dynamics of the advection-diffusion transport. We especially observe a consistently higher effective diffusivity for particles of a higher particle diffusivity ( $\mathcal{L} = 10^{-2}$ ), which matches the observation of a transition from the  $\Delta \propto \mathcal{P}$  to the  $\Delta \propto \mathcal{P}^{1/2}$  region for high  $\mathcal{L}$  and low  $\varepsilon$  from Section 4.3.3 (Fig. 4.18).

We must note that the measurements of passive scalar diffusion are strongly influenced by the time and location that we released our tracer particles at. This becomes apparent especially if dynamics at the chosen location is not characteristic for the overall dynamics, as we observed when we entered particles right into a dislocation line (see Fig. 4.14) at  $\varepsilon = 0.25$ . It is a general problem of this type of measurement that it is sensitive to the initial conditions of the scalar inside the flow field. We will therefore in the next section (Section 4.4) consider Lagrangian statistics of particle pairs, which will likely have a better sampling of the overall dynamics of SDC.

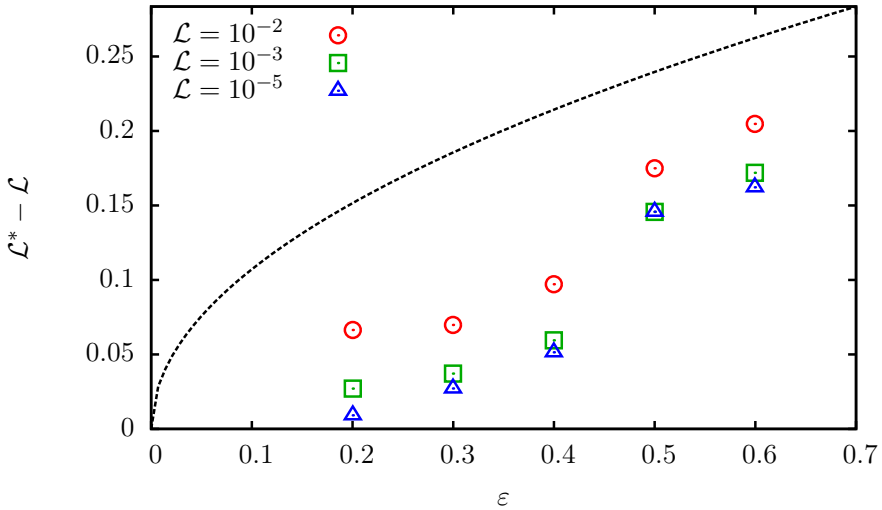


Figure 4.21.: Diffusion enhancement  $\mathcal{L}^* - \mathcal{L}$  relative to the distance  $\varepsilon$  from RBC onset, in a periodic system with  $\Gamma = 100$ ,  $Pr = 1$ . The black line is  $\mathcal{L}^* - \mathcal{L} \propto \sqrt{\varepsilon}$  as in Figure 4.20.

## 4.4. Two-Particle Dispersion in Spiral Defect Chaos

We consider the relative displacement of particle pairs, which each show particle diffusion and are initialized at identical midplane locations within the fluid. With the absolute positions  $\vec{x}_i$  of a particle  $i$  within the fluid volume, we denote the relative displacement vector  $\vec{r}_{ij}$  between particles  $i$  and  $j$  as

$$\vec{r}_{ij} := \vec{x}_j - \vec{x}_i. \quad (4.16)$$

As a measure of the relative average distance between particle pairs with an initial separation distance  $\vec{r}_{ij}(t_0)$ , we consider the Lagrangian pair dispersion that we introduced in Equation (2.40) (Section 2.5),

$$R^2(t) := \langle [\vec{r}_{ij}(t) - \vec{r}_{ij}(t_0)]^2 \rangle. \quad (4.17)$$

As discussed by Fyrillas *et al.*[17], the effective diffusivity (also called *dispersivity*) of a diffusive passive scalar can be defined in the Lagrangian frame just like in the Eulerian frame. In analogy to the effective diffusivity  $\mathcal{L}^*$  (Eq. (4.6)), we define the effective Lagrangian diffusivity at time  $t$  as

$$\mathcal{L}_L^*(t) := \frac{R^2(t)}{4t\cdot\kappa} \quad (4.18)$$

and the time-averaged Lagrangian effective diffusivity  $\mathcal{L}_{L,\text{avg}}^*$  as

$$\mathcal{L}_{L,\text{avg}}^* := \langle \mathcal{L}_L^*(t) \rangle_t. \quad (4.19)$$

These effective diffusivities are based on the model of diffusion in a two-dimensional system, which needs to be kept in mind when considering short time scales where dispersion in the vertical dimension plays a role.

For two particles that each have a diffusivity  $\mathcal{D}$ , the total distance between them in a fluid at rest follows the distribution

$$\begin{aligned} \rho(\vec{r}, t) &= \frac{1}{2\pi\sigma^2} \int d\vec{x}_i \int d\vec{x}_j \delta(\vec{r} - \vec{x}_i - \vec{x}_j) \exp\left[-\frac{|\vec{x}_i|^2 + |\vec{x}_j|^2}{2\sigma^2}\right] \\ &= \frac{1}{2\pi\sigma^2} \int d\vec{R}_{ij} \int d\vec{r}_{ij} \delta(\vec{r} - \vec{r}_{ij}) \exp\left[-\frac{2|\vec{R}_{ij}|^2 + \frac{1}{2}|\vec{r}_{ij}|^2}{2\sigma^2}\right] \\ &= \frac{1}{\sqrt{4\pi\sigma^2}} \exp\left[-\frac{|\vec{r}|^2}{4\sigma^2}\right], \end{aligned} \quad (4.20)$$

with the center of mass at  $\vec{R}_{ij} = \frac{1}{2}(\vec{r}_i + \vec{r}_j)$  and the standard deviation  $\sigma^2 = 6\mathcal{D}t$ . This corresponds to a process of normal diffusion with a relative diffusivity of

$$\mathcal{D}_{\text{rel}} = 2\mathcal{D}. \quad (4.21)$$

Compared to the development of the second moment with time (Section 4.3), we therefore expect

to find stronger diffusion by a factor of two for very short times, when all particles and thus their center of mass get advected in a nearly homogeneous flow field.

### Behavior for Short Times

Figure 4.22 shows the increase of  $R^2$  with time for the different particle diffusivities, in SDC at  $\varepsilon = 0.4$ . The convection pattern is similar to that of Figure 4.2 in Section 4.1. For very short times ( $t < 0.05 \tau_v$ ), the pair dispersion increases like

$$R^2(t) = 6 \cdot 2\mathcal{D} \cdot t, \quad (4.22)$$

as we expect for the squared distance between two tracers of individual diffusivity  $\mathcal{D}$  in a three-dimensional isotropic fluid at rest. At these short times, direction and strength of advection seems highly correlated for the particle pairs. Around  $t = 0.1 \tau_v$ , the pair dispersion shows a steeper increase and deviates from this value. This behavior appears to depend rather on total diffusion time than on the total distance between the particles, even though the time of the transition is much lower than the vortex turnover time, which is on the order of the thermal vertical diffusion time (see the increase of the velocity scale  $U$  with  $\varepsilon$  in Figure 4.19, Section 4.3.3). We expect to find a ballistic regime with  $R^2 \propto t^2$  for  $\mathcal{L} \ll 1$  after the normal diffusion regime, but do not observe this at the chosen parameters.

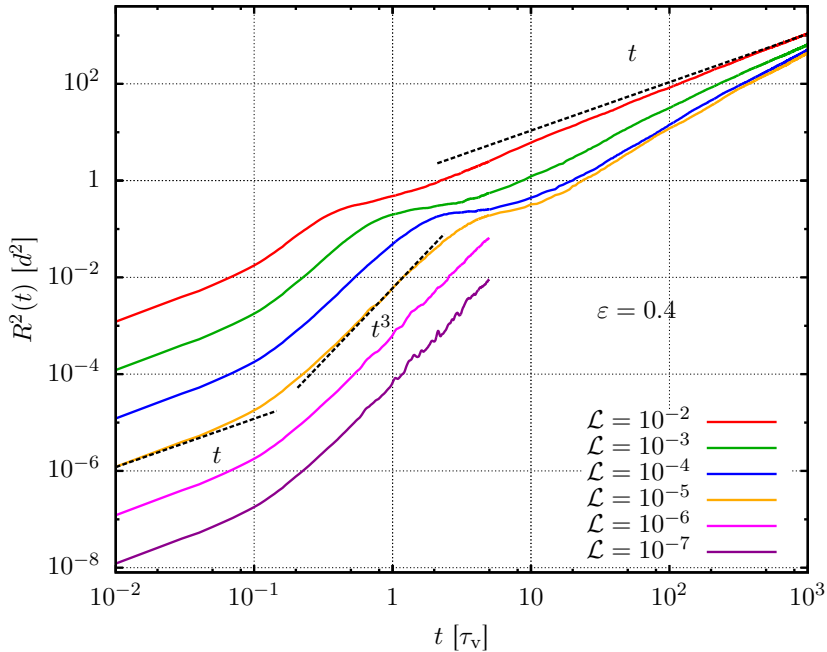


Figure 4.22.: Pair dispersion  $R^2(t)$  of tracer particles, in a periodic system of aspect ratio  $\Gamma = 100$  at  $\varepsilon = 0.4$ ,  $Pr = 1$ , for different particle diffusivities  $\mathcal{L}$ . The lines show the average over 10 simulations with  $N \geq 500$  particle pairs each, at an initial separation of  $r(t_0) = 0$ . Different trajectories were used for  $t < 5 \tau_v$  and  $t \geq 5 \tau_v$ . Dashed lines serve as a guide to the eye.

#### 4. Particle Transport in Spiral Defect Chaos

##### Behavior for Medium Times

After the initial linear increase follows a short period with a super-diffusive increase in the pair dispersion of the form

$$R^2(t) \propto t^3, \quad (4.23)$$

in which  $R^2$  increases up to  $R^2 \approx 0.1 d^2$  followed by a plateau. Dividing the pair dispersion by  $4\kappa \cdot t$  gives the effective diffusivity  $\mathcal{L}_L^*(t)$  (Equation (4.18)), which is shown for different  $\varepsilon$  in Figures 4.23, 4.24 and 4.25. Here we can see that for the plateau, the diffusivity decreases; the dispersion grows slower than for a normal diffusive process. The plateau is on the vortex turnover time scale, and can be explained by the finite size of the convection rolls, which poses a natural boundary to the particle dispersion. Particles can only change their convection roll by diffusion, which is orders of magnitude slower than advection. We observe in Figure 4.22 that the behavior for the different  $\mathcal{L}$  has a similar structure and occurs at the same  $R^2$  but different times  $t$ , because the advection process depends on the spatially correlated flow structures but not the time. The quantitative value of the plateau is  $R^2 \approx 0.5 d^2$ , which corresponds to a particle distance of

$$R_{\text{plateau}} \approx 0.7 d. \quad (4.24)$$

It is remarkable that, of those particles that have a large contribution to  $R^2$ , such a large number move towards each other that the total dispersion is almost constant in time for this short interval.

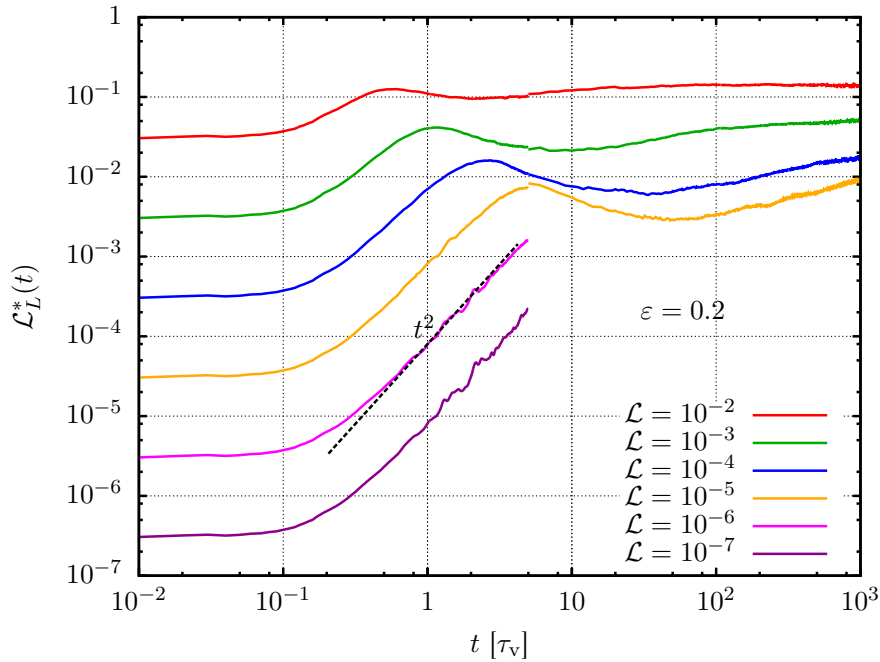


Figure 4.23.: Lagrangian diffusivity  $\mathcal{L}_L^*(t)$  in ISR at  $\varepsilon = 0.2$  for the different diffusivities  $\mathcal{L}$  of the particles. Simulation details as in Figure 4.22.

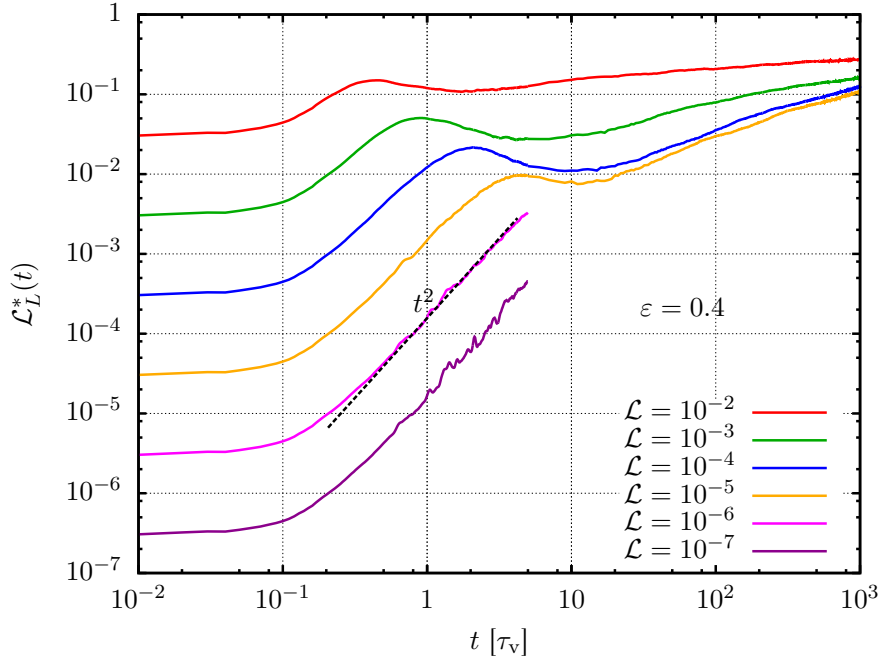


Figure 4.24.: Lagrangian diffusivity  $\mathcal{L}_L^*(t)$  at  $\varepsilon = 0.4$  for the different diffusivities  $\mathcal{L}$  of the particles.  
Simulation details as in Figure 4.22.

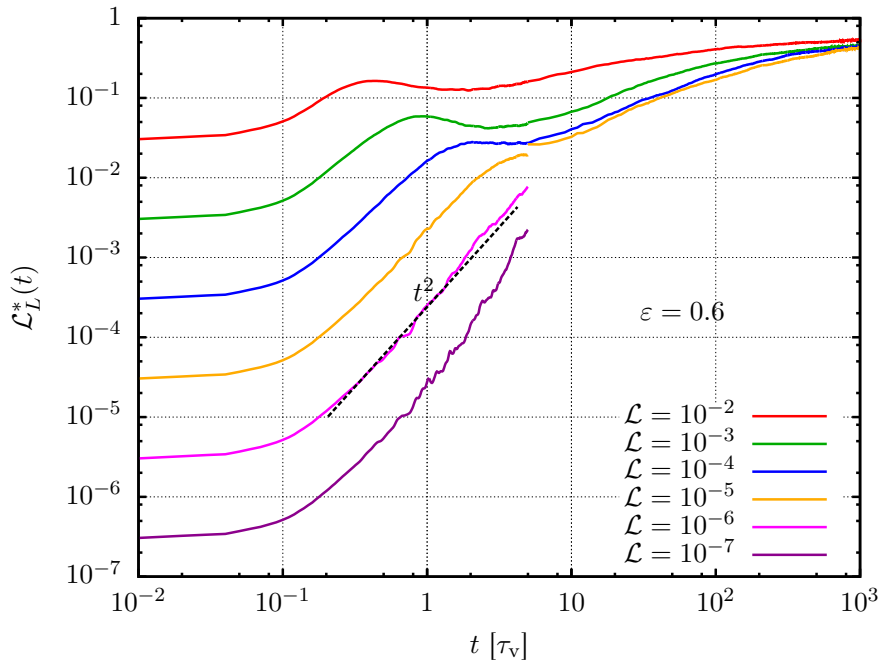


Figure 4.25.: Lagrangian diffusivity  $\mathcal{L}_L^*(t)$  at  $\varepsilon = 0.6$  for the different diffusivities  $\mathcal{L}$  of the particles.  
Simulation details as in Figure 4.22.

### Behavior for Long Times

After the plateau, dispersion yet again rises superlinear, but converges towards normal diffusive  $R^2(t) \propto t$  behavior. It takes several orders of magnitude in time for the diffusivity to move towards some asymptotic value, which appears to be reached faster for higher  $\varepsilon$ . At  $\varepsilon = 0.6$ , the time to get close to the asymptotic value is around  $10^3 \tau_v$ , for smaller  $\varepsilon$  we did not run the simulations for long enough to draw definite conclusions. At  $\varepsilon = 0.6$ , the asymptotic value for

$$\mathcal{L}_L^*(t)|_{t \rightarrow \infty}, \quad (4.25)$$

which can also be defined as an effective diffusivity (see [17]), is almost the same for all  $\mathcal{L}$ . If this asymptotic value is independent of the particle diffusivity, it must be a transport property of the flow field rather than of the individual particles.

#### 4.4.1. Radial Distribution

To show how the tracer particles are distributed within their rolls, we consider the distribution of their horizontal separation at different times. The radial distribution function  $g_{xy}(R)$  integrates the density  $\rho(R)$  of particles with a horizontal radial distance between  $R$  and  $R + dr$ , with  $dr \ll 1$ , and normalizes this quantity by the area between the two radii:

$$g_{xy}(R) := \frac{1}{2\pi R \cdot dr} \int_R^{R+dr} \rho(R) dR \quad (4.26)$$

This radial correlation provides insights into the development of the effective Lagrangian diffusivity that we see in figures 4.23 to 4.25, and is displayed in Figure 4.26. For small  $t$ , where we observed the increase in radial dispersion of  $R^2 \propto t^3$ , the radial distribution moves away from the initial Gaussian towards a broader distribution<sup>1</sup>. However, as the distribution tail reaches the distance of  $R \approx 1.2 d$  (which is the approximate width of a convection roll in the ISR system), it shows a characteristic decrease in radial density. Some sort of barrier is present at the width of one convection roll, which, as we discussed in Section 4.2.1, is the separatrix between neighboring rolls. While mixing within each roll is strongly enhanced, this barrier is the cause for the plateau in  $R^2(t)$ . Even in the highly irregular SDC system at  $\varepsilon = 0.6$ , where convection rolls of different width and also defects exist, the barrier is visible in the radial distribution function. Beyond the time of mixing within one roll, an increasing number of particles have separations of several roll widths, and the tails have an increasingly strong impact on the average dispersion of the particles. This is the regime where the large-scale structure and dynamics of the flow field dominates transport, and the local flows within an individual convection roll become less important.

---

<sup>1</sup>At Lewis number  $\mathcal{L} = 10^{-5}$ , the  $R^2 \propto t^3$  increase happens for times  $t < 5 \tau_v$ , which are covered by the red and green curve in Fig. 4.26.

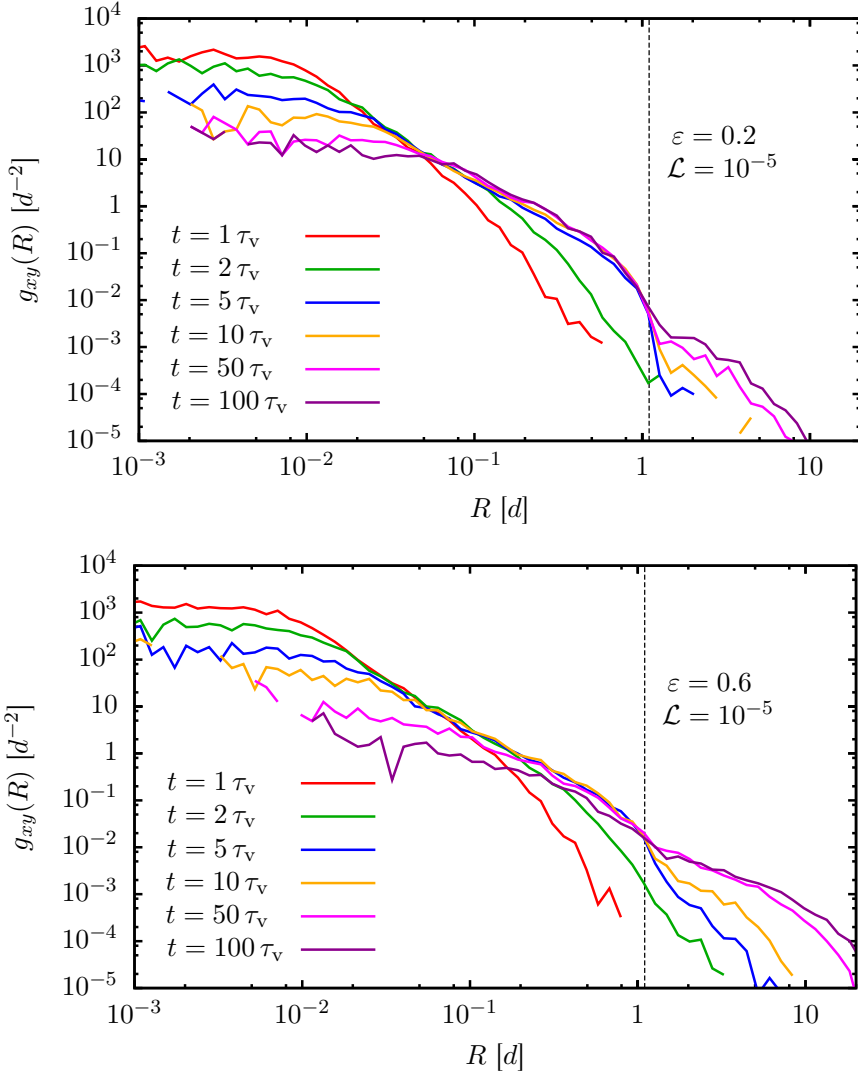


Figure 4.26.: Horizontal radial distribution function  $g_{xy}(R)$  of particle pairs diffusing with  $\mathcal{L} = 10^{-5}$ , for straight rolls at  $\varepsilon = 0.2$  and Spiral Defect Chaos at  $\varepsilon = 0.6$ , at different times  $t$ . Figures 4.23 and 4.25 show the corresponding Lagrangian diffusivities.

#### 4.4.2. Horizontal and Vertical Dispersion

By only considering the horizontal or vertical components of the distance vector  $\vec{r}_{ij}$  between two particles, we can see how the dispersion in the horizontal and vertical directions add up to the total dispersion. As the height of the large aspect ratio Bénard system is very limited compared to its width, we expect to find different behavior for these two cases. In analogy to the Lagrangian pair dispersion (Eq. (4.17)), we define the horizontal dispersion

$$R_{xy}^2(t) := \langle [\Delta x_{ij}(t) - \Delta x_{ij}(t_0)]^2 + [\Delta y_{ij}(t) - \Delta y_{ij}(t_0)]^2 \rangle \quad (4.27)$$

#### 4. Particle Transport in Spiral Defect Chaos

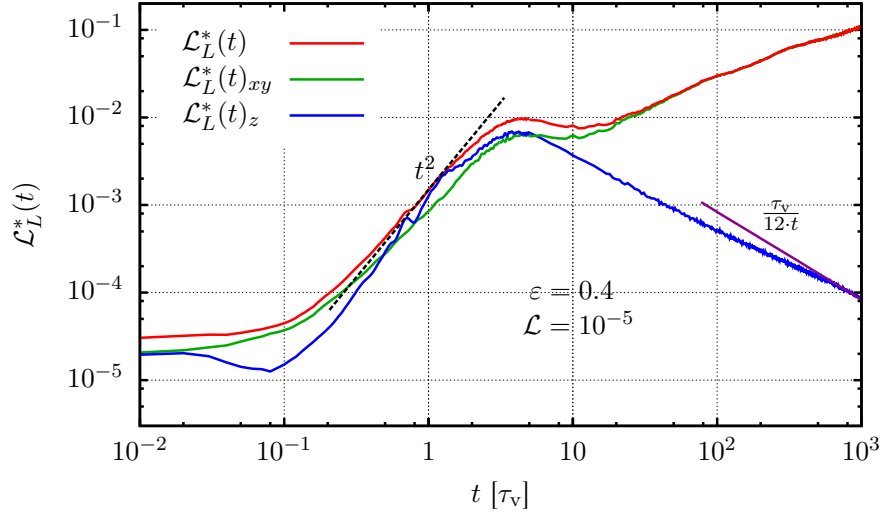


Figure 4.27.: Lagrangian diffusivity  $\mathcal{L}_L^*(t)$  at  $\varepsilon = 0.4$  and  $\mathcal{L} = 10^{-5}$  of the particles, for the horizontal and vertical components of the dispersion. Periodic system at  $\varepsilon = 0.4$ ,  $Pr = 1$ ,  $\Gamma = 100$ , with  $N \geq 500$  particle trajectories. The purple line is  $\frac{\tau_v}{12 \cdot t}$ .

and the vertical dispersion

$$R_z^2(t) := \langle [\Delta z_{ij}(t) - \Delta z_{ij}(t_0)]^2 \rangle. \quad (4.28)$$

Note that the pair dispersion can be calculated from the horizontal and vertical dispersions by the relation  $R^2(t) = R_{xy}^2 + R_z^2(t)$ . In analogy to definition (4.18), we denote the horizontal Lagrangian diffusivity by

$$\mathcal{L}_L^*(t)_{xy} := \frac{R_{xy}^2(t)}{4t \cdot \kappa} \quad (4.29)$$

and the vertical Lagrangian diffusivity by

$$\mathcal{L}_L^*(t)_z := \frac{R_z^2(t)}{2t \cdot \kappa}. \quad (4.30)$$

Figure 4.27 shows one example for the time development of the different diffusivities. Initially, the horizontal and vertical Lagrangian diffusivity both have a magnitude of twice the particle diffusivity  $\mathcal{L}$ , as we would expect. The effective Lagrangian diffusivity  $\mathcal{L}_L^*(t)$  is, like the horizontal diffusivity, defined for two dimensions, but measures a three-dimensional normal diffusion for short times and is therefore larger than the horizontal and vertical Lagrangian diffusivities by a factor of  $3/2$ . We notice a decrease in  $\mathcal{L}_L^*(t)_z$  around  $t = 0.1 \tau_v$ , which is characteristic for a horizontal stretching of the flow field. Despite our noisy data, we then see an increase with a  $t^2$  slope for both the horizontal and the vertical effective diffusivities, up to the plateau that we consistently observe for all different Rayleigh numbers and diffusivities. However, after the plateau, the vertical dispersion cannot increase any further due to the limited vertical system extent. If the vertical

positions of particle pairs are uncorrelated and evenly distributed along  $\Omega_z$ , we expect a dispersion of

$$R_{\text{even}}^2 = \int_{\Omega_z} dz_i \int_{\Omega_z} dz_j (z_i - z_j)^2 = \frac{d^2}{6}. \quad (4.31)$$

We observe that  $\mathcal{L}_L^*(t)_z$  approaches the function

$$\frac{\tau_v}{12 \cdot t} = \frac{R_{\text{even}}^2}{2t \cdot \kappa}, \quad (4.32)$$

which matches the expected behavior.

#### 4.4.3. Influence of Diffusivity on Effective Dispersion

By looking at the pair dispersion an Lagrangian diffusivity, we found that the long-term transport properties in Rayleigh-Bénard convection are largely independent of the individual particle diffusivities, but strongly depend on the Rayleigh number and strength of convective motion. Still, we want to find out how the advection enhances the diffusion process for particle pairs for intermediate time scales. With the effective Lagrangian diffusivity  $\mathcal{L}_L^*$ , we can define the Lagrangian diffusion enhancement

$$\Delta_L := \frac{\mathcal{L}_L^* - \mathcal{L}}{\mathcal{L}}, \quad (4.33)$$

which we can set in relation to the Péclet number

$$\mathcal{P} = \frac{d}{\kappa} \cdot \frac{U}{\mathcal{L}} \quad (4.34)$$

that is the ratio of advective and diffusive mass transport, as described in Section 4.3.3. The similarities between the diffusion enhancement  $\Delta$  in the Eulerian frame (Eq. (4.8) in Section 4.3.3) and the Lagrangian diffusion enhancement  $\Delta_L$  can be nicely seen in comparing Figure 4.18 with Figure 4.28. We again see the transition from

$$\Delta_L \propto \mathcal{P}^{1/2}, \quad (4.35)$$

for a large range of  $\mathcal{P}$  in ISR and small  $\mathcal{P}$  in SDC, to

$$\Delta_L \propto \mathcal{P} \quad (4.36)$$

for Spiral Defect Chaos with large  $\mathcal{P}$ . While the  $\mathcal{P}^{1/2}$ -scaling is characteristic for systems in which effective diffusion is dominated by particle transitions between adjacent convection rolls, linear scaling with  $\mathcal{P}$  appears to result from a strong influence of the defect dynamics that is pronounced at high Rayleigh numbers  $\varepsilon$ , and high advection velocities  $U$  compared to the diffusivity  $\mathcal{L}$ . As in Section 4.3.3, we observed a decrease in the diffusivity for  $\mathcal{P} < 10$ , which we attribute to a simulation artefact and do not consider any further.

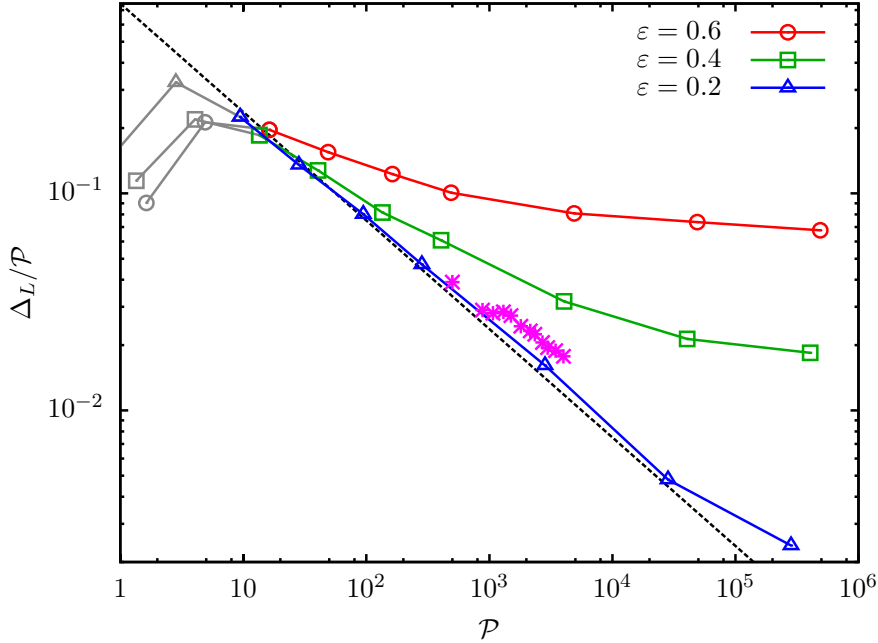


Figure 4.28.: Lagrangian diffusion enhancement ( $\Delta_L/\mathcal{P} \propto (\mathcal{L}_L^* - \mathcal{L})$ ) relative to the Péclet number, in a periodic system at  $\Gamma = 100$ ,  $Pr = 1$ , for different  $\varepsilon$ . Stars are measurements for  $\Delta/\mathcal{P}$  from [28] (ISR at  $\varepsilon = 4.5$ ). The dashed line is  $\Delta \propto \mathcal{P}^{1/2}$ .

#### 4.4.4. Influence of Rayleigh Number on Effective Dispersion

We now investigate how the effective dispersion is enhanced by an increase in Rayleigh number. We know that the Rayleigh number effect is two-fold, as it both boosts the flow velocity  $U$  in the convection rolls and induces mean flows and the formation of more and more defects in the convection pattern.

Figure 4.29 shows the Lagrangian diffusivity at the same particle diffusivities, but for different Rayleigh numbers. We have normalized our time by the average flow velocity  $U$  and thus measure it in the vertical advection time  $d/U$ . For the different  $\varepsilon$ , the flow velocity  $U$  lies between  $2.8 d/\tau_v$  and  $4.9 d/\tau_v$ , see also Figure 4.19. With this scaling, the curves collapse for small times, and  $\mathcal{L}_L^*(t)$  increases with  $t^2$  up to a peak. The peak is higher for larger  $\varepsilon$ . The faster defect dynamics and smaller size of convection roll patches at higher  $\varepsilon$  limits the time in which  $\mathcal{L}_L^*(t)$  decreases after the first peak: At high  $\varepsilon$ , diffusivity rises again sooner and thus reaches a higher effective diffusivity for  $t > 10\tau_v$ .

The increase of Lagrangian diffusivity with  $\varepsilon$  is shown in Figure 4.30. Here, we see a transition from an almost constant effective Lagrangian diffusivity for  $\varepsilon < 0.3$  to a linear increase at  $\varepsilon > 0.4$ . Unlike we would expect from considering the Péclet number dependence of diffusion enhancement, the effective diffusivities for different  $\mathcal{L}$  are different. The effective diffusivity  $\mathcal{L}_L^*$  is orders of magnitude larger than the particle diffusivity  $\mathcal{L}$ . Note that the transition point at which  $\mathcal{L}_L^*$  starts to increase significantly lies well above the onset of SDC in the system. Close to onset, the density of defects increases, but only near  $\varepsilon = 0.4$  do the defects dominate against shrinking patches of

straight rolls. The diffusive transport seems to depend on that defect density rather than the pure existence of any defects in the system, and transitions smoothly with increasing  $\varepsilon$ .

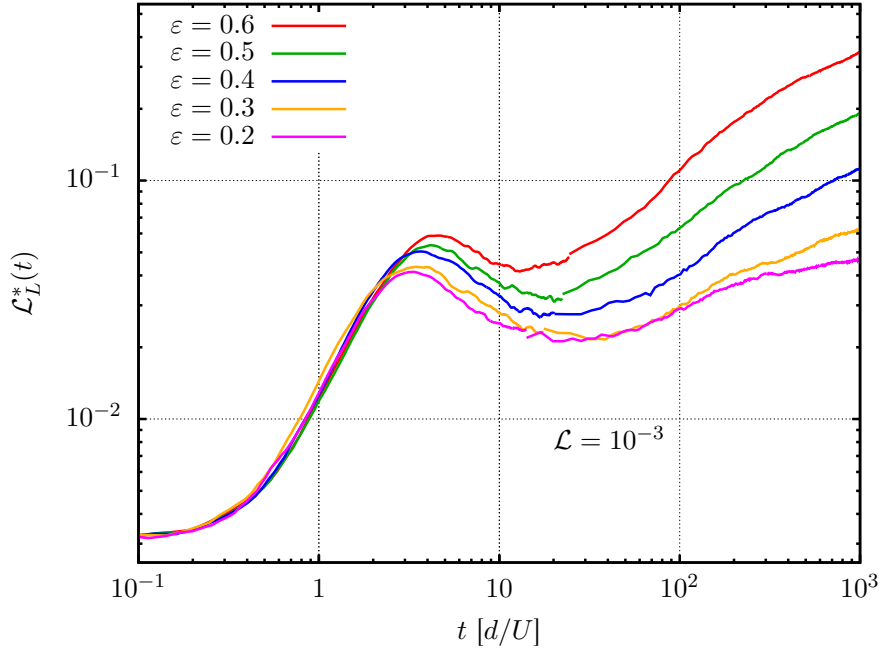


Figure 4.29.: Lagrangian diffusivity for tracer trajectories with particle diffusivity  $\mathcal{L} = 10^{-3}$ , at different Rayleigh numbers  $\varepsilon$  in a periodic system of aspect ratio  $\Gamma = 100$  at  $Pr = 1$ .

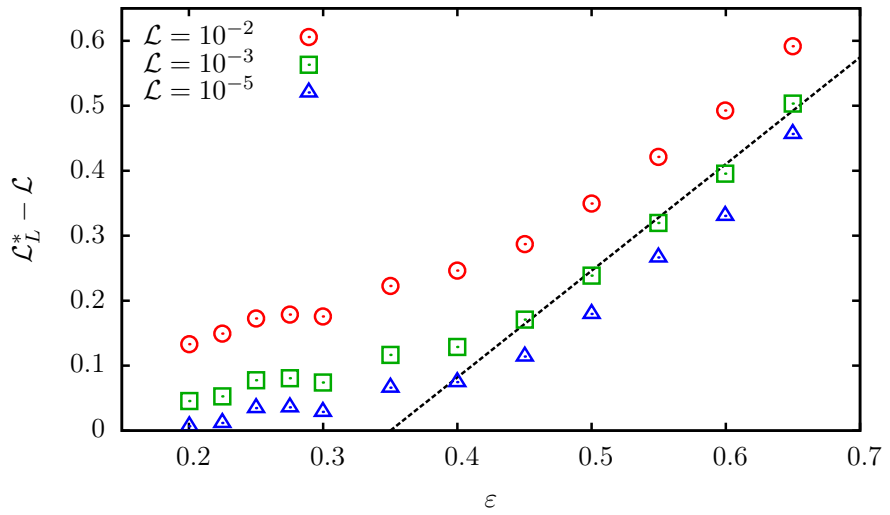


Figure 4.30.: Lagrangian effective diffusion enhancement  $\mathcal{L}_L^* - \mathcal{L}$  relative to the reduced Rayleigh number  $\varepsilon$ , in a periodic system with  $\Gamma = 100$ ,  $Pr = 1$ . The dashed line is  $\mathcal{L}_L^* - \mathcal{L} \propto (\varepsilon - 0.35)$  and serves as a guide to the eye.

#### 4.4.5. Dislocation Effects on Dispersion Enhancement

We observe that, at parameters where ISR and SDC coexist, the diffusion enhancement is stronger for SDC. We want to determine whether the enhancement is caused by the pure existence of defects in the fluid, or whether the spatiotemporal dynamics is needed. To differentiate between the effects of the defects alone, and those of the temporal dynamics, we consider three types of systems at identical parameters: One system type is initialized with an ISR pattern at  $q = \frac{8\pi}{10d}$ , the second is in the SDC state but static in time, the third system is fully developed SDC that changes with time. The wave number for the ISR system was chosen according to experimental findings from Plapp[21] (see Figure 2.2). Examples for the SDC patterns that were used in both the static and the dynamic simulations of SDC are shown in Figure 4.33.

Figure 4.31 shows the dispersion in the three systems. For  $t < \tau_v$ , the curves collapse, while for  $t > \tau_v$ , dispersion is larger for SDC than for ISR regardless of any time dependence. The characteristic velocity is  $U_{\text{ISR}} = 6.0d/\tau_v$  in the Straight Roll system and  $U_{\text{SDC}} = 5.6d/\tau_v$  in Spiral Defect Chaos. This difference of less than 10% in advection velocity is likely not the reason why dispersion in SDC is an order of magnitude larger than in ISR for long times. Apparently, dispersion depends on the existence of mean flows and defects in the system, not on their change over time. We even observe an increased dispersion in the static flow field with respect to the dynamic physical system. We attribute this to mean flows that carry particles out of convection rolls, while they would actually move the whole convection roll in dynamic SDC and thus contain the particle in that roll.

In the dependence of Lagrangian diffusion enhancement  $\Delta_L$  on the Péclet number  $\mathcal{P}$  (Figure 4.32), we again observe the typical  $\mathcal{P}^{1/2}$ -scaling for ISR and the transition to a scaling of  $\Delta_L \propto \mathcal{P}$  for SDC, even in systems at identical Rayleigh numbers. The mean flows, which are driven by

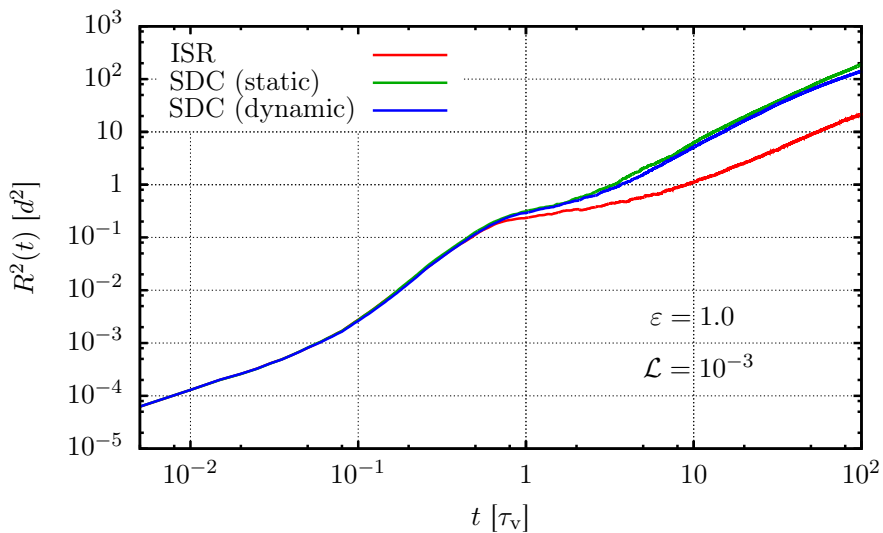


Figure 4.31.: Development of the two-particle dispersion  $R^2(t)$  of the tracer particles, in a periodic system of aspect ratio  $\Gamma = 50$  at  $Pr = 1$ ,  $\varepsilon = 0.8$ ,  $\mathcal{L} = 10^{-3}$ . The lines show the average over 20 simulations with  $N = 10^3$  particles each.

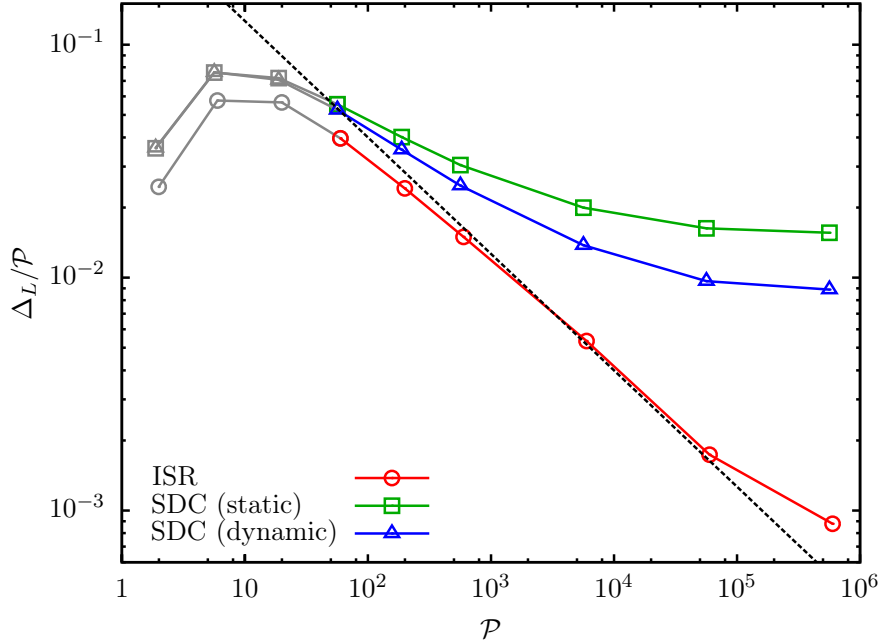


Figure 4.32.: Lagrangian diffusion enhancement  $\Delta_L/\mathcal{P}$  relative to the Péclet number, in a periodic system at  $\Gamma = 50$ ,  $Pr = 1$ ,  $\varepsilon = 0.8$ . The dashed line is  $\Delta \propto \mathcal{P}^{1/2}$ .

defects and curvature in convection rolls, appear to be responsible for the dispersion of particles, especially if the particle diffusion is very small compared to the scale of fluid velocity. Whether the roll pattern actually changes with time or not plays only a minor role; in fact the “frozen” system, where advective motion follows the stream lines, has a faster dispersion than a system with temporal dynamics.

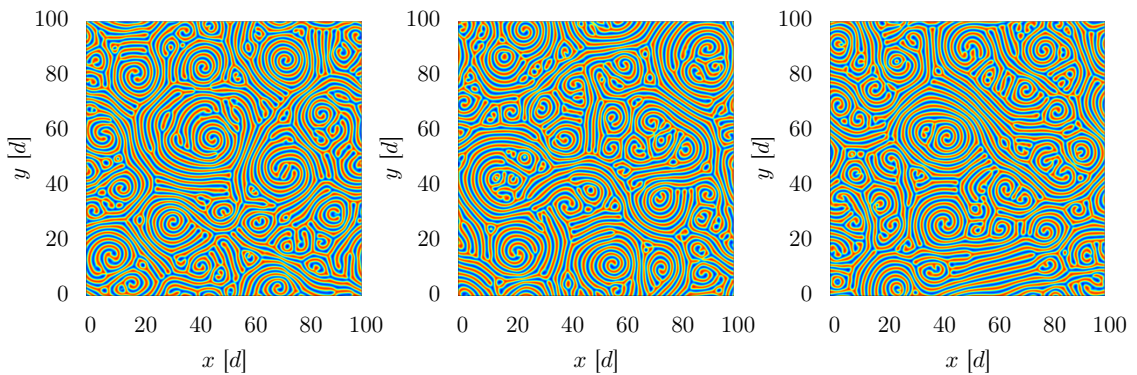


Figure 4.33.: Midplane temperatures for three systems that were used to investigate transport in static and dynamic SDC, at  $\Gamma = 50$ ,  $Pr = 1$ ,  $\varepsilon = 0.8$ .

## 4.5. Irreversibility of Convective Flow

It has recently been suggested[31] that in dissipative flows, the lack of reversibility can be characterized by an asymmetry between the acceleration and deceleration of particles in the flow field. Observations have shown that tracer particles build up kinetic energy over longer time scales than they dissipate that energy.

We investigate energy increments and decrements for the Spiral Defect Chaos state of Rayleigh-Bénard convection, which shows a laminar, yet irreversible spatiotemporal behavior and, due to the large aspect ratio, can show characteristics of both two-dimensional and three-dimensional flows. We consider the relative kinetic energy per unit mass of a fluid particle,

$$E(t) := \frac{v^2(t)}{2}, \quad (4.37)$$

and investigate the work (change in energy) over a time interval  $\tau$ ,

$$W(\tau) := E(t + \tau) - E(t) = \frac{v^2(t + \tau) - v^2(t)}{2}. \quad (4.38)$$

If energy gains and losses of the particles occur on different time scales, this will be visible in the moments of  $W(\tau)$ . While the first moment will vanish for a stationary flow, and the second moment is not sensitive to the sign of  $W(\tau)$ , the third moment will carry information about an asymmetry in the time scales of energy gains and losses. In a time reversible flow, we expect the third moment to vanish, as detailed balance results in equal probabilities for energy losses and gains. Figure 4.34 shows the quantity  $-\langle W^3(\tau) \rangle$ , averaged over particles and time, for Rayleigh-Bénard convection at different Rayleigh numbers.

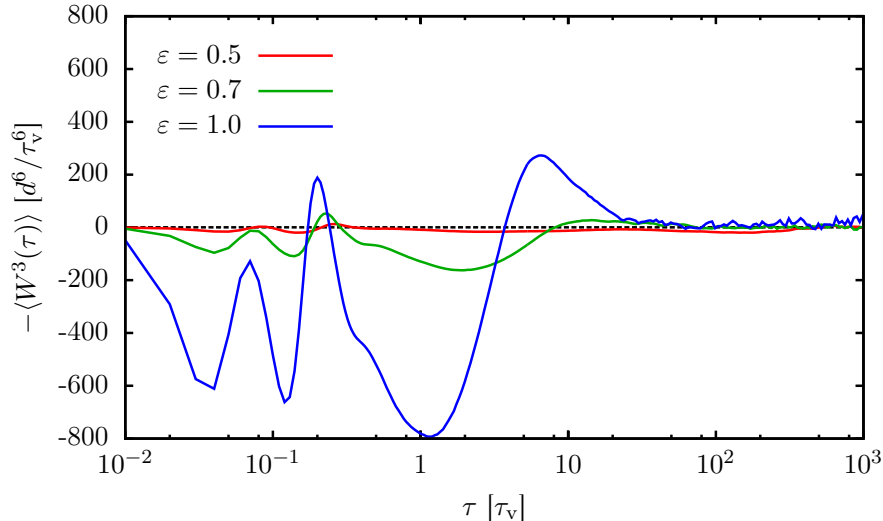


Figure 4.34.:  $-\langle W^3(\tau) \rangle$ , averaged over time  $T = 10^4 \tau_v$  and  $N = 10^3$  particle trajectories, at  $Pr = 1$  in a periodic system of  $\Gamma = 50$ . At  $\varepsilon = 0.5$ , the pattern consists of ISR with few dislocations, while at higher  $\varepsilon$  we observe SDC. A small amount of particle diffusion ( $\mathcal{L} = 10^{-5}$ ) was added to improve spatial sampling.

$\varepsilon$	$v_{\max} [d/\tau_v]$	$\tau_{vt} [\tau_v]$
0.5	11.2	0.28
0.7	13.5	0.23
1.0	16.7	0.19

Table 4.1.: Convection flow velocities for different Rayleigh numbers at  $Pr = 1$ ,  $\Gamma = 50$ , and the vortex turnover time scale, which we approximate by the lower bound  $\tau_{vt} = \pi d/v_{\max}$ .

At an aspect ratio of  $\Gamma = 50$ , the reduced Rayleigh number  $\varepsilon = 0.5$  is below the onset of SDC and represents an ISR system with few dislocations. In this system,  $\langle W^3 \rangle$  is very low. At  $\varepsilon = 0.7$ , SDC has set in, and some dislocations are present in the system.  $\varepsilon = 1.0$  represents strongly driven SDC with many dislocations. It must be noted that for the different Rayleigh numbers, the strength of convection and thus the vortex turnover time differs (up to a factor of 1.5, see Table 4.1). However, the difference in the third moment of  $W(\tau)$  is much more pronounced. For small times  $\tau < 10 \tau_v$ , the value is mostly negative and shows distinct maxima and minima. The negative values of  $-\langle W^3(\tau) \rangle$  correspond to time scales on which an energy gain takes place. At

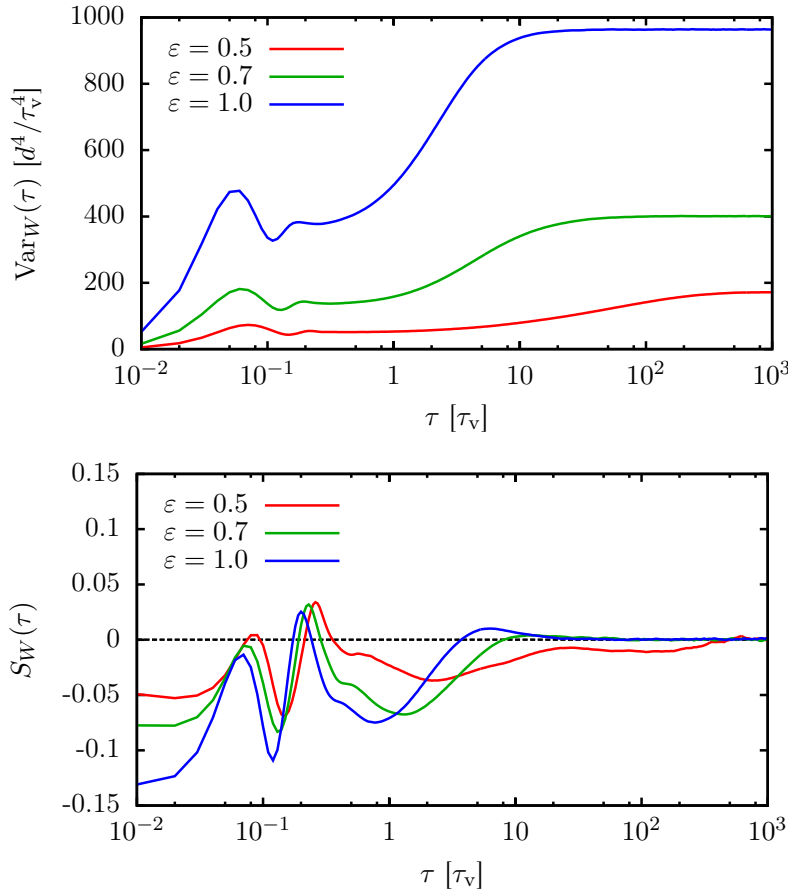


Figure 4.35.: Variance and skewness of  $W(\tau)$ , averaged over 1000 particle trajectories in Rayleigh-Bénard convection (details see caption of Figure 4.34).

#### 4. Particle Transport in Spiral Defect Chaos

$\tau \approx 0.2 \tau_v$  and above  $\tau = 5 \tau_v$ , energy is lost; the long-term correlation drops to zero. From these results, we see that the particles gain energy on the very short timescales, and lose the energy over a larger timescale.

To achieve a better spatial sampling, and to avoid an artefact of our time stepping scheme<sup>2</sup>, we add a diffusion process with  $\mathcal{L} = 10^{-5}$  to move the particles through the fluid. Diffusion of  $\mathcal{L} = 10^{-5}$  will result in a standard deviation of  $\sigma = 0.45 d$  in a time of  $\Delta t = 10^3 \tau_v$ , moving the particle from the center to some arbitrary location inside the convection roll. The particle energy per mass, which is on the order of  $E \approx 15 d^2 / \tau_v^2$ , is only influenced by a disturbance of order  $\delta E \approx 10^{-4} d^2 / \tau_v^2$ . Figure 4.35 shows the variance

$$\text{Var}_W(\tau) := \langle W^2(\tau) \rangle \quad (4.39)$$

and skewness

$$S_W(\tau) := -\frac{\langle W^3(\tau) \rangle}{\langle W^2(\tau) \rangle^{3/2}}. \quad (4.40)$$

As the variance reaches a plateau for large  $\tau$ , the skewness drops to zero. The constant acceleration of circular motion in convection rolls does not contribute to changes in energy, and in ISR, a change in energy is indicative of a change in the position of a particle's orbit in a convection roll. The final plateau in the variance indicates that particles have assumed a completely different location in the roll pattern. Due to the fast dynamics, this happens at  $\tau \approx 10 \tau_v$  for  $\varepsilon = 1$ , but particles stay in their roll for as long as  $\tau = 500 \tau_v$  in ISR, where only the small effect of diffusion can move them around. The results suggest that the asymmetry in the acceleration statistics is limited to a range  $\tau \leq 20 \tau_v$ . We note that normalizing times for the different systems by their respective vortex turnover time scale moves the extrema of the moments closer together, but does not make them collapse. We also note that, due to the error discussed in Appendix A.3, the spatiotemporal chaos of the system was not a perfect implementation of Spiral Defect Chaos; yet the property of temporal irreversibility and the dependence of the pattern on  $\varepsilon$  remained the same.

---

<sup>2</sup>For large simulation time steps, the particles of the ISR system would follow an inward spiraling motion on the time scale  $\Delta t = 10^3 \tau_v$ .

# 5. Conclusions and Outlook

The work and results shown in this thesis fall into two categories. On one hand, we continued work on a high-performance, GPU-parallelized Galerkin solver for the incompressible Boussinesq equations, which we combined with a high-order scheme for the tracing of diffusing particles. On the other hand, we investigated the Spiral Defect Chaos state of Rayleigh-Bénard convection in high aspect ratio systems, and its transport properties, by considering Lagrangian trajectories of passive tracer particles. We will first discuss our work on the numerical solver, and later focus on the insights regarding transport in thermal convection.

## 5.1. Parallelized Galerkin Solver and Particle Tracer

As noted above, the numeric simulation of the convective flow field is based on the implementation by J. Zudrop[32]. By using his work, we could focus our efforts on efficiency and accuracy of the scheme. We performed an additional verification of the code and discovered two significant errors: In the nonlinear operator, we identified occasions where operations would only be performed on coefficients of the first vertical mode due to an insufficient grid size. Additionally, two terms of the operator had a wrong indexing for the Chandrasekhar overlap integrals and would thus use wrong coefficients. We did thorough tests regarding the effect of these two errors on the resulting flow field. Unfortunately, some of the simulations in this thesis had already been performed when the second error was discovered, these instances have been marked in the discussion of the respective results. An additional discussion of the error and its effects can be found in Appendix A.3.

The strongest limitation of the preexisting implementation was the limitation in its vertical resolution to two spectral modes, which severely limited the applicability of the scheme to near-onset convection. The main reason for limiting the number of vertical modes was that for  $N_z = 2$ , the submatrices of the linear operator were diagonal and their inverse could easily be calculated. To allow for larger  $N_z$ , we added a pre-computation step to the linear operator, which inverts these matrices on the host and stores them in device RAM where they are being accessed every time step. Values for the overlap integrals of the Chandrasekhar and Sine functions, which had previously been hardcoded into the source code, are now being calculated during initialization from their analytic forms for the required number of modes. The limitations for the number of vertical modes are now the size of the device memory, as the requirement grows linear with the number of modes, and the runtime, which has the complexity  $\mathcal{O}(N_z^3)$ . The latter is a severe limitation even for small systems, and we ran simulations at  $N_z > 5$  for testing purposes only.

Our optimizations in kernel calls and memory accesses had a large impact on the runtime performance: For a standard simulation of size  $N_x \times N_y \times N_z = 512 \times 512 \times 2$ , these changes reduced the runtime per time step on the GTX680 device from an average 88 ms to an average 45 ms.

## 5. Conclusions and Outlook

We attribute this improvement by a factor of 2 mainly to a massive reduction in the number of kernel calls, which we accomplished by creating long and specialized kernels, which combined the effects of many short kernels without changes to the simulation scheme. Additionally, we were able to combine two large terms of the nonlinear operator into one (terms 6 and 7 of Eq. A.17a), eliminating  $\mathcal{O}(N_z^3)$  large kernel calls in every time step.

We added the capability to configure the simulation via multiple command-line arguments. The command-line configuration makes use of an input parser to interpret the command line string. With this new method, we can compile one binary program file and use it for many different types of simulations.

## Outlook

Due to the object-oriented modular structure of the software package, additional features can easily be implemented. One easy and effective modification of the simulation scheme is a higher-order solver for the linear operator, for example the second-order Crank-Nicolson method. This method would replace Equation (3.35b) in Section 3.1.6 by the term

$$V_{t+1} = (1 - \frac{dt}{2} \cdot B^{-1}L)^{-1} (1 + \frac{dt}{2} \cdot B^{-1}L) [V_t + \tilde{V}_{t+1}], \quad (5.1)$$

which can easily be implemented in the initialization of the implicit linear operator and does not involve any runtime overhead for the individual time steps. Since the damping effect of the implicit Euler method is lost in the Crank-Nicolson scheme, time steps with the implicit Euler method would have to be applied from time to time.

An additional increase in runtime performance can potentially be achieved by increasing GPU occupancy with CUDA streams. By running multiple kernels in parallel, the GPU scheduler can use all multiprocessors to their full capacity and hide latencies. This concept can be used, for example, to parallelize the evaluation of the independent terms of the nonlinear operator, or even the work on the linear and nonlinear operators. Based on the findings by Zudrop, we believe that using multiple GPU devices for one simulation is not an efficient option for most standard simulations, unless the memory transfer latencies are significantly decreased, and thus recommend to focus future attention on increasing performance on one device.

In the flow field, additional measurements can be made with new operators. Profiles of the vertical vorticity

$$\Omega(x, y) := \int_{\Omega_z} [\vec{\nabla} \times \vec{u}(\vec{x})] \cdot \vec{e}_z \, dz \quad (5.2)$$

and the local mean flow

$$\vec{U}(x, y) := \int_{\Omega_z} \vec{u}(\vec{x}) \, dz \quad (5.3)$$

could open new insights into transport properties of Spiral Defect Chaos, and are easy to implement in our spectral scheme. Heat transport properties can be investigated by calling the temperature operator from the particle tracer and storing the temperatures along the particle trajectories.

## 5.2. Transport Properties of Spiral Defect Chaos

Using the parallelized simulation scheme, we were able to investigate Rayleigh-Bénard convection at very large aspect ratios. At the time scales that we considered, we could not find a sharp transition between ISR at low Rayleigh numbers and SDC for higher  $Ra$ , but rather a continuous increase in defect density and roll curvature that would at some point form spiral patterns. Since the term Spiral Defect Chaos is only loosely defined, a clear definition of its onset cannot be given either. We showed in Section 4.1 four system states along the route from ISR to SDC, after 1.5 horizontal diffusion times, and described their temporal dynamics.

By considering different types of small scale patterns in Section 4.2, we could qualitatively describe local transport properties of the convective flow that would later help us interpret our findings of the transport properties of Rayleigh-Bénard convection. Fast mixing takes place within the individual convection rolls, which can enhance the effects of molecular diffusion by orders of magnitude and quickly homogenizes particle density within one roll. However, particle exchange between adjacent convection rolls is very limited, so that the planes between the rolls separate the fluid volume into compartments, and a steep particle density gradient can develop between them. Still, particle transport perpendicular to roll orientation is much stronger than along the rolls, where only molecular diffusion takes place. Pushing the rolls through the system with a global mean flow has little effect on the mixing; while we assumed that the mean flow would move the particles from convection roll to convection roll in the middle between top and bottom boundary, we actually observed the opposite effect, in that the rolls were pushed through the system, but some particles very close to the top and bottom plates refused to follow, an effect known from Taylor dispersion in pipe flows. Unlike for straight rolls, the flow field around a giant spiral had a strong particle transport along the convection rolls, resulting in a directed transport of particles along the spiral arms. Dislocations were found to strongly enhance particle transport, especially when forming a dislocation line.

When we turned to fully developed Spiral Defect Chaos and used a large number of particles to act as a passive scalar in Section 4.3, we could observe normal diffusion for long time scales, as the variance of the spatial distribution of particles grew linear with time. The slope of this linear increase defines an effective diffusivity, which is always larger than the particle diffusivity and for small diffusivities independent of it. It appears that this effective diffusivity is a characteristic property of the flow in the system. By setting the diffusion enhancement in relation to the Péclet number  $\mathcal{P}$ , which describes the relative strength of advection compared to particle diffusion, we found for large  $\mathcal{P}$  a linear growth of the enhancement with  $\mathcal{P}$ . This happens where the effective diffusivity is independent of the particle diffusivity, as in that case, both the Péclet number and the diffusion enhancement scale are proportional to the inverse particle diffusivity for a given system. This observation has already been made by Chiam *et al.*[11], who however observed a much smaller difference in diffusion enhancement for the different particle diffusivities, and also for the different Rayleigh numbers that they considered.

Looking at the Rayleigh number dependence of the diffusion enhancement, we find in the cell of aspect ratio  $\Gamma = 30$  a strong increase of the enhancement close to the onset of Spiral Defect Chaos at  $\varepsilon = 0.55$ , unlike Chiam *et al.*, who extrapolated from few measurements at higher  $\varepsilon$  and assumed

## 5. Conclusions and Outlook

the enhancement to start right at convection onset at  $\varepsilon = 0$ . Despite the enhanced transport in straight rolls, the high number of defects and temporal dynamics of Spiral Defect Chaos appears to be the real cause for a fast distribution of particles throughout the system. We therefore propose the diffusion enhancement as a quantitative measure for the onset of Spiral Defect Chaos.

The overall picture of particle dispersion in Rayleigh-Bénard convection, which we presented in Section 4.4, is coherent: For times smaller than the roll turnover time scale, particles first disperse like in a normal diffusive process, as long as their distance is very small. Then, due to velocity gradients within the convection rolls, the distance between particles will lead to different velocities, enhancing pair dispersion with a  $t^3$ -law until particles are at random positions within their common roll. Dispersion saturates, and can only grow further when diffusion into adjacent rolls takes place. Strong advection within the rolls makes this a super-diffusive process at first, but for long times, the random nature of hopping between the rolls brings particle transport back to a normal diffusion process, though with a largely enhanced diffusivity. Interestingly, these effects are featured both in ISR and SDC, due to their similar local convection patterns. Defects and local mean flows, which are more common with increasing  $\varepsilon$ , quantitatively enhance dispersion and decrease the time scales on which the flow pattern, rather than the particle diffusivity, determines the effective dispersion.

However, the convergence of the effective dispersion towards a characteristic value, which we found for  $\varepsilon = 0.6$  and suspect as well for lower Rayleigh numbers, raises questions regarding scaling of the diffusion enhancement  $\Delta$  with the Péclet number  $\mathcal{P}$  (Section 4.3.3): If  $\mathcal{L}^*$  is a property of the pattern and independent of  $\mathcal{L}$  for large times,  $\Delta \propto \mathcal{P}^{1/2}$  cannot be true. It is well possible that the  $\mathcal{P}^{1/2}$ -scaling that we observed in SDC only holds for intermediate time scales when the particle transition between rolls is still the main source of diffusion enhancements, but breaks down for long times and gets replaced by  $\Delta \propto \mathcal{P}$  if the spatiotemporal chaos of rolls is the dominating mechanism. To get a clear result on whether the effective diffusivities converge for long times, the simulation time at low  $\varepsilon$  needs to be increased by at least two orders of magnitude.

Besides two-particle dispersion, we looked at the acceleration statistics of single particles in Section 4.5, and found systematic asymmetries between energy losses and gains that can be considered an indicator for an irreversible dynamics of the flow. Unlike in free turbulence, the scale on which significant acceleration can take place is in our system limited by the size of a convection roll. But while the asymmetry between acceleration and deceleration does not extend to time scales of significant changes within the pattern, the local defect dynamics lead to a quick gain in energy for short times, which is lost only after several vortex turnovers.

## Outlook

Even though we extended the aspect ratio of the Bénard systems even beyond the regime where experimental observations of Spiral Defect Chaos have been reported, we still did not use the parallel implementation to its full capability. At low vertical resolutions, aspect ratios of  $\Gamma = 200$  are possible within the given memory limitations. The computation time for simulating several horizontal thermal diffusion times will be enormous, but the results may provide clues regarding the question whether Spiral Defect Chaos is a stable state for large systems, and where its onset lies.

## 5.2. Transport Properties of Spiral Defect Chaos

Investigation of the pair dispersion should be extended to longer simulation times, to answer the question whether the effective diffusivity is independent of the Péclet number for small  $\varepsilon$ , or depends on the particle diffusivity even when defects are present in a system. Differentiating between the diffusion enhancement of straight convection rolls and particle transport by mean flows and defect dynamics will only be possible by extending the simulations to longer times and lower particle diffusivities. Insights into the long-range transport of particles in the large aspect ratio systems might also be won by engineering a 2D model that captures the hopping of diffusing particles between convection rolls without specifying the detailed dynamics of the rolls themselves, eliminating the smallest time scales and thus allowing for larger total simulation times.

For a detailed investigation of the  $t^3$  scaling that we observed in the initial regime of pair dispersion, a high-resolution simulation of the local flow structure within one convection roll can point to the relevant mechanisms. It will be especially instructive to see whether this scaling region extends even further towards low particle diffusivities, or even reaches  $\mathcal{D} = 0$ . Understanding dispersion in vortices of a given fixed length scale leads the way to understanding transport in vortices at many different length scales, which is turbulence.

To answer open questions regarding particle transport in convection, many additional effects can be introduced for the particles that move through the system. By giving them mass or a density that deviates from that of the fluid, their transport will be significantly altered. While our model can describe diffusion of a molecular dye in the fluid, transport of large proteins, or even small animals, in a thermally driven flow will introduce new effects that were not part of our studies. One special case along these lines would be a coupling from the particle density back to the thermal or viscous properties of the fluid.



# A. Appendix

Discretizing the equations for the temporal evolution is a tedious task, the results of which can be found in this appendix. Appendix A.1 contains the evolution equations for Rayleigh-Bénard convection, as found in Zudrop[32]. The penalization scheme introduced in Section 3.1.4 will not be covered by this appendix, but can be found in [32]. A list of the simulation parameters for the simulation results that we discuss is presented in Appendix A.2. Appendix A.3 discusses an error in the simulation scheme.

## A.1. Discrete Equations for the Boussinesq Problem

To arrive at a scheme for calculating the coefficients in the spectral representation of the velocity and temperature fields, we strictly follow the notation of Zudrop[32]. The Boussinesq equations (3.28) can be written in the form

$$\partial_t T = \Delta T - \Delta_{xy} f - (\vec{u} \cdot \nabla) T, \quad (\text{A.1a})$$

$$\frac{1}{Pr} \Delta \Delta_{xy} \partial_t f = \Delta^2 \Delta_{xy} f - Ra \Delta_{xy} T - \frac{1}{Pr} \delta (\vec{u} \cdot \nabla \vec{u}), \quad (\text{A.1b})$$

$$\frac{1}{Pr} \Delta_{xy} \partial_t g = \Delta \Delta_{xy} g - \frac{1}{Pr} \epsilon (\vec{u} \cdot \nabla \vec{u}), \quad (\text{A.1c})$$

$$\frac{1}{Pr} \partial_t F = \partial_z^2 F - \frac{1}{Pr} \partial_z \langle u_x u_z \rangle_{xy}, \quad (\text{A.1d})$$

$$\frac{1}{Pr} \partial_t G = \partial_z^2 G - \frac{1}{Pr} \partial_z \langle u_y u_z \rangle_{xy}. \quad (\text{A.1e})$$

When we order the degrees of freedom for the simulation as a *Solution Vector*  $V$ , we can collect the pre-factors of the time derivatives into a linear *Time Stepping Operator*  $B$  and the terms directly proportional to the degrees of freedom into a *Linear Operator*  $L$ . The other terms will then be represented by the *Nonlinear Operator*  $N(V)$ , which is in fact quadratic (or bilinear if written as  $N(V, V)$ ). The equation system then has the simple form

$$B \partial_t V = LV + N(V). \quad (\text{A.2})$$

We will first give representations for the operators  $B$ ,  $L$  and  $N$ , and then combine them into a time stepping scheme that leads from the system state at one time step,  $V_i$ , to the next ( $V_{i+1}$ ). In this section, we follow the convention that modes in the horizontal  $x$ -direction are indexed by the letter  $k$ , modes in the horizontal  $y$ -direction are indexed by  $l$ , and modes in the vertical  $z$ -direction are indexed by  $m$  (and  $m'$  and  $m''$ ) in the ranges

$$k \in [k_{\min}; k_{\max}] \quad \text{with} \quad k_{\max,\min} = \pm \frac{N_x - 1}{2}, \quad (\text{A.3a})$$

$$l \in [l_{\min}; l_{\max}] \quad \text{with} \quad l_{\max,\min} = \pm \frac{N_y - 1}{2}, \quad (\text{A.3b})$$

$$m \in [1; N_z]. \quad (\text{A.3c})$$

## A. Appendix

The solution vector  $V \in \mathbb{R}^{(3N_x N_y + 2) \cdot N_z}$  can be constructed from the different horizontal modes and the mean flow:

$$V = \begin{pmatrix} V_{(k_{\min}, l_{\min})} \\ \vdots \\ V_{k,l} \\ \vdots \\ V_{(k_{\max}, l_{\max})} \\ V_F \\ V_G \end{pmatrix} \quad (\text{A.4})$$

With the vertical modes for temperature and velocity in the solution vector  $V_{k,l} \in \mathbb{R}^{3N_z}$ , and the horizontal mean flow vectors  $V_F, V_G \in \mathbb{R}^{N_z}$  for the mean flow in the directions  $x$  and  $y$ :

$$V_{k,l} = \begin{pmatrix} \hat{T}_{k,l,1} \\ \vdots \\ \hat{T}_{k,l,N_z} \\ \hat{f}_{k,l,1} \\ \vdots \\ \hat{f}_{k,l,N_z} \\ \hat{g}_{k,l,1} \\ \vdots \\ \hat{g}_{k,l,N_z} \end{pmatrix} \quad V_F = \begin{pmatrix} \hat{F}_1 \\ \vdots \\ \hat{F}_{N_z} \end{pmatrix} \quad V_G = \begin{pmatrix} \hat{G}_1 \\ \vdots \\ \hat{G}_{N_z} \end{pmatrix} \quad (\text{A.5})$$

### Time Derivative

Creating the weighted Galerkin average by integrating the left hand side  $B\partial_t V$  of (A.1) over their respective domains yields the following terms:

For the poloidal component of the velocity field,  $f$ :

$$\int_{\Omega} \left( \frac{1}{P_r} \Delta \Delta_{xy} \partial_t f(\vec{x}, t) \right) \overline{E_k(x) E_l(y) C_m(z)} \, d\vec{x} = \frac{4\pi^2(k^2 + l^2)}{P_r L^2} \left( \frac{4\pi^2(k^2 + l^2)}{L^2} \partial_t \hat{f}_{k,l,m} - \sum_{m'} \langle C''_{m'}, C_m \rangle_z \partial_t \hat{f}_{k,l,m'} \right) \quad (\text{A.6a})$$

For the toroidal component of the velocity field,  $g$ :

$$\int_{\Omega} \left( \frac{1}{P_r} \Delta_{xy} \partial_t g(\vec{x}, t) \right) \overline{E_k(x) E_l(y) S_m(z)} \, d\vec{x} = -\frac{2\pi^2(k^2 + l^2)}{P_r L^2} \partial_t \hat{g}_{k,l,m} \quad (\text{A.6b})$$

For the mean flows  $F$  and  $G$ :

$$\int_{\Omega_z} \left( \frac{1}{P_r} \partial_t F(z, t) \right) \overline{S_m(z)} \, dz = \frac{1}{2P_r} \partial_t \hat{F}_m \quad (\text{A.6c})$$

$$\int_{\Omega_z} \left( \frac{1}{P_r} \partial_t G(z, t) \right) \overline{S_m(z)} \, dz = \frac{1}{2P_r} \partial_t \hat{G}_m \quad (\text{A.6d})$$

For the temperature field  $T$ :

$$\int_{\Omega} (\partial_t T(\vec{x}, t)) \overline{E_k(x) E_l(y) S_m(z)} \, d\vec{x} = \frac{1}{2} \partial_t \hat{T}_{k,l,m} \quad (\text{A.6e})$$

This defines the operator  $B$ , which is block diagonal for each  $k_x, k_y$ -mode and has two entries for the mean flow matrices  $B^F$  and  $B^G$ :

$$B = \begin{pmatrix} B_{k_{\min}, l_{\min}} & 0 & 0 & \dots & 0 \\ 0 & \ddots & 0 & \dots & 0 \\ 0 & 0 & B_{kl} & & 0 \\ \vdots & \vdots & & \ddots & \\ 0 & 0 & 0 & B^F & 0 \\ 0 & 0 & 0 & 0 & B^G \end{pmatrix} \quad (\text{A.7})$$

Each block is again diagonal, except for  $f$ , where the vertical modes couple.  $B_{kl}$  has the form

$$B_{kl} = \begin{pmatrix} B_{kl}^T & 0 & 0 \\ 0 & B_{kl}^f & 0 \\ 0 & 0 & B_{kl}^g \end{pmatrix}. \quad (\text{A.8})$$

The individual sub-matrices of the operator  $B$  are then defined as:

$$(B_{kl}^T)_{mm'} := \frac{1}{2} \delta_{m,m'} \quad (\text{A.9a})$$

$$(B_{kl}^f)_{mm'} := \left[ \frac{4\pi^2(k^2+l^2)}{PrL^2} \left( \frac{4\pi^2(k^2+l^2)}{L^2} \cdot \delta_{m,m'} - \langle C''_{m'}, C_m \rangle_z \right) \right] \quad (\text{A.9b})$$

$$(B_{kl}^g)_{mm'} := - \left[ \frac{2\pi^2(k^2+l^2)}{PrL^2} \right] \cdot \delta_{m,m'} \quad (\text{A.9c})$$

$$(B^F)_{mm'} := \frac{1}{2Pr} \delta_{m,m'} \quad (\text{A.9d})$$

$$(B^G)_{mm'} := \frac{1}{2Pr} \delta_{m,m'} \quad (\text{A.9e})$$

### Linear term

Analogously, the weighted integrals over the linear terms  $LV$  from the right hand side of (A.1) read:

For the poloidal component of the velocity field,  $f$ :

$$\begin{aligned} \int_{\Omega} (\Delta^2 \Delta_{xy} f(\vec{x}, t) - Ra \Delta_{xy} T(\vec{x}, t)) \overline{E_k(x) E_l(y) C_m(z)} \, d\vec{x} = \\ - \frac{4\pi^2(k^2+l^2)}{L^2} \left[ \left( \frac{16\pi^4(k^2+l^2)^2}{L^4} + \lambda_m^4 \right) \hat{f}_{k,l,m} - \frac{8\pi^2(k^2+l^2)}{L^2} \sum_{m'} \langle C''_{m'}, C_m \rangle_z \hat{f}_{k,l,m'} \right] \\ + Ra \cdot \frac{4\pi^2(k^2+l^2)}{L^2} \sum_{m'} \langle S_{m'}, C_m \rangle_z \hat{T}_{k,l,m'} \quad (\text{A.10a}) \end{aligned}$$

## A. Appendix

For the toroidal component of the velocity field,  $g$ :

$$\int_{\Omega} (\Delta \Delta_{xy} g(\vec{x}, t)) \overline{E_k(x) E_l(y) S_m(z)} d\vec{x} = \frac{4\pi^2(k^2+l^2)}{L^2} \left( \frac{2\pi^2(k^2+l^2)}{L^2} + \frac{m^2\pi^2}{2} \right) \hat{g}_{k,l,m} \quad (\text{A.10b})$$

For the mean flows  $F$  and  $G$ :

$$\int_{\Omega_z} (\partial_z^2 F(z, t)) \overline{S_m(z)} dz = -\frac{m^2\pi^2}{2} \hat{F}_m \quad (\text{A.10c})$$

$$\int_{\Omega_z} (\partial_z^2 G(z, t)) \overline{S_m(z)} dz = -\frac{m^2\pi^2}{2} \hat{G}_m \quad (\text{A.10d})$$

For the temperature field  $T$ :

$$\begin{aligned} \int_{\Omega} (\Delta T(\vec{x}, t) - \Delta_{xy} f(\vec{x}, t)) \overline{E_k(x) E_l(y) S_m(z)} d\vec{x} = \\ - \left( \frac{2\pi^2(k^2+l^2)}{L^2} + \frac{m^2\pi^2}{2} \right) \hat{T}_{k,l,m} + \frac{2\pi^2(k^2+l^2)}{L^2} \sum_{m'} \langle C_{m'}, S_m \rangle_z \hat{f}_{k,l,m'} \end{aligned} \quad (\text{A.10e})$$

This defines the operator  $L$ , which, like  $B$ , is block diagonal for each  $k_x, k_y$ -mode and the mean flow matrices  $L^F$  and  $L^G$ :

$$L = \begin{pmatrix} L_{k_{\min}, l_{\min}} & 0 & 0 & \dots & 0 \\ 0 & \ddots & 0 & \dots & 0 \\ 0 & 0 & L_{kl} & & 0 \\ \vdots & \vdots & & \ddots & \\ & & & & L^F & 0 \\ 0 & 0 & 0 & 0 & 0 & L^G \end{pmatrix} \quad (\text{A.11})$$

Unlike the  $B$  matrix, the linear operator includes a coupling between  $f$  and  $T$ , whereas the term for  $g$  does not couple to them, such that the operator can be written as

$$L_{kl} = \begin{pmatrix} L_{kl}^{TT} & L_{kl}^{Tf} & 0 \\ L_{kl}^{fT} & L_{kl}^{ff} & 0 \\ 0 & 0 & L_{kl}^g \end{pmatrix}, \quad (\text{A.12})$$

where the individual sub-matrices are defined via the relations:

$$(L_{kl}^{TT})_{mm'} := -\frac{1}{2} \left[ \frac{4\pi^2(k^2+l^2)}{L^2} + m^2\pi^2 \right] \cdot \delta_{m,m'} \quad (\text{A.13a})$$

$$(L_{kl}^{Tf})_{mm'} := \frac{4\pi^2(k^2+l^2)}{L^2} \langle C_{m'}, S_m \rangle_z \quad (\text{A.13b})$$

$$(L_{kl}^{fT})_{mm'} := Ra \cdot \frac{4\pi^2(k^2+l^2)}{L^2} \langle S_{m'}, C_m \rangle_z \quad (\text{A.13c})$$

$$(L_{kl}^{ff})_{mm'} := -\frac{4\pi^2(k^2+l^2)}{L^2} \left[ \left( \frac{16\pi^4(k^2+l^2)^2}{L^4} + \lambda_m^4 \right) \delta_{m,m'} - \frac{8\pi^2(k^2+l^2)}{L^2} \langle C''_{m'}, C_m \rangle_z \right] \quad (\text{A.13d})$$

$$(L_{kl}^g)_{mm'} := \left[ \frac{4\pi^2(k^2+l^2)}{L^2} \left( \frac{2\pi^2(k^2+l^2)}{L^2} + \frac{m^2\pi^2}{2} \right) \right] \cdot \delta_{m,m'} \quad (\text{A.13e})$$

$$(L^F)_{mm'} := -\frac{m^2\pi^2}{2} \delta_{m,m'} \quad (\text{A.13f})$$

$$(L^G)_{mm'} := -\frac{m^2\pi^2}{2} \delta_{m,m'} \quad (\text{A.13g})$$

### Nonlinear term

As described in Section 3.1.3, evaluation of the nonlinear term  $N(V)$  of the simulation scheme involves a Fourier transform of the fields  $f$ ,  $g$  and  $T$  into real space. To simplify notation, we define the following quantities (which depend on the  $x$ - and  $y$ -position, the  $z$  mode index  $m$ , and time  $t$ ):

$$v_x := \partial_x \langle f, C_m \rangle_z \quad w_x := \partial_y \langle g, S_m \rangle_z + \langle F, S_m \rangle_z \quad (\text{A.14a})$$

$$v_y := \partial_y \langle f, C_m \rangle_z \quad w_y := -\partial_x \langle g, S_m \rangle_z + \langle G, S_m \rangle_z \quad (\text{A.14b})$$

$$v_z := \Delta_{xy} \langle f, C_m \rangle_z \quad (\text{A.14c})$$

The values for these fields (and their spatial derivatives) at discrete spatial locations will be calculated via a two-dimensional complex-to-real discrete Fourier transform, where we take advantage of the fact that a spatial derivative in real space can be expressed by a multiplication in Fourier space.

The operator  $\vec{u} \cdot \nabla \vec{u}$  (with  $\nabla \cdot \vec{u} = 0$ ) can be written as:

$$\vec{u} \cdot \nabla \vec{u} = \begin{pmatrix} \partial_x(u_x u_x) + \partial_y(u_y u_x) + \partial_z(u_z u_x) \\ \partial_x(u_x u_y) + \partial_y(u_y u_y) + \partial_z(u_z u_y) \\ \partial_x(u_x u_z) + \partial_y(u_y u_z) + \partial_z(u_z u_z) \end{pmatrix} \quad (\text{A.15})$$

The velocity field  $\vec{u}(\vec{x}, t)$  can then be expressed as:

$$\vec{u}(\vec{x}, t) = \begin{pmatrix} \sum_m C'_m(z) \cdot v_x(x, y, m, t) + S_m(z) \cdot w_x(x, y, m, t) \\ \sum_m C'_m(z) \cdot v_y(x, y, m, t) + S_m(z) \cdot w_y(x, y, m, t) \\ \sum_m C_m(z) \cdot v_z(x, y, m, t) \end{pmatrix} \quad (\text{A.16})$$

With this velocity field, the terms  $u_i u_j$  from (A.15) are:

$$\begin{aligned} u_x u_x &= \sum_{m,m'} [C'_m C'_{m'} v_x(m) v_x(m') + 2C'_m S_{m'} v_x(m) w_x(m') + S_m S_{m'} w_x(m) w_x(m')] \\ u_y u_y &= \sum_{m,m'} [C'_m C'_{m'} w_x(m) w_x(m') + 2C'_m S_{m'} v_y(m) w_y(m') + S_m S_{m'} w_y(m) w_y(m')] \\ u_z u_z &= \sum_{m,m'} [C_m C_{m'} v_z(m) v_z(m')] \\ u_x u_y &= \sum_{m,m'} [C'_m C'_{m'} v_y(m) v_x(m') + C'_m S_{m'} (v_y(m) w_x(m') + v_x(m) w_y(m')) + S_m S_{m'} w_y(m) w_x(m')] \\ u_x u_z &= \sum_{m,m'} [C'_m C_{m'} v_x(m) v_z(m') + S_m C_{m'} w_x(m) v_z(m')] \\ u_y u_z &= \sum_{m,m'} [C'_m C_{m'} v_y(m) v_z(m') + S_m C_{m'} w_y(m) v_z(m')] \end{aligned}$$

## A. Appendix

With  $T(m) := \langle T, S_m \rangle_z$ , the parts of  $(\vec{u} \cdot \nabla T) = u_x \partial_x T + u_y \partial_y T + u_z \partial_z T$  have the form:

$$\begin{aligned} u_x \partial_x T &= \sum_{m,m'} [C'_m(z)S_{m'}(z) \cdot v_x(m) + S_m(z)S_{m'}(z) \cdot w_x(m)] \partial_x T(m') \\ u_y \partial_y T &= \sum_{m,m'} [C'_m(z)S_{m'}(z) \cdot v_y(m) + S_m(z)S_{m'}(z) \cdot w_y(m)] \partial_y T(m') \\ u_z \partial_z T &= \sum_{m,m'} [C_m(z)S'_{m'}(z) \cdot v_z(m)] T(m') \end{aligned}$$

These terms can now be used to assemble a discretized formulation for the nonlinear terms of Equations (A.1), again by multiplying with the Galerkin weighting functions and integrating over space. For the poloidal component  $f$  and toroidal  $g$ , integration yields:

$$\begin{aligned} &\int_{\Omega} \left( \frac{1}{Pr} \delta \cdot (\vec{u} \cdot \nabla \vec{u}) \right) \overline{E_k(x) E_l(y) C_m(z)} \, d\vec{x} \\ &= \frac{-4\pi^2 k^2}{PrL^2} \left[ \sum_{m',m''} \begin{array}{l} \langle \partial_z(C'_{m'}C'_{m''}), C_m \rangle_z \mathcal{F}_{xy}(v_x(m') \cdot v_x(m''))(k,l) \\ + 2\langle \partial_z(C'_{m'}S_{m''}), C_m \rangle_z \mathcal{F}_{xy}(v_x(m') \cdot w_x(m''))(k,l) \\ + \langle \partial_z(S_{m'}S_{m''}, C_m) \rangle_z \mathcal{F}_{xy}(w_x(m') \cdot w_x(m''))(k,l) \end{array} \right] \\ &- \frac{4\pi^2 l^2}{PrL^2} \left[ \sum_{m',m''} \begin{array}{l} \langle \partial_z(C'_{m'}C'_{m''}), C_m \rangle_z \mathcal{F}_{xy}(v_y(m') \cdot v_y(m''))(k,l) \\ + 2\langle \partial_z(C'_{m'}S_{m''}), C_m \rangle_z \mathcal{F}_{xy}(v_y(m') \cdot w_y(m''))(k,l) \\ + \langle \partial_z(S_{m'}S_{m''}, C_m) \rangle_z \mathcal{F}_{xy}(w_y(m') \cdot w_y(m''))(k,l) \end{array} \right] \\ &- \frac{8\pi^2 kl}{PrL^2} \left[ \sum_{m',m''} \begin{array}{l} \langle \partial_z(C'_{m'}C'_{m''}), C_m \rangle_z \mathcal{F}_{xy}(v_y(m') \cdot v_x(m''))(k,l) \\ + \langle \partial_z(C'_{m'}S_{m''}), C_m \rangle_z \mathcal{F}_{xy}(v_y(m') \cdot w_x(m''))(k,l) \\ + \langle \partial_z(S_{m'}S_{m''}, C_m) \rangle_z \mathcal{F}_{xy}(w_y(m') \cdot v_x(m''))(k,l) \\ + \langle \partial_z(S_{m'}S_{m''}, C_m) \rangle_z \mathcal{F}_{xy}(w_y(m') \cdot w_x(m''))(k,l) \end{array} \right] \\ &+ \frac{2\pi ik}{PrL} \left[ \sum_{m',m''} \begin{array}{l} \langle \partial_z^2(C_{m'}C'_{m''}), C_m \rangle_z \mathcal{F}_{xy}(v_z(m') \cdot v_x(m''))(k,l) \\ + \langle \partial_z^2(C_{m'}S_{m''}), C_m \rangle_z \mathcal{F}_{xy}(v_z(m') \cdot w_x(m''))(k,l) \end{array} \right] \\ &+ \frac{2\pi il}{PrL} \left[ \sum_{m',m''} \begin{array}{l} \langle \partial_z^2(C_{m'}C'_{m''}), C_m \rangle_z \mathcal{F}_{xy}(v_z(m') \cdot v_y(m''))(k,l) \\ + \langle \partial_z^2(C_{m'}S_{m''}), C_m \rangle_z \mathcal{F}_{xy}(v_z(m') \cdot w_y(m''))(k,l) \end{array} \right] \\ &+ \frac{8\pi^3 ik(k^2 + l^2)}{PrL^3} \left[ \sum_{m',m''} \begin{array}{l} \langle (C'_{m'}C_{m''}), C_m \rangle_z \mathcal{F}_{xy}(v_x(m') \cdot v_z(m''))(k,l) \\ + \langle (S_{m'}C_{m''}), C_m \rangle_z \mathcal{F}_{xy}(w_x(m') \cdot v_z(m''))(k,l) \end{array} \right] \\ &+ \frac{8\pi^3 il(k^2 + l^2)}{PrL^3} \left[ \sum_{m',m''} \begin{array}{l} \langle (C'_{m'}C_{m''}), C_m \rangle_z \mathcal{F}_{xy}(v_y(m') \cdot v_z(m''))(k,l) \\ + \langle (S_{m'}C_{m''}), C_m \rangle_z \mathcal{F}_{xy}(w_y(m') \cdot v_z(m''))(k,l) \end{array} \right] \\ &+ \frac{4\pi^2(k^2 + l^2)}{PrL^2} \left[ \sum_{m',m''} \langle \partial_z(C_{m'}C_{m''}), C_m \rangle_z \mathcal{F}_{xy}(v_z(m') \cdot v_z(m''))(k,l) \right] \quad (\text{A.17a}) \end{aligned}$$

$$\begin{aligned} &\int_{\Omega} \left( \frac{1}{Pr} \epsilon \cdot (\vec{u} \cdot \nabla \vec{u}) \right) \overline{E_k(x) E_l(y) S_m(z)} \, d\vec{x} \\ &= \frac{-4\pi^2 kl}{PrL^2} \left[ \sum_{m',m''} \begin{array}{l} \langle (C'_{m'}C'_{m''}), S_m \rangle_z \mathcal{F}_{xy}(v_x(m') \cdot v_x(m''))(k,l) \\ + 2\langle (C'_{m'}S_{m''}), S_m \rangle_z \mathcal{F}_{xy}(v_x(m') \cdot w_x(m''))(k,l) \\ + \langle (S_{m'}S_{m''}), S_m \rangle_z \mathcal{F}_{xy}(w_x(m') \cdot w_x(m''))(k,l) \end{array} \right] \end{aligned}$$

$$\begin{aligned}
& + \frac{4\pi^2 kl}{PrL^2} \left[ \sum_{m',m''} \begin{array}{l} \langle (C'_{m'} C'_{m''}), S_m \rangle_z \mathcal{F}_{xy}(v_y(m') \cdot v_y(m''))(k,l) \\ + 2 \langle (C'_{m'} S_{m''}), S_m \rangle_z \mathcal{F}_{xy}(v_y(m') \cdot w_y(m''))(k,l) \\ + \langle (S_{m'} S_{m''}), S_m \rangle_z \mathcal{F}_{xy}(w_y(m') \cdot w_y(m''))(k,l) \end{array} \right] \\
& + \frac{4\pi^2(k^2 - l^2)}{PrL^2} \left[ \sum_{m',m''} \begin{array}{l} \langle (C'_{m'} C'_{m''}), S_m \rangle_z \mathcal{F}_{xy}(v_x(m') \cdot v_y(m''))(k,l) \\ + \langle (S_{m'} C'_{m''}), S_m \rangle_z \mathcal{F}_{xy}(w_x(m') \cdot v_y(m''))(k,l) \\ + \langle (C'_{m'} S_{m''}), S_m \rangle_z \mathcal{F}_{xy}(w_y(m') \cdot v_x(m''))(k,l) \\ + \langle (S_{m'} S_{m''}), S_m \rangle_z \mathcal{F}_{xy}(w_x(m') \cdot w_y(m''))(k,l) \end{array} \right] \\
& + \frac{2\pi il}{PrL} \left[ \sum_{m',m''} \begin{array}{l} \langle \partial_z(C_{m'} C'_{m''}), S_m \rangle_z \mathcal{F}_{xy}(v_z(m') \cdot v_x(m''))(k,l) \\ + \langle \partial_z(C_{m'} S_{m''}), S_m \rangle_z \mathcal{F}_{xy}(v_z(m') \cdot w_x(m''))(k,l) \end{array} \right] \\
& - \frac{2\pi ik}{PrL} \left[ \sum_{m',m''} \begin{array}{l} \langle \partial_z(C_{m'} C'_{m''}), S_m \rangle_z \mathcal{F}_{xy}(v_z(m') \cdot v_y(m''))(k,l) \\ + \langle \partial_z(C_{m'} S_{m''}), S_m \rangle_z \mathcal{F}_{xy}(v_z(m') \cdot w_y(m''))(k,l) \end{array} \right] \quad (\text{A.17b})
\end{aligned}$$

For the nonlinearity in the evolution of  $F$  and  $G$ , the mean flow is defined by the  $(k, l) = (0, 0)$ -mode in Fourier space, such that the equations read:

$$\begin{aligned}
& \int_{\Omega_z} \left( \frac{1}{Pr} \partial_z \langle u_x u_z \rangle_{xy} \right) \overline{S_m(z)} \, dz \\
&= \frac{1}{Pr} \left[ \sum_{m',m''} \begin{array}{l} \langle \partial_z(C'_{m'} C'_{m''}), S_m \rangle_z \mathcal{F}_{xy}(v_x(m') \cdot v_z(m''))(0,0) \\ + \langle \partial_z(S_{m'} C'_{m''}), S_m \rangle_z \mathcal{F}_{xy}(w_x(m') \cdot v_z(m''))(0,0) \end{array} \right] \quad (\text{A.17c})
\end{aligned}$$

$$\begin{aligned}
& \int_{\Omega_z} \left( \frac{1}{Pr} \partial_z \langle u_y u_z \rangle_{xy} \right) \overline{S_m(z)} \, dz \\
&= \frac{1}{Pr} \left[ \sum_{m',m''} \begin{array}{l} \langle \partial_z(C'_{m'} C'_{m''}), S_m \rangle_z \mathcal{F}_{xy}(v_y(m') \cdot v_z(m''))(0,0) \\ + \langle \partial_z(S_{m'} C'_{m''}), S_m \rangle_z \mathcal{F}_{xy}(w_y(m') \cdot v_z(m''))(0,0) \end{array} \right] \quad (\text{A.17d})
\end{aligned}$$

Finally, the nonlinear term for the temperature field  $T$  is:

$$\begin{aligned}
& \int_{\Omega} (\vec{u} \cdot \nabla T) \overline{E_k(x) E_l(y) S_m(z)} \, d\vec{x} \\
&= \sum_{m',m''} \left[ \begin{array}{l} \langle (C'_{m'} S_{m''}), S_m \rangle_z \mathcal{F}_{xy}(v_x(m') \cdot \partial_x T(m''))(k,l) \\ + \langle (S_{m'} S_{m''}), S_m \rangle_z \mathcal{F}_{xy}(w_x(m') \cdot \partial_x T(m''))(k,l) \end{array} \right] \\
&+ \sum_{m',m''} \left[ \begin{array}{l} \langle (C'_{m'} S_{m''}), S_m \rangle_z \mathcal{F}_{xy}(v_y(m') \cdot \partial_y T(m''))(k,l) \\ + \langle (S_{m'} S_{m''}), S_m \rangle_z \mathcal{F}_{xy}(w_y(m') \cdot \partial_y T(m''))(k,l) \end{array} \right] \\
&+ \sum_{m',m''} \left[ \begin{array}{l} \langle (C'_{m'} S'_{m''}), S_m \rangle_z \mathcal{F}_{xy}(v_z(m') \cdot T(m''))(k,l) \end{array} \right] \quad (\text{A.17e})
\end{aligned}$$

## A. Appendix

### A.2. Table of Simulation Parameters

This section lists simulation parameters that were used to create the data. For the cylindrical geometry, the penalization scheme was used with different  $\eta$ , generally  $\eta = 0.02$ . The number of modes are presented in real space, due to the real-to-complex FFT, the simulation used  $N_x/2 + 1$   $x$ -modes with complex coefficients. All lengths are in  $d$ , all times in  $\tau_v = d^2/\kappa$ . The initialization time before introduction of tracer particles is called  $t_{\text{init}}$ , initialization generally ends at  $t_0 = 0$ . Counted from that point,  $t_{\text{max}}$  denotes the maximum simulation time.

Simulation	Section	$Ra$	$L_x \times L_y$	Geometry	$N_x \times N_y \times N_z$	$dt$	$t_{\text{init}}$	$t_{\text{max}}$
Onset Periodic <sup>a</sup>	4.1	$\leq 2732$	$200 \times 200$	periodic	$1024 \times 1024 \times 2$	0.01	60000	-
ISR	4.2.1	2647	$100 \times 100$	periodic	$1024 \times 1024 \times 2$	0.01	5	1000
ISR with Mean Flow	4.2.2	2647	$100 \times 100$	periodic	$1024 \times 1024 \times 2$	0.01	5	1000
Giant Spiral	4.2.3	2732	$70 \times 70$	cylinder	$512 \times 512 \times 2$	0.01	50	500
Dislocation	4.2.4	2647	$140 \times 140$	periodic	$1024 \times 1024 \times 2$	0.01	5	1000
Dislocation Line <sup>b</sup>	4.2.5	2135	$200 \times 200$	periodic	$1024 \times 1024 \times 2$	0.01	40000	1000
Diff. of Pass. Scalar	4.3	$\leq 4270$	$60 \times 60$	cylinder	$256 \times 256 \times 5$	0.005	100	100
Diff. of Pass. Scalar <sup>b</sup>	4.3	$\leq 2732$	$200 \times 200$	periodic	$1024 \times 1024 \times 2$	0.01	40000	1000
Dispersion <sup>c</sup>	4.4	$\leq 2732$	$200 \times 200$	periodic	$1024 \times 1024 \times 2$	0.01	40000	1000
Dislocation Effects	4.4.5	3500	$100 \times 100$	periodic	$512 \times 512 \times 4$	0.005	100	100
Irreversibility <sup>b</sup>	4.5	$\leq 3500$	$100 \times 100$	periodic	$512 \times 512 \times 4$	0.01	10000	10000

<sup>a</sup> In the initialization of the large aspect ratio system, an initialization time of 50000  $\tau_v$  was simulated with the error discussed in Appendix A.3 before the correct code was used.

<sup>b</sup> These simulations were performed with the error discussed in Appendix A.3.

<sup>c</sup> The data shown for  $t > 5 \tau_v$  is from simulations with the error discussed in Appendix A.3.

### A.3. Error in the Simulation Code

After a significant portion of the simulations for this thesis had been performed, we discovered that the nonlinear operator of the simulation code was using the overlap integral  $\langle \partial_z^2(C_{m''}C'_{m'}), C_m \rangle$  instead of the correct integral  $\langle \partial_z^2(C_{m'}C'_{m''}), C_m \rangle$  of Equation (A.17a) in Appendix A.1. This subtle difference in the indexing ( $m'$  and  $m''$  are swapped) had no noticeable effect on the convection pattern, but was discovered in a validation step when the simulation results were compared to a different implementation of the same simulation scheme for a rotating convection system. In the equilibrated system, the error was smaller than the total nonlinear operator by a factor of  $10^4$ . The error, which in this thesis only affected simulations with  $N_z = 2$ , influences the nonlinear coupling between the first and second vertical mode for high horizontal wave numbers, in the interaction of the horizontal and vertical flow field.

We repeated some of the simulations with the correct simulation code, and found the transport properties of the pattern to be unchanged. Due to time constraints, we could not repeat simulations for large aspect ratios; but since we found the local properties to be the same and had not been able to distinguish the large scale pattern from Spiral Defect Chaos in the first place, we believe that the error does not affect the results. This is especially true for the investigation of irreversibility, where we consider flow properties of chaotic systems without the explicit goal of describing Rayleigh-Bénard convection. The most critical impact of the error is in Section 4.1, where we investigate the onset of Spiral Defect Chaos that is likely sensitive to the slightest variations in the simulation. Here we recommend repeating the simulations with the correct code, for a longer initialization time, and for a larger vertical resolution to find the Rayleigh number at which Spiral Defect Chaos sets in.



# Bibliography

- [1] P. Angot, C. H. Bruneau, and P. Fabrie. A penalization method to take into account obstacles in incompressible viscous flows. *Numerische Mathematik*, 81(4):497–520, 1999. doi: 10.1007/s002110050401.
- [2] H. Aref. Stochastic particle motion in laminar flows. *Phys. Fluids A*, 3:1009, 1991. doi: 10.1063/1.858080.
- [3] H. Bénard. Les tourbillons cellulaires dans une nappe liquide. *Revue generale des Sciences*, XII:1261–1309, 1900.
- [4] P. Bergé and M. Dubois. Rayleigh-Bénard convection. *Contemp. Phys.*, 25(6):535–582, 1984.
- [5] E. Bodenschatz, W. Pesch, and G. Ahlers. Recent developments in Rayleigh-Benard convection. *Ann. Rev. Fluid Mech.*, 32:709–778, 2000. doi: 10.1146/annurev.fluid.32.1.709.
- [6] G. Boffetta, A. Mazzino, and A. Vulpiani. Transport of inert and reactive particles: Lagrangian statistics in turbulent flow. *Lect. Notes Phys.*, 744:37–70, 2008. doi: 10.1007/978-3-540-75215-8.
- [7] J. Boussinesq. *Théorie de l’écoulement tourbillonnant et tumultueux des liquides dans les lits rectilignes à grande section*. Paris, Gauthier-Villars et fils, 1897.
- [8] J. P. Boyd. *Chebyshev and Fourier Spectral Methods*. Courier Dover Publications, 2001.
- [9] R. E. Britter. Atmospheric dispersion of dense gases. *Annu. Rev. Fluid Mech.*, 21:317–344, 1989. doi: 10.1146/annurev.fluid.21.1.317.
- [10] H. Bruus. *Theoretical Microfluidics*. Oxford University Press, 2008.
- [11] K.-H. Chiam, M. C. Cross, H. S. Greenside, and P. F. Fischer. Enhanced tracer transport by the spiral defect chaos state of a convecting fluid. *Phys. Rev. E*, 71:036205, 2005. doi: 10.1103/PhysRevE.71.036205.
- [12] Nvidia Corporation. *CUDA Toolkit 4.2 CUFFT Library Programming Guide*. Version 1, 2012.
- [13] Nvidia Corporation. *CUDA Toolkit 5.0 CURAND Guide*. Version 2, 2012.
- [14] Nvidia Corporation. *CUDA C Programming Guide*. Version 4.2, 2012.
- [15] V. Croquette and H. Williams. Nonlinear waves of the oscillatory instability on finite convective rolls. *Physica D: Nonlinear Phenomena*, 37(1–3):300 – 314, 1989. doi: 10.1016/0167-2789(89)90138-3.

## Bibliography

- [16] M. Cross and H. Greenside. *Pattern Formation and Dynamics in Nonequilibrium Systems*. Cambridge University Press, 2009.
- [17] M. M. Fyrillas and K. K. Nomura. Diffusion and Brownian motion in Lagrangian coordinates. *J. Chem. Phys.*, 126(164510), 2007. doi: 10.1063/1.2717185.
- [18] M. Marder. *Condensed Matter Physics*. Wiley, 2010.
- [19] I. V. Melnikov, D. A. Egolf, S. Jeanjean, B. Plapp, and E. Bodenschatz. Invasion of Spiral Defect Chaos into Straight Rolls in Rayleigh-Bénard convection. *AIP Conf. Proc.*, 501:36, 2000. doi: 10.1063/1.59948.
- [20] S. W. Morris, E. Bodenschatz, D. S. Cannell, and G. Ahlers. Spiral defect chaos in large aspect ratio Rayleigh-Bénard convection. *Phys. Rev. Lett.*, 71:2026–2029, Sep 1993. doi: 10.1103/PhysRevLett.71.2026.
- [21] B. Plapp. *Spiral-pattern formation in Rayleigh-Bénard convection*. PhD thesis, Cornell Univ., Ithaca, New York, 1997.
- [22] B. Plapp, D. Egolf, E. Bodenschatz, and W. Pesch. Dynamics and selection of giant spirals in Rayleigh-Bénard convection. *Phys. Rev. Lett.*, 81:5334–5337, 1998. doi: 10.1103/PhysRevLett.81.5334.
- [23] Lord Rayleigh. On convection currents in a horizontal layer of fluid, when the higher temperature is on the under side. *Philosophical Magazine*, 32(187-92):529–546, Jul-Dec 1916. ISSN 1478-6435.
- [24] O. Reynolds, A. W. Brightmore, and W. H. Moorby. *Papers on mechanical and physical subjects*, volume 3. Cambridge University Press, 1903.
- [25] J. Salazar and L. Collins. Two-particle dispersion in isotropic turbulent flows. *Annu. Rev. Fluid Mech.*, 41:405–432, 2009. doi: 10.1146/annurev.fluid.40.111406.102224.
- [26] A. Schlüter, D. Lortz, and F. Busse. On the stability of steady finite amplitude convection. *J. Fluid Mech.*, 23:129–144, 1965. doi: 10.1017/S0022112065001271.
- [27] B. Schmitt and W. von Wahl. Decomposition of Solenoidal Fields into Poloidal Fields, Toroidal Fields and the Mean Flow. Applications to the Boussinesq-Equations. In *The Navier-Stokes Equations II — Theory and Numerical Methods*, pages 291–305. Springer Berlin Heidelberg, 1992.
- [28] T. H. Solomon and J. P. Gollub. Passive transport in steady Rayleigh-Bénard convection. *Phys. Fluids*, 31:1372, 1988. doi: 10.1063/1.866729.
- [29] P. Sundararajan and A. D. Stroock. Transport phenomena in chaotic laminar flows. *Annu. Rev. Chem. Biomol. Eng.*, 3:473–96, 2012. doi: 10.1146/annurev-chembioeng-062011-081000.
- [30] F. Toschi and E. Bodenschatz. Lagrangian properties of particles in turbulence. *Annu. Rev. Fluid Mech.*, 41:375–404, 2009. doi: 10.1146/annurev.fluid.010908.165210.

## *Bibliography*

- [31] H. Xu, A. Pumir, and E. Bodenschatz. Private communication.
- [32] J. Zudrop. Simulation of weak turbulent Rayleigh-Bénard convection on a GPU. Master's thesis, Georg-August-Universität Göttingen, 2011.



**Erklärung** nach §18(8) der Prüfungsordnung für den Bachelor-Studiengang Physik und den Master-Studiengang Physik an der Universität Göttingen:

Hiermit erkläre ich, dass ich diese Abschlussarbeit selbstständig verfasst habe, keine anderen als die angegebenen Quellen und Hilfsmittel benutzt habe und alle Stellen, die wörtlich oder sinngemäß aus veröffentlichten Schriften entnommen wurden, als solche kenntlich gemacht habe.

Darüberhinaus erkläre ich, dass diese Abschlussarbeit nicht, auch nicht auszugsweise, im Rahmen einer nichtbestandenen Prüfung an dieser oder einer anderen Hochschule eingereicht wurde.

Göttingen, den 29. August 2013

(Simon Schütz)